

Establishment and Characterisation of a Clinically Relevant Metaphyseal Fracture Model in the Distal Femur of Skeletally Matured Sheep

Inaugural Dissertation
submitted to the
Faculty of Medicine
in partial fulfilment of the requirements
for the PhD-Degree
of the Faculties of Veterinary Medicine and Medicine
of the Justus Liebig University Giessen

by
Alagboso, Francisca Ijeoma
of
Akokwa

Giessen, 2019

From the Experimental Trauma Surgery, Faculty of Medicine

Director: Univ. Prof. Dr. med. Dr. h.c. Christian Hei

Of the Faculty of Medicine of the Justus-Liebig-University Giessen

Supervisor

Prof. Dr. med. Dr. biol. hom Volker Alt

Committee Members

External Examiner: Prof. Dr. Michael Amling

Committee Chair: Prof. Dr. Klaus-Dieter Schlter

Committee Member: Prof. Dr. med. vet. Sabine Wenisch

Date of PhD Disputation

4th October 2019

Dedicated to my parents

ABSTRACT

Despite the high incidence of metaphyseal bone fractures in patients, the cellular and molecular mechanisms underlying the healing process of metaphyseal fractures are still poorly understood due to the unavailability of suitable experimental animal models. The intention of the current work was to establish a novel clinically relevant large animal model for metaphyseal bone healing in the distal femur of skeletally matured sheep. In contrast to commonly used partial osteotomy models, this model employed a complete wedge-shaped osteotomy at the metaphysis. The osteotomy was stabilised internally with a customised anatomical locking titanium plate that allowed immediate postoperative full weight bearing. Bone healing was evaluated at 12 weeks post-fracture relative to the unoperated contralateral femur. No plate breakage or secondary fracture was recorded in the animals. Histological and micro-computed tomography results revealed an increased amount of mineralised and dense trabeculae with rich bone marrow. The new trabeculae healed via direct intramembranous ossification without visible callus and cartilaginous tissue formation. Functional morphological analysis of the osteocyte-lacuna revealed regularly arranged spherically shaped osteocytes-lacunae along with the canaliculi system. The biomechanical test revealed a comparable stiffness in both operated and unoperated femurs. However, the stiffness at their cortical regions was two-fold more than in their trabecular regions. Histomorphometric assessment of two major bone matrix enzymes: ALP (osteoblast marker) and TRAP (osteoclast marker) revealed a significantly higher ALP activity in the operated femur. Bone remodelling was evident by the expressed bone formation markers (COL1A1, ALP, BGLAP, BMP2, ASMA, OPG) and bone resorption markers (RANKL, CTSK) as revealed by quantitative PCR and immunohistochemistry. Bone surface biochemical analysis using time-of-flight secondary ion mass spectrometry showed high, and a homogeneously distributed calcium and collagenous components. Ultrastructural imaging of the new trabeculae revealed a characteristic parallel arrangement of the collagen fibrils uniformly mineralised by the dense mineral substance. Active osteoblasts were characterised by their plump cuboidal-shape, abundant rough endoplasmic reticulum, and a distinct Golgi apparatus whereas active osteoclasts were characterised by their large size, multiple nuclei and a ruffled border. The ultrastructure of the osteocytes varied according to the mineralisation level. The matured star-shaped osteocytes embedded inside the fully mineralised bone whereas young osteocytes embedded within the osteoid or partially mineralised bone areas. In conclusion, this newly established metaphyseal fracture model is of interest to study bone healing and treatment options for the enhancement of metaphyseal fractures.

ZUSAMMENFASSUNG

Ungeachtet einer hohen Inzidenz für metaphysäre Frakturen beim Menschen sind die dem Heilungsprozess unterliegenden zellulären und molekularen Mechanismen immer noch unzureichend bekannt, was in erster Linie durch das Fehlen klinisch relevanter Tiermodelle zu begründen ist. In der vorliegenden Studie wurde ein neuartiges, klinisch relevantes Großtier-Modell für die metaphysäre Knochenheilung im distalen Femur ausgewachsener Schafe etabliert. Im Gegensatz zu normalerweise genutzten partiellen Osteotomien realisierte dieses Modell eine durchgehende keilförmige Osteotomie im Bereich der Metaphyse. Die Osteotomie wurde durch eine anatomische winkelstabile Platte stabilisiert, welche postoperativ sofort eine Vollbelastung erlaubte. 12 Wochen nach der Operation wurde die Knochenheilung in Relation zur gesunden kontralateralen Seite evaluiert. Bei den Tieren traten weder Plattenbrüche noch Sekundärfrakturen auf. Histologische und μ -computertomografische Ergebnisse zeigten eine große Menge mineralisierten Knochens sowie verdichtete Knochen trabekel und reichlich Knochenmark. Neue Knochen trabekel entstanden durch desmale Ossifikation ohne sichtbare Knorpel- oder Kallusbildung. Eine spezifische morphologische Analyse der Osteozytenlakunen veranschaulichte regelmäßig angeordnete sphärische Lakunen zusammen mit den zugehörigen Knochenkanälchen. Biomechanische Tests demonstrierten eine vergleichbare Steifigkeit in den operierten und nicht operierten Femora. Dabei war die Steifigkeit in den kortikalen doppelt so hoch wie in den trabekulären Regionen. Histomorphometrische Analysen zweier wichtiger Knochenmatrix-Enzyme, der ALP (als Osteoblasten-Marker) und der TRAP (als Osteoklasten-Marker), ergaben eine signifikant erhöhte ALP-Aktivität im operierten Femur. Sowohl durch immunhistochemische Färbungen als auch mithilfe der quantitativen PCR konnten aktive Knochenumbau-Prozesse durch die Expression der knochen aufbauenden Marker Col1A1, ALP, BGLAP, BMP2, ASMA, OPG sowie der knochen abbauenden Marker TRAP und CTSK nachgewiesen werden. Die biochemische Analyse der Knochenoberfläche durch die time-of-flight secondary ion mass spectrometry (ToF-SIMS) ergab eine große Menge gleichmäßig verteilten Kalziums wie auch kollagener Komponenten. Die ultrastrukturelle Untersuchung der neu gebildeten Trabekel zeigte charakteristisch parallel angeordnete und gleichmäßig dicht mineralisierte Kollagen-Fibrillen. Aktive Osteoblasten konnten anhand ihrer würfelförmigen Gestalt, des zahlreich vorkommenden rauen endoplasmatischen Retikulums sowie eines auffälligen Golgi-Apparates identifiziert werden, während die aktiven Osteoklasten durch ihre Größe, die Mehrkernigkeit und ein *ruffled border* geprägt waren. Die Ultrastruktur der Osteozyten variierte dem Mineralisierungslevel entsprechend. Reife sternförmige Osteozyten lagen eingeschlossen in vollständig mineralisierter Knochenmatrix, während sich junge Osteozyten im Bereich des Osteoids, bzw. teilweise in mineralisierte Matrix eingebettet fanden. Zusammenfassend ist zu sagen, dass dieses neu etablierte metaphysäre Fraktur-Modell im Schaf zukünftig für die Untersuchung der Knochenheilung und für neue Therapien zur Stimulation zur Heilung bei metaphysären Frakturen genutzt werden kann.

TABLE OF CONTENTS

ABSTRACT	iv
ZUSAMMENFASSUNG	v
TABLE OF CONTENTS	vi
LIST OF FIGURES	ix
LIST OF TABLES	x
LIST OF ABBREVIATIONS	xi
1. INTRODUCTION	1
1.1 Bone structure, composition and function	1
1.2 Healing process of diaphyseal and metaphyseal fractures	2
1.3 Large animal models for fracture healing study	3
1.4 Aim and objectives of the study	8
2. MATERIALS AND METHODS	9
2.1 Ethics statement	9
2.2 Experimental design	9
2.3 Bone mineral density (BMD) measurement using DEXA	10
2.4 Surgical procedure of the femur osteotomy	11
2.5 Post-operative follow-up	12
2.6 Euthanasia and Sample harvesting	13
2.7 Embedding of bone slices in Technovit 9100	13
2.7.1 Preparation of reagents	15
2.8 Micro-computed tomography (micro-CT) analysis	15
2.8.1 Scanning procedure	15
2.8.2 Micro-CT image post-processing and data acquisition	16
2.9 Biomechanical analysis	17
2.10 Bone sample grinding and sectioning	19
2.11 Histological staining	20
2.11.1 Trichrome Masson-Goldner stain	20
2.11.1.1 Preparation of reagents	20
2.11.2 Von-Kossa van-Gieson stain	21
2.11.2.1 Preparation of reagents	21
2.11.3 Silver nitrate stain	22
2.11.3.1 Preparation of reagents	22
2.12 Enzyme histochemical staining	22
2.12.1 Alkaline phosphatase (ALP) stain	22

2.12.1.1 Preparation of reagents.....	23
2.12.2 Tartrate-resistant acid phosphatase (TRAP) stain	23
2.12.2.1 Preparation of reagents.....	23
2.13 Immunohistochemical staining.....	24
2.13.1 Bone morphogenetic protein-2 (BMP2) stain	24
2.13.2 Osteoprotegerin (OPG) and Receptor activator of NF-kB ligand (RANKL) stain	25
2.13.3 Alpha-smooth muscle actin (ASMA) stain	26
2.13.3.1 Preparation of reagents.....	26
2.14 Light microscopic imaging	27
2.15 Bone Histomorphometric analysis	27
2.16 Gene Expression analysis.....	27
2.16.1 RNA isolation.....	27
2.16.2 Primer testing and validation for the target genes.....	28
2.16.3 Quantitative PCR.....	28
2.16.4 Data analysis.....	29
2.17 Time-of-Flight Secondary Ion Mass Spectrometry (ToF-SIM) analysis.....	29
2.18 Embedding of bone slices in Epon	30
2.18.1 Preparation of reagents	31
2.19 Ultramicrotomy.....	32
2.19.1 Semi-thin sections	32
2.19.2 Ultrathin sections	32
2.20 Transmission electron microscopic imaging	33
2.21 Statistical analysis	33
3. RESULTS.....	34
3.1 Clinical observations	34
3.2 Bone mineral density evaluation	34
3.3 Micro-computed tomography analysis	35
3.3.1 Substantial bony bridging of the fracture gap evident by the high healing scores	35
3.3.2 An increased amount of newly formed bone revealed by the quantitative 3D-morphometry	37
3.4 Biomechanical analysis	38
3.4.1 A comparable bone stiffness at both the operated and unoperated femurs	38
3.5 Qualitative and quantitative histology	39
3.5.1 Healing characterised by a dense inter-cortical and trabecular bone bridging	39
3.5.2 Major matrix mineralisation as evident by an increased amount of mineralised bone area	41
3.5.3 Increased number of regularly organised osteocytes-lacunae canaliculi network	43

3.6 Qualitative and quantitative enzyme histochemistry	44
3.6.1 A significantly higher cellular expression of ALP in the operated femur	44
3.7 Qualitative and quantitative immunohistochemistry	45
3.7.1 A moderate amount of BMP2, OPG, RANKL and a reduced ASMA count	45
3.8 Gene expression analysis	47
3.8.1 Up-regulation of prominent genes involved in bone formation	47
3.9 Bone surface analysis using ToF-SIMS	49
3.9.1 Calcium and collagen surface mapping revealed similar intensity distribution	49
3.10 Ultrastructural analysis of the newly formed trabeculae	50
3.10.1 The localisation of the ROIs for further ultrastructural analysis.....	50
3.10.2 Ultrastructure of the organic matrix and the bone mineral material.....	52
3.10.3 Ultrastructure of the osteoclasts.....	53
3.10.4 Ultrastructure of the osteoblasts	54
3.10.5 Ultrastructure of the osteocytes.....	55
4. DISCUSSION	56
4.1 Successful establishment of a metaphyseal fracture model in the distal femur of skeletally matured sheep	56
4.2 Validation of the BMD in the study animals	57
4.2.1 A comparable BMD at the whole body and femur region of the sheep.....	57
4.3 Characterisation of bone healing in the fractured area	57
4.3.1 Bone microstructure	57
4.3.2 Bone mineralisation and stiffness	59
4.3.3 Cellular activities of osteoclasts, osteoblasts and osteocytes	59
4.3.4 Vascularisation.....	61
4.3.5 Activities of prominent bone formation and resorption genes.....	61
4.3.6 Characteristic ultrastructure of the organic, inorganic and the specialised bone cells	62
4.4 Limitations of the study	63
5. CONCLUSION	64
6. REFERENCES	65
THESIS DECLARATION	74
ACKNOWLEDGEMENTS	75
CURRICULUM VITAE	Error! Bookmark not defined.

LIST OF FIGURES

Fig. 1. A schematic representation of long bone anatomy.....	1
Fig. 2. Diagrammatic representation of the experimental design.....	10
Fig. 3. Internal fixation of the custom-made locking plate and full osteotomy at the sheep distal femur metaphysis.....	12
Fig. 4. Creation of ROI for the 3D-quantitative morphometry.....	17
Fig. 5. The location of indentation points for biomechanical testing.....	18
Fig. 6. Assessment of the bone stiffness via indentation test.....	19
Fig. 7. Postoperative X-ray analysis of the operated femur.....	34
Fig. 8. Evaluation of the BMD.....	35
Fig. 9. Micro-CT image evaluation of the healing status of all six sheep at 12 weeks post-fracture.....	36
Fig. 10. Qualitative evaluation of the degree of bone healing.....	37
Fig. 11. Quantitative micro-CT image analysis.....	38
Fig. 12. Assessment of the biomechanical competence of the newly formed bone.....	39
Fig. 13. Microstructural features of the newly formed cortical and trabecular bone in the fractured area.....	40
Fig. 14. Major bone matrix mineralisation as evidence of advanced bone healing.....	42
Fig. 15. Increased number of well-organised spherically shaped osteocytes-lacunae with the canaliculi network as proof of the new bone maturation.....	43
Fig. 16. Bone formation in the fractured area evident in the significantly higher activity of the osteoblasts.....	45
Fig. 17. Comparative expression of BMP2, OPG, RANKL and ASMA.....	46
Fig. 18. Relative expression of prominent bone formation and resorption genes	48
Fig. 19. The local distribution pattern of calcium and collagen in the fractured area.....	49
Fig. 20. The localisation of ROIs in the fractured area for further ultrastructural analysis.....	51
Fig. 21. Ultrastructure of the organic matrix and the bone mineral material.....	52
Fig. 22. Ultrastructure of the osteoclasts.....	53
Fig. 23. Ultrastructure of the osteoblasts.....	54
Fig. 24. Ultrastructure of the osteocytes.....	55

LIST OF TABLES

Table 1: A comprehensive literature review of the available sheep long bone fracture models for studies on diaphyseal and metaphyseal bone healing.....	5
Table 2: Sample embedding in Technovit 9100.....	14
Table 3: The radiographic image grading scale.....	16
Table 4: The various staining methods with the allocated bone section number.....	19
Table 5: The forward and reverse primer sequence of the target genes.....	28
Table 6: Sample embedding in Epon.....	30

LIST OF ABBREVIATIONS

%	Percentage
°C	Degree Celsius
µm	Micrometre
µM	Micromolar
3D	Three-dimension
AgNO ₃	Silver nitrate
ALP	Alkaline phosphatase
ASMA	Alpha-smooth muscle actin
B2M	Beta-2 microglobulin
BGLAP	Osteocalcin
BMD	Bone mineral density
BMP2	Bone morphogenetic protein-2
Bp	Base pair
BV	Bone volume
BV/TV	Bone volume over the total volume
Ca ⁺	Calcium ion
cDNA	Complementary deoxyribonucleic acid
COL1A1	Collagen, type 1, alpha 1
COL2A1	Collagen, type 2, alpha 2
C _T	Cycle threshold
CTSK	Cathepsin K
DEXA	Dual Energy X-ray Absorptiometry
dH ₂ O	Distilled water
ddH ₂ O	Double-distilled water
F	Force
G	Gram
H ₂ O	Water
HA	Hydroxyapatite
IFM	Interfragmentary movement
Kg	Kilogram
M	Molar
Mbar	Millibar

List of Abbreviations

Mg	Milligram
micro-CT	Micro-computed tomography
N	Newton
obs	Osteoblasts
ocs	Osteocytes
ocy	Osteocytes
OPG	Osteoprotegerin
PCR	Polymerase chain reaction
RANKL	Receptor activator of nuclear factor kappa-B ligand
RNA	Ribonucleic acid
ROI	Region of interest
RT	Room temperature
SMI	Structural mass index
Tb.N	Trabecular number
Tb.Sp	Trabecular spacing
Tb.Th	Trabecular thickness
TEM	Transmission Electron Microscopy
ToF-SIMS	Time-of-Flight Secondary Ion Mass Spectrometry
TRAP	Tartrate-resistant acid phosphatase
v/v	Volume per volume

1. INTRODUCTION

1.1 Bone structure, composition and function

The bones of the skeleton generally function in providing structural and movement support, protection of vital internal body organs, and as a storehouse of growth factors, cytokines, minerals, and hematopoietic stem cells [1], [2]. The long bones of the lower extremity are mostly subjected to load bearing activities and thus, crucial for skeletal movement [3]–[5]. The long bone is composed of a hollow shaft also known as the diaphysis, a rounded epiphysis lying above the growth plate and a cone-shaped metaphysis located underneath the growth plate. The diaphysis primarily consists of dense cortical bone, while the metaphysis and epiphysis are majorly composed of trabecular bone also called cancellous or spongy bone surrounded by a relatively thin layer of cortical bone as shown in figure 1.

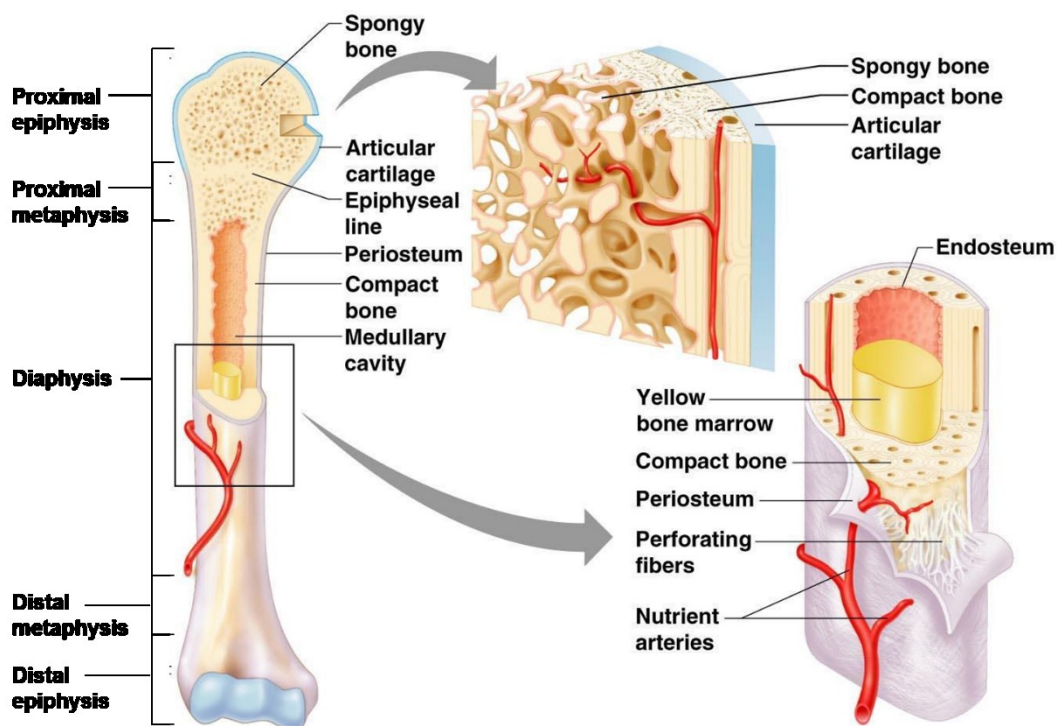


Fig. 1: A schematic representation of long bone anatomy. The diaphysis is consists of dense cortical bone whereas the epiphysis and metaphysis comprise majorly of trabecular bone (modified from <http://docplayer.net/28369321-The-skeletal-system-musculo-skeletal-system.html>; accessed on 02.2.2019).

The outer surface of the cortical bone is attached to a thick fibrous (Sharpey's fibres) periosteal layer that serves as a protective sheath while providing support to tendons, which secure the muscle to the bone. The osteogenic layer of the periosteum contains progenitor cells that can develop into bone forming cells. Enclosed within the cortical

bone is a porous network of trabeculae, surrounded by a hollow cavity containing the bone marrow. The endosteum covers the inner surface of the cortical, trabecular, and blood vessel canals. The cortical bone is composed primarily of osteons of concentric lamellae arranged in Haversian canal whereas the trabecular bone is primarily composed of thin plates and rod-shaped structural units called trabeculae packets arranged in a mosaic-like microstructure. The trabecular bone has a lower stiffness, larger surface area to volume ratio and shows a higher metabolic rate [2], [6]–[8].

The bone matrix is made up of organic and inorganic components. The fibrillar type 1 collagen dominates the organic component whereas the inorganic component is mostly carbonated hydroxyapatite $[\text{Ca}_{10}(\text{PO}_4)_6(\text{OH})_2]$ [9]–[11]. The collagenous fibres appear very dense containing regularly arranged fibrils that are oriented in parallel and reinforced with the mineral particles deposited within and outside the structure [12], [13]. The mineral phase determines the stiffness, while the collagen component controls its post-yield ductility. By combining the unique mechanical properties, the collagen-mineral composite contributes to bone's strength by providing both rigidity and resistance against the applied load. The mechanical property of a bone is also determined by the density and distribution pattern of the mineral within the collagenous matrix as well as the structural organisation of the tissue both at the micro and nano-structural levels [14], [15]. Specific types of bone cells, namely osteoblasts, osteoclasts and osteocytes with unique morphological features occupy defined an area within the bone matrix. In response to physiological or mechanical forces, they perform defined roles during osteogenesis, bone modelling and remodelling processes.

1.2 Healing process of diaphyseal and metaphyseal fractures

The healing of a diaphyseal fracture in the cortical bone area is a complex multi-step process that combines both intramembranous and endochondral ossification. It is characterised by periosteal callus formation, in which the amount of callus depends on the stability of the fracture fixation [16]–[18]. In contrast, the healing of a metaphyseal fracture in the trabecular bone area under mechanically stable conditions occurs more rapidly, mainly through a direct membranous bone formation within the marrow space, and with very little or no external callus formation [19]–[23]. The inter-trabecular healing process begins with the formation of a hematoma, which subsequently leads to an inflammatory stage that is succeeded by a large assembly of undifferentiated

mesenchymal stem cells developing into the osteoid tissue, which then transforms into the woven bone that is later remodeled into lamellar bone [19]–[24]. Most trabecular fractures of the lower body extremity for example, in the distal femur, occur in the metaphyseal bone area. This is because trabecular bone density and strength decreases with ageing and in the disease condition, thus making it highly susceptible to fracture [25].

1.3 Large animal models for fracture healing study

Although small animal models are most often used for fracture healing studies, they have several shortcomings when compared to larger animals. Some of the limiting factors include their small skeletal size, bone structure and limited life expectancy [26]–[28]. These drawbacks are addressable using large animal models. Among previously tested larger animals such as goats, pigs, dogs and non-human primates, sheep are the best choice with respect to orthopaedic research [29], [30]. These studies found many similarities between sheep skeleton and human subject in terms of size, microstructure, bone metabolism and mechanical properties [29], [31]–[33]. The use of skeletally matured sheep as a large animal model for fracture healing studies have been reported to be more clinically relevant in comparison to small animals because the results are more likely translatable to the human subject. Also, the large size and shape of the sheep skeleton allow the use of orthopaedic implants comparable to those used in patients [34], [35].

Although several fracture healing studies have been conducted using sheep, most of the defects were created in the diaphyseal area of the long bone as shown in table 1. This contrasts with the clinical situation where most fractures occur in the metaphyseal region. Based on the extensive literature review (Table 1), only three studies are available on metaphyseal bone healing using sheep models. In one of those studies, Malhotra et al. 2014 [36] compared the healing rate of different drill hole defect sizes (8 mm, 11 mm and 14 mm) created in the proximal tibia and distal femoral epiphysis of young and adult sheep. In the other two studies, a 3 mm partial osteotomy was created in the trochlear groove of the distal femur in skeletally matured sheep [37] and osteoporotic sheep [38]. Despite having interesting experimental outcomes, the models mentioned above are somewhat limited by the lack of full discontinuity of the bone at the fracture area and the absence of a clinically relevant fixation technique

owing to the simple nature of the fracture, which is often not the case with clinical fractures. Based on current literature review, a complete osteotomy at the metaphysis and a proper internal fixation are among the main criteria required for an animal model to be considered as clinically relevant for metaphyseal bone healing study [39], [40].

Table 1: A comprehensive literature review of the available sheep long bone fracture models for studies on diaphyseal and metaphyseal bone healing.

Experimental study	Sheep breed and age	Healthy or diseased condition	Defect size and location	Fracture fixation method	Study duration	Healing outcome
Wullschlegel <i>et al.</i> , 2013 [41]	Merino 5.6 ± 0.9 years	Healthy	3 cm multi-fragmentary shaft fracture of the distal femur (A0 - C3 fracture).	External fixator	4 and 8 weeks	Callus bridging was observed at the fracture gap.
Lill <i>et al.</i> , 2003 [42]	Female Swiss mountain 7.5 ± 1.5 years	Osteoporotic	3 mm transverse midshaft osteotomy on the distal tibia.	External fixator	8 weeks	The osteoporotic group had reduced healing compared to sham.
Challis <i>et al.</i> , 2006 [43]	Not provided	Healthy	Transverse osteotomy of the right distal radius.	External fixator	4 and 6 weeks	Addition of cyclic pneumatic pressure did not significantly increase healing outcome compared to the control group.
Epari <i>et al.</i> , 2006 [44]	Female merino 2.5 – 3-5 years	Healthy	3 mm osteotomy on the tibial diaphysis.	External fixator (rigid and semi-rigid)	6 and 9 weeks	The use of semi-rigid fixator increased healing time leading to prolonged chondral phase.
Tufekci <i>et al.</i> , 2018 [45]	Merino 3 - 4 years	Healthy	3 mm and 30 mm critical-sized defect separated by a 30 mm bone segment.	External fixator	9 weeks	Early mechanical stimulation alone is sufficient for a timely healing outcome.

Table 1 continued

Experimental study	Sheep breed and age	Healthy or diseased condition	Defect size and location	Fracture fixation method	Study duration	Healing outcome
Hente <i>et al.</i> , 1999 [46]	Female Swiss Alpine 6 – 11 years	Healthy	3 mm osteotomy of the anterior aspect of the tibia.	External fixator (static and dynamic fixation).	10 weeks	No significant differences between dynamic and static fixation groups.
Augat <i>et al.</i> , 2001 [47]	Male merino 1.8 – 2.5 years	Healthy	Transverse osteotomy of the right tibia at the mid-diaphyseal level.	External fixator with controlled interfragmentary movement (IFM).	9 weeks	Externally applied mechanical stimulation with cyclic non-uniform tensile strains did not enhance healing.
Claes <i>et al.</i> , 1995 [48]	Male sheep 2 years	Healthy	0.6 mm transverse osteotomy of the right metatarsal.	External fixator with controlled IFM.	9 weeks	Dynamic fixation accelerated healing. However, bone healing was more dependent on gap size rather than IFM.
Wolf <i>et al.</i> , 1998 [49]	Female merino sheep	Healthy	3 mm transverse osteotomy of the left tibia.	External fixator with controlled IFM.	6 weeks	External mechanical stimulation did not enhance healing. IFM of about 0.5 mm seemed to be the optimal distance to support healing.

Table 1 continued

Experimental study	Sheep breed and age	Healthy or diseased condition	Defect size and location	Fracture fixation method	Study duration	Healing outcome
Claes <i>et al.</i> , 2009 [19]	Mountain 6 years	Healthy	3 mm partial osteotomy in the trochlear groove of the distal femur.	Two stainless-steel plates with a thickness of 2 and 2.7 mm were implanted to limit IFM.	8 weeks	Smaller IFM resulted in better healing outcome compared to larger IFM.
Bindl <i>et al.</i> , 2013 [38]	Merino 5 – 6 years	Osteoporotic	3 mm partial osteotomy in the trochlea region of the distal femur.	Two stainless-steel plates with a thickness of 2 and 2.7 mm were implanted to limit IFM.	8 weeks	Hypothalamic-Pituitary Disconnection (HPD) treated group had a poor healing outcome.
Malhotra <i>et al.</i> , 2014 [36]	18 months and 5 years	Healthy	Distal femoral epiphysis and proximal tibial epiphysis. Drill hole defects with a fixed depth of 25 mm and diameter of 8 mm or 11 mm or 14 mm.	None.	4 weeks	Healing decreased as defect size increased. The defect areas were only partially healed due to the short observation time.

1.4 Aim and objectives of the study

The high incidence of metaphyseal fracture in the world's ageing population makes it a serious clinical concern, especially since there are limited treatment options available. Therefore, there is an urgent need for appropriate large animal models that fulfil specific clinical criteria to enable translational studies on metaphyseal fracture healing.

The goal of this doctoral research work is to establish and extensively characterise a clinically relevant metaphyseal fracture model in adult sheep distal femur. The full discontinuity at the metaphysis and the adequate internal stabilisation conferred by the titanium locking plate fixation comparable to the clinical situation met the criteria expected of a clinically relevant animal model.

The objectives of this study include:

- 1.** To determine whether the customised anatomical locking plate construct conferred sufficient mechanical stability on the fractured gap under mechanical loading conditions.
- 2.** To quantify the extent of healing that occurred in the fractured area within the 12 weeks observation period.
- 3.** To determine the nature of the tissue formation and whether the trabecular healing occurred via intramembranous or endochondral ossification.
- 4.** To determine the biomechanical competence of the newly formed bone.
- 5.** To extensively characterise the structural features of the organic, inorganic and cellular components of the newly formed trabeculae up to the nanometer scale.

2. MATERIALS AND METHODS

2.1 Ethics statement

The local animal care committee approved this study according to the German animal protection laws of the District Government of Darmstadt under the reference number V 54-19 c 20/15 - FU/1061. All the animals were handled in conformity with the guidelines for care and use of laboratory animals of the National Institutes of Health.

2.2 Experimental design

This study was conducted using six female adult Merino land sheep aged between 6 - 7 years and an average weight of 99 kg. The animals were fed with a standard sheep diet (S6189-S010; ssniff-Spezialdiäten, Germany) and they grazed freely at the meadow. The bone mineral density (BMD) of the animals was measured using Dual Energy X-ray Absorptiometry (DEXA) two weeks after acclimatisation to the new environment. Subsequently, the femoral osteotomy on the left distal femur metaphysis was performed, and then the fracture was allowed to heal for 12 weeks. The matching right femurs were left intact and used as the experimental control. Just before the animals were euthanised for sample collection, their final BMD measurement was recorded. The left and right distal femur areas were harvested for further analysis using various methods as shown in figure 2. All the procedures including the DEXA, femoral osteotomy and euthanasia were carried out under general body anaesthesia, which was performed via intravenous administration of 2 mg/kg propofol (20 mg/mL propofol; Fresenius Kabi, Germany) and 2 mg/kg fentanyl (50 mg/mL Fentanyl-Hameln; Hameln Pharmaceuticals GmbH, Germany).

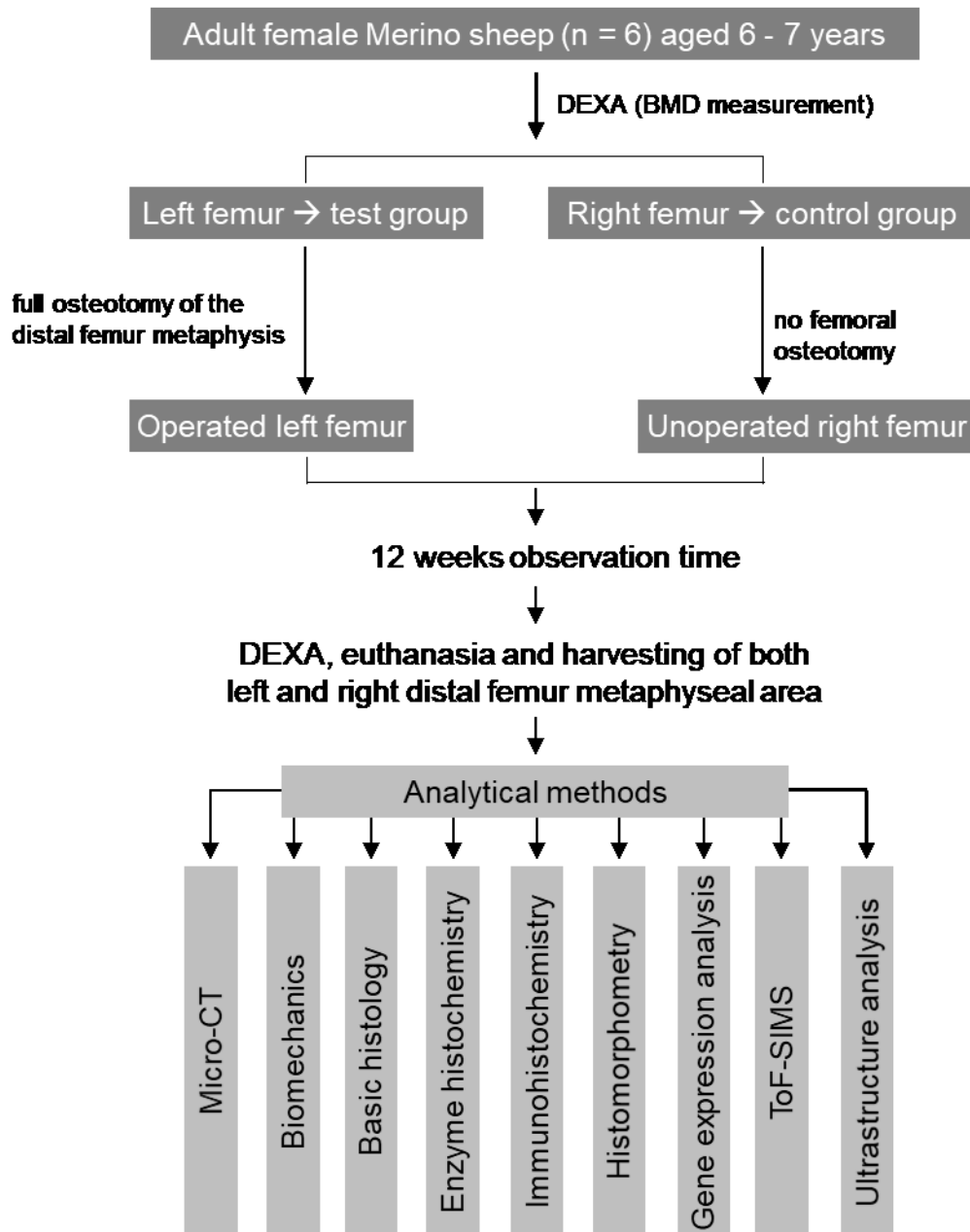


Fig. 2. Diagrammatic representation of the experimental design.

2.3 Bone mineral density (BMD) measurement using DEXA

The BMD of each animal was measured before the femur osteotomy and at 12 weeks post-surgery using the DEXA machine (Lunar Prodigy, GE Healthcare, Germany). The measurement was done after the standard machine calibration as described in the manufacturer's protocol. The measured BMD of the whole-body region, operated left and unoperated right femurs of the animals were analysed using the large animal mode of the enCORE software (version 13.40).

2.4 Surgical procedure of the femur osteotomy

A complete wedge-shaped osteotomy was created in the distal metaphyseal area of the left femur under general body anaesthesia as described below:

Each sheep was laid in a supine position, and the hind legs were fixed in a slightly extendable position to enable proper internal rotation. The left hind leg to be operated was shaved entirely from the thigh region down to the knee area. Subsequently, the surgical site and the lower body part were fully draped sterile. Incisions were made to expose the lateral femur from the lateral condyle area into the midshaft area between the lateral vastus muscle, and the lateral head of the femoral biceps muscle. Proper care was taken to avoid the disruption of the surrounding collateral ligaments. Two blunt Hohmann retractors were used to expose the femoral shaft, and the soft tissues around the osteotomy site were carefully removed.

For a stable fixation of the distal femur, a custom-made angular stable 11-hole titanium plate (aap Implantate, Germany) was inserted into the lateral side of the distal femur (Fig. 3A-B). Care was taken to fix the locking plate to the distal femur just proximal to the joint line of the knee joint, and a non-locking screw (aap Implantate, Germany) was used to fix the plate onto the lateral cortex via the oval hole. Six 50 mm long locking screws (aap Implantate, Germany) were fixed into the distal part of the plate with penetration from the medial cortex without violation of the cartilage or other intraarticular structures (Fig. 3C). The remaining four locking screws holes were fixed into the diaphyseal region.

Afterwards, the patella was gently dislocated with the aid of blunt Hohmann retractors that exposed the ventral aspect of the distal femur. A line just proximal and parallel to the articular cartilage was marked. At the lateral aspect of the distal femur, the line was extended 10 mm proximally and connected to the medial origin of the line resulting in a triangular/wedge-shaped guideline for subsequent sawing. The osteotomy was carried out using a motorised oscillating saw. The exercised bone was chiselled out, then the defect (Fig. 3D) was cleaned and flushed with saline to remove residual bone particles. Multiple layered soft tissues and skin closure were performed using resorbable stitches. A spray silver dressing was applied to prevent infection. The stable angular fixation of the fracture permitted the immediate post-operative full-weight bearing of the animals.

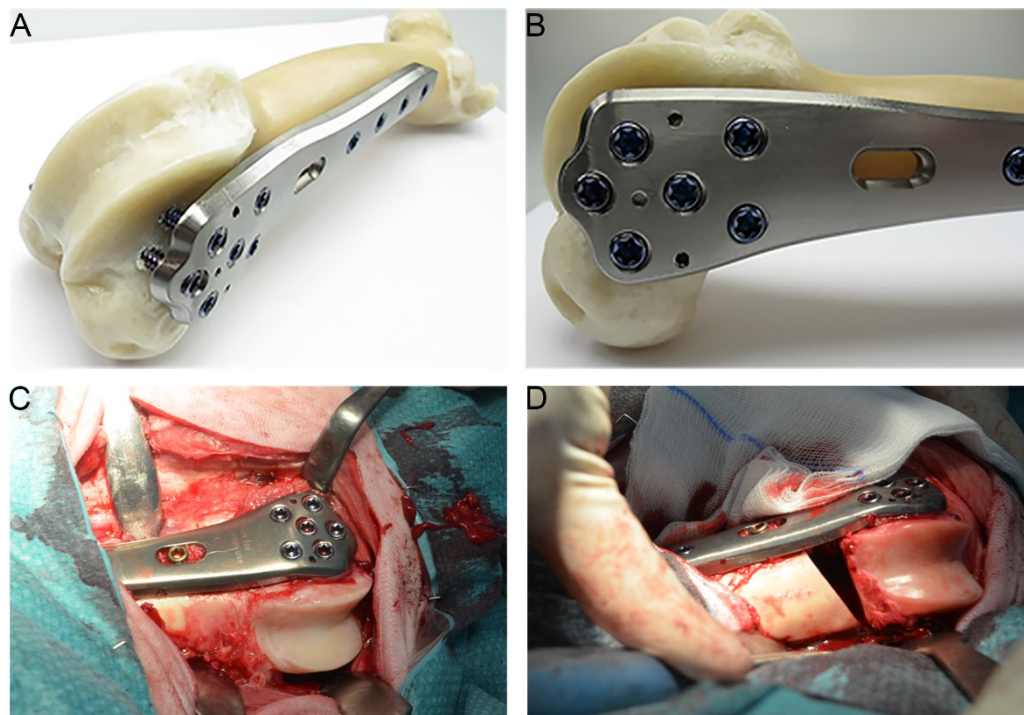


Fig. 3. Internal fixation of the custom-made locking plate and full osteotomy at the sheep distal femur metaphysis. (A) Overview image of the customised titanium locking plate for fixation of the distal metaphyseal area of the femur (B) The condylar part of the plate allows for stable fixation of the distal femur with six 50 mm long locking screws. (C) Intraoperative image after fixation of the locking plate to the lateral part of the left femur with stable fixation of the locking screws into the condylar area before the osteotomy. (D) Intraoperative appearance after the creation of the wedge-shaped osteotomy with a full discontinuity at the distal metaphyseal area of the femur.

2.5 Post-operative follow-up

The animals were kept individually for one week to ensure proper wound healing and for the rest of the observation period in a flock on a nearby meadow with the standard diets and water ad libitum. The overall health status and wound healing were checked daily during the first two postoperative weeks by a veterinarian. The postoperative monitoring included the administration of relevant analgesics, observation of weight bearing and return to daily activities. Subsequently, the animals were monitored weekly until the end of the study period. Postoperative X-ray of the femur was performed one day after the surgery without additional anaesthesia to ascertain if the metallic implant was correctly placed and to exclude any additional peri-implant fractures of the femur.

2.6 Euthanasia and Sample harvesting

All animals were euthanised at 12 weeks post-surgery by intravenous administration of 50 mg/kg pentobarbital (Anestesal; Pfizer, Germany) under anaesthesia as described above. After euthanasia, both the left and right femurs were harvested from the animals. The femurs were carefully cleaned of any unwanted soft tissues in contact with the cortical bone surface, and the plates were carefully removed from the femurs. All the harvested femurs remained stable after the plate removal, and no plate breakage was recorded. The distal end of the operated left and unoperated right femurs of the six sheep were harvested and sectioned into thin coronal bone slices using a diamond saw (Trennband 0.2 mm; Patho-service Germany) under constant cooling and then assigned to the various analytical methods. For biomechanical analysis, coronal bone slices of about 4.5 mm thickness were immediately frozen without processing to avoid any alteration in bone quality. About 3 mm thick coronal bone slices were allocated for gene expression and ultrastructure analysis. The samples for gene expression analysis were immediately placed in RNAlater (1204027, Ambion, USA), and stored at -80 °C until further processing. Another 4.5 mm thick coronal bone slices were allocated for both micro-CT analysis and histological staining since micro-CT is a non-destructive technique. The bone specimens were immediately fixed in 4 % phosphate-buffered paraformaldehyde (Carl Roth, Germany) and stored at 4 °C until further processing.

2.7 Embedding of bone slices in Technovit 9100

Technovit 9100 New (Heraeus Kulzer, Germany) is a plastic embedding system based on methyl methacrylate (MMA). The undecalcified femoral bone slices were embedded in the Technovit 9100 New. This embedding technique enabled the investigation of the samples using various histological staining, enzyme-histochemistry and immunohistochemistry. The reagent was supplied as five components consisting of:

1. Technovit 9100 basic solution of stabilised MMA. This component was destabilised by passing the reagent slowly through a column filled with approximately 50 g of aluminium oxide (X908, Roth, Germany). The destabilised solution was stored at -20 °C in corked brown glass.
2. Technovit 9100 PMMA powder was used to eliminate polymerisation shrinkage and facilitate a better polymerisation process.

3. Technovit 9100 hardener 1 and hardener 2 worked together to facilitate targeted polymerisation even at temperatures less than 0 °C.
4. Technovit 9100 regulator is a reactive organic compound that facilitates a precise polymerisation with controlled low-temperature spikes.

The embedding process was performed in two steps, namely tissue pre-treatment and tissue treatment. In the tissue pre-treatment phase, the harvested samples were fixed in 4 % paraformaldehyde for 24 - 48 hours followed by six rounds of washing with 0.1 M phosphate buffer, pH 7.3. The tissue treatment stage involved sample dehydration in increasing concentration of ethanol (32205, Sigma, Germany), then in an intermedium which involved defatting with xylene (9713, Roth, Germany) and lastly the immersion stage where the samples were embedded in Technovit. Table 2 below describes how the sample treatment phase was performed.

Table 2: Sample embedding in Technovit 9100.

Duration and temperatures for the tissue treatment phase of the sheep femoral bone slices.

Treatment phase: Dehydration, intermedium and immersion		
Dehydration in Ethanol		
Concentration	Duration	Temperature
70 %	2 days	RT
70 %	2 days	RT
80 %	3 days	RT
96 %	3 days	RT
100 %	4 days	RT
100 %	3 days	RT
100 %	4 days	RT
100 %	3 days	RT
100 % p.a.	4 days	RT
Intermedium in Xylene		
Concentration	Duration	Temperature
100 %	6 hours	RT
100 %	12 hours	RT
Immersion in Technovit 9100		
Reagent	Duration	Temperature
Pre-infiltration 1	5 days	RT
Pre- infiltration 2	5 days	RT
Pre- infiltration 3	5 days	4 °C
Infiltration 1	6 days	4 °C
Infiltration 2	6 days	4 °C
Infiltration 3	6 days	4 °C
Polymerisation	2 days	- 4 °C
Polymerisation	1 hour	4 °C

Key: RT: room temperature; °C: degree Celsius

2.7.1 Preparation of reagents

- ❖ Pre-infiltration 1: 200 ml Xylene + 200 ml Technovit 9100 stabilised basic solution.
- ❖ Pre-infiltration 2: 200 ml stabilised Technovit 9100 basic solution + 1 g hardener 1.
- ❖ Pre-infiltration 3: 200 ml destabilised Technovit 9100 solution + 1 g hardener 1.
- ❖ Infiltration solution 1 - 3: 250 ml destabilised Technovit 9100 solution + 20 g PMMA powder + 2 g hardener 1.
- ❖ Polymerisation mixture: 9 parts of stock solution A + 1 part of stock solution B.
 - Solution A: 500 ml destabilised Technovit 9100 solution + 80 g PMMA powder + 3 g hardener 1.
 - Solution B: 44 ml destabilised Technovit 9100 + 17.6 ml hardener 2 + 2 ml regulator.
- ❖ Phosphate buffer, pH 7.3
 - Solution A: 27.6 g Sodium dihydrogen phosphate monohydrate (106346, Merck, Germany) in 1000 ml ddH₂O.
 - Solution B: 35.6 g di-Sodium hydrogen phosphate dihydrate in 1000 ml ddH₂O.
 - Stock solution (0.2 M Na-phosphate, pH 7.3): 230 ml solution A + 770 ml solution B.
 - Working solution (0.1 M Na-phosphate, pH 7.3): 500 ml stock solution + 500 ml ddH₂O.

2.8 Micro-computed tomography (micro-CT) analysis

2.8.1 Scanning procedure

The Technovit-embedded coronal bone slices were scanned using a Bruker micro-CT (SkyScan 1173, Kontich, Belgium) at the X-ray energy of 130 kV and 60 μ A for assessment of bone microstructure as described by Bouxsein and colleagues [50]. The samples were positioned on a computer-controlled rotation stage and scanned at 240° around the vertical axis in rotation steps of 0.25° with a noise reduction, and a frame average of 4-fold. A 0.25 mm brass filter was used for beam filtration to reduce beam hardening. A pair of HA-phantoms with a diameter of 32 mm and mineral densities of

250 mg / 750 mg HA was scanned with each scan for system calibration of linear attenuation coefficient to the density of HA. The images were reconstructed with the NRecon-Software (Bruker microCT, Kontich, Belgium), resulting in an 8-bit grayscale image. A Gaussian filter (kernel = 1) was employed for image reconstruction with a moderate smoothing.

2.8.2 Micro-CT image post-processing and data acquisition

The qualitative assessment of the generated micro-CT images of the bone specimens of the operated left femurs was performed by two independent investigators to determine the extent of bony bridging at both the cortical and trabecular regions of the fractured area. The examination was conducted with the Sykscan Dataviewer software for 3-dimensional (3D) image analysis. The 3D images of the bone slices were orientated in a similar direction before the assessment. Next, the fractured area was divided into the following three parts: medial cortex, defect centre and, lateral cortex. Healing at these regions were graded using the radiographic grading scale shown in table 3, which was adapted from previous reports [36], [51]. The images were reviewed in transverse, coronal as well as sagittal planes to ensure a thorough and precise assessment. The sum of the grades was used to determine the healing status of each specimen.

Table 3: The radiographic image grading scale.

0	No healing: No visible bone bridging within the fractured area.
1	Partial cortical and trabecular healing: Minor bone bridging with gaps; defect visible with low radiographic density than adjacent bone outside the fractured area.
2	Advance cortical and trabecular healing: Bone bridging evident with minimal gaps; defect visible with radiographic density fairly like that of adjacent bone outside the fractured area.
3	Complete cortical and trabecular healing: Bone bridging with no gaps; defect hardly visible with a radiographic density equivalent to the adjacent bone outside the fractured area.

For the quantitative analysis, a direct 3D-morphometry of the newly formed trabeculae of the operated left femurs was analysed relative to the unoperated right femurs. The creation of a region of interest (ROI), segmentation and quantitative morphometry were performed using the CTAn Software (Version 1.18.4, Bruker microCT, Kontich, Belgium). A triangular/wedge-shaped ROI was manually contoured within the fractured

area of the operated left femurs and at the comparable region in the unoperated right femurs (Fig. 4A-B).

The cortical bone region was excluded from the ROI. The height of the wedge at the lateral and medial sides of each bone sample was about 10.5 mm and 0.5 mm, respectively. The contoured wedge was interpolated into a defined specimen volume. For the trabecular bone morphometry, a global threshold of 30 % of the maximum grey values corresponding to a mineral density of 400 mg HA/cm³ was defined. The analysis method was adapted from previous reports [52], [53].



Fig. 4. Creation of ROI for the 3D-quantitative morphometry. Representative images of (A) operated left and (B) unoperated right femur showing the wedge-shaped ROI defined only at the trabecular bone area.

2.9 Biomechanical analysis

The stiffness of the trabecular and cortical regions within and adjacent to the fractured area was determined using an indentation test. The indentation test was performed on non-processed fresh coronal bone slices by Prof. Dr. L. Dürselen, a collaborating partner at the Institute of Orthopaedic Research and Biomechanics, University of Ulm, Germany (Institute director: Prof. Dr. A. Ignatius). Similar points were also measured from the corresponding unoperated right femur to enable comparison. The samples were marked at nine points with a water-insoluble pen as shown in figure 5. Points 2,5,7,8 and 9 were within the osteotomy area; points 1 and 3 were around the cortical region while points 4 and 6 were located within the trabecular region adjacent to the fractured area. The indentation test was performed on the marked points using a standard material test machine (Z10, Zwick Roell, Germany) as shown in figure 6A.

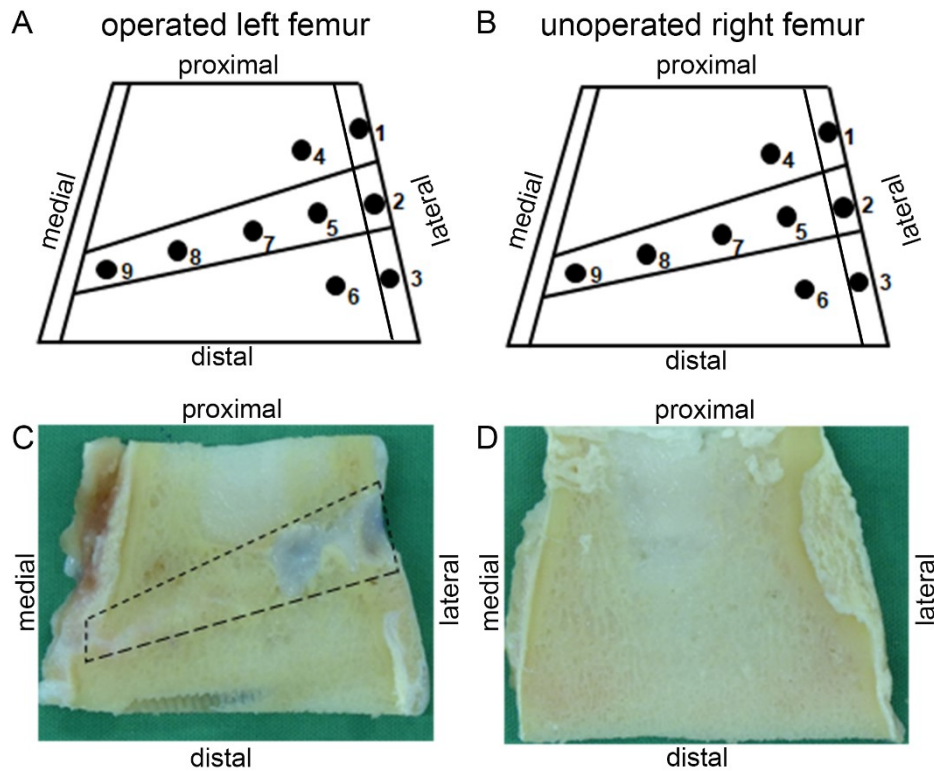


Fig. 5. The location of indentation points for biomechanical testing. Schematic representation of the operated left femur (A) and unoperated right femur (B) showing the measurement locations on the bone slice. Overview images of coronal bone slices of the operated left femur (C) and (D) unoperated contralateral side. The wedge-shape outlined the former fracture area.

The machine was fitted with a force sensor (500 N maximum load, KAF-Tw, A.S.T., Germany) and the deformation was measured with a laser distance sensor (IL-D220-20, Mikro-Epsilon, Germany). The samples were placed on a flat surface and kept moist throughout the test using sodium chloride. After applying a preload of 5 N with a stamp of 2.6 mm diameter, the indentation test was conducted at a constant deformation rate of 1 mm/min. The measurement was either automatically terminated if the sample failed to withstand the applied force or when a compressive force of 120 N was reached. The stiffness (slope) in Nmm^{-1} was calculated from the linear part of the force-deformation curve (Fig. 6B). This occurred at an indentation depth of maximally 10 % of the sample height for trabecular bone and around 2 % of the sample height for cortical bone using the following formula:

$$\text{Slope } (\text{Nmm}^{-1}) = \frac{F_{\text{high}} \text{ in } N - F_{\text{low}} \text{ in } N}{dL(F_{\text{high}}) \text{ in } mm - dL(F_{\text{low}}) \text{ in } mm}$$

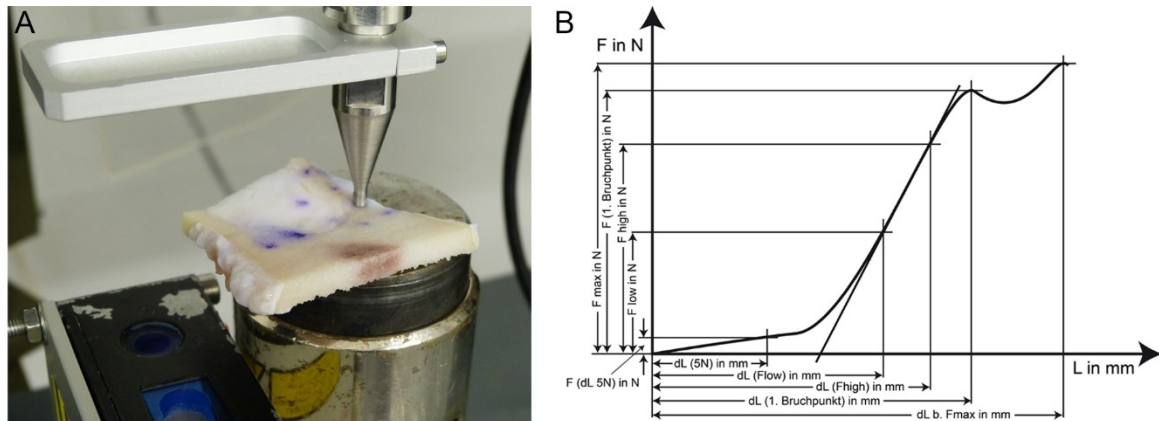


Fig. 6. Assessment of the bone stiffness via indentation test. (A) The overview image showed an indentation point on the cortical region of a coronal bone slice. (B) Schematic diagram of a force-deformation plot of a given sample after the indentation test.

2.10 Bone sample grinding and sectioning

The undecalcified Technovit embedded bone slices were partly ground and polished into about 70 μm thick grinding using a cutting-grinding machine (Exakt-300, EXAKT Advanced Technologies Germany). Then the remaining Technovit blocks were trimmed and divided into two halves of lateral and medial sides to enable sectioning using the 2.5 cm Kawamoto's film (Cryofilm type 2C(9), Section-Lab Co. Ltd., Japan). Five micrometres thick sections were prepared with the aid of a microtome (RM2155, Leica, Germany) equipped with a hard-metallic knife (400215, Leica, Germany). Consecutive sections were used for the various staining as shown in table 4.

Table 4: The various staining methods with the allocated bone section number.

Staining method	Section number
Von-Kossa van-Gieson	6
Alpha-smooth muscle actin	7
Silver nitrate	8
Alkaline phosphate	9
Tartrate-resistant acid phosphatase	10
Bone morphogenetic protein-2	11
Receptor activator of NF-kB ligand	12
Osteoprotegerin	13

2.11 Histological staining

2.11.1 Trichrome Masson-Goldner stain

The undecalcified bone grindings were stained with trichrome Masson-Goldner to investigate the healing quality and general tissue appearance within the fractured area as described below.

The samples were deplastified for two days in two changes of 2-methoxyethyl-acetate (8.06061, Merck Germany). Later, the samples were rehydrated in decreasing ethanol series namely, 100 %, 96 % and 70 % each for five minutes and then for five minutes in distilled water. Then, the samples were incubated in Weigert's iron hematoxylin A + B (X906/ X907, Roth, Germany) for three minutes, washed under running tap water for ten minutes to develop the blue colouration. The samples were incubated for five minutes in a freshly prepared Masson solution made from Fuchsin-Ponceau-Azophloxin compounds. Afterwards, the samples were rinsed in 1 % acetic acid (9372.4, Roth, Germany) and then incubated in Tungstophosphoric acid orange-G solution for 8 minutes and washed in 1 % acetic acid. Finally, the samples were incubated in 0.2 % light green (62110, Fluka, Germany) for eight minutes, rinsed again in 1 % acetic acid and dehydrated very rapidly in 100 % ethanol and then cleared twice in xylene for ten minutes each before mounting in coverslips with Eukitt (03989, Sigma-Aldrich, Germany).

2.11.1.1 Preparation of reagents

- ❖ Weigert's Iron Haematoxylin: 40 ml solution A + 40 ml solution B.
- ❖ Masson Solution (Fuchsin-Ponceau-Azophloxin):
 - Solution A: 1 g Fuchsin-Ponceau Masson (1A-350, Chroma, Germany) in 100 ml dH₂O, bring to boil and add 1 ml glacial acetic acid.
 - Solution B: 1 g Ponceau de Xylidine in 100 ml dH₂O, bring to boil and add 1 ml of glacial acetic acid. Filter the solution before use.
 - Solution C: 0.5 g Azophloxin in 100 ml dH₂O + 200 µl glacial acetic acid.
 - Working solution 1: 3.3 ml solution A + 6.7 ml part solution B + 2 ml solution C + 88 ml 0.2 % glacial acetic acid. Filter the solution before use.

- ❖ Tungstophosphoric acid Orange G Solution: 3 g Tungstophosphoric acid (1.00583, Merck, Germany) + 2 g Orange G (1B-221, Chroma, Germany) in 100 ml dH₂O. Filter the solution before use.
- ❖ 0.2 % Light green: 0.2 g brilliant green + 200 µl glacial acetic acid in 100 ml dH₂O. Filter the solution before use.

2.11.2 Von-Kossa van-Gieson stain

The undecalcified bone sections were stained with von-Kossa van-Gieson to differentiate the mineralised bone area from the osteoid area and to quantify the newly mineralised bone within the fractured area as described below.

The samples were deplastified in three changes of 2-methoxyethyl-acetate (MEA) for 20 minutes per round. Subsequently, the samples were rehydrated in decreasing ethanol series namely, 100 %, 96 % and 70 % each for five minutes and then for five minutes in distilled water. Afterwards, the samples were stained with von-Kossa as follows: incubation in 3 % silver nitrate solution (131459, Applichem, Germany) for five minutes, followed by rinsing in three changes of distilled water and then for about two minutes in 10 % sodium carbonate-formaldehyde solution. The samples were washed under running tap water for ten minutes, then fixed in 5 % sodium-thiosulfate solution (1.06509, Merck, Germany) for five minutes before being rinsed in two changes of distilled water for two minutes each. The samples were contrasted in 0.8 % methyl green solution (5159, Roth Germany) for eight minutes and washed in three changes of distilled water for two minutes each. Then samples were stained with van-Gieson as follows: incubation in Weigert's iron haematoxylin for six minutes, washed under running tap water for ten minutes, followed by immersion in van-Gieson solution (2E-050, Chroma, Germany) for five minutes. Lastly, the samples were dehydrated very quickly in 96 % and 100 % ethanol and cleared in two changes of xylene for five minutes each before mounting in coverslips with Depex (18243.02, Serva, Germany).

2.11.2.1 Preparation of reagents

- ❖ 3 % silver nitrate solution: 3 g of silver nitrate (AgNO₃) in 1000 ml dH₂O.
- ❖ 10 % sodium carbonate-formaldehyde: 10 g sodium carbonate (A315, Roth, Germany) + 25 ml 37 % formaldehyde (104002, Merck, Germany). Bring to 1000 ml with dH₂O.

- ❖ 5 % sodium thiosulphate solution: 5 g sodium thiosulphate in 1000 ml dH₂O.
- ❖ 0.8 % methyl green: 1 g methyl green in 25 ml absolute ethanol.

2.11.3 Silver nitrate stain

The undecalcified Technovit-embedded sections were stained with silver nitrate to visualise the morphology of the osteocyte-lacuna canaliculi network and quantify the osteocytes lacunae within the fractured area as described below.

After sample deplastification and rehydration as described for the trichrome Masson-Goldner stain, the bone sections were decalcified in a solution (pH 7.3) containing 3.4 % Tris (4855, Roth, Germany) and 10 % Titriplex III (1.08418, Merck, Germany) for three days. The samples were incubated in the silver nitrate mixture, containing a 1:2 ratio of solution A and B for 90 minutes in the dark. The samples were rinsed in distilled water for five minutes, followed by ten minutes incubation in a freshly prepared 5 % sodium thiosulfate solution and then five minutes washing in distilled water. The samples were subsequently dehydrated through an ascending ethanol gradient (70 %, 96 % and 100 %) for five minutes each and cleared in two changes of xylene before mounting in coverslips with Depex.

2.11.3.1 Preparation of reagents

- ❖ Solution A: 24.75 ml ddH₂O + 250 µl methanoic acid + 0.5 g gelatin low bloom.
- ❖ Solution B (50 % silver nitrate): 10 g silver nitrate in 20 ml ddH₂O.
- ❖ 5 % sodium thiosulfate solution: 1 g sodium-thiosulfate in 20 ml ddH₂O.

2.12 Enzyme histochemical staining

2.12.1 Alkaline phosphatase (ALP) stain

The undecalcified bone sections were stained with ALP to investigate the activity of osteoblasts in the fractured area. The bone sections were deplastified in MEA and rehydrated in descending series of alcohol as already described above. Next, the samples were treated with 0.1 M Tris-buffer (pH 9.4) for ten minutes and then incubated in ready-to-use 5-bromo,4-chloro,3-indolylphosphate/nitrobluetetrazolium substrate solution (50-81-08, KPL, Germany) using a moist chamber at 37 °C for one hour. Afterwards, the sections were rinsed in three changes of distilled water and

counterstained with nuclear fast red aluminium sulphate solution (N069, Roth, Germany), followed by washing in three changes of distilled water. The stained samples were dehydrated in an ascending series of alcohol and cleared in xylene before mounting with coverslips using Eukitt.

2.12.1.1 Preparation of reagents

- ❖ 1 M Tris-buffer, pH 9.4: 121.1 g Tris in 1 L dH₂O. Adjust pH to 9.4 with 25 % HCl.
 - 0.1 M Tris-buffer, pH 9.4: 100 ml 1 M Tris-buffer + 900 ml dH₂O.

2.12.2 Tartrate-resistant acid phosphatase (TRAP) stain

The undecalcified bone sections were stained with TRAP to investigate the activity of bone tissue associated macrophages such as osteoclasts. The deplastified sections were treated with 0.1 M sodium acetate buffer, pH 5.2 for ten minutes, followed by incubation in TRAP-stain solution containing naphthol-AS-TR-phosphate, N,N-dimethyl formamide, fast red, sodium tartrate and sodium acetate buffer using a moist chamber at 37 °C for one hour. The sections were later rinsed in three changes of distilled water for five minutes each and then counterstained with Shandon Instant-hematoxylin (6765015, Thermo Scientific, Germany) for about 20 seconds and rinsed again in distilled water for one minute. Afterwards, sections were placed under running tap water for ten minutes, rinsed in distilled water for five minutes, and then coverslipped using the Kaisers Glycerin gelatin (6474, Roth, Germany).

2.12.2.1 Preparation of reagents

- ❖ 1 M sodium acetate: 82.03 g sodium acetate (1.062680, Merck, Germany) in 1 L dH₂O. Adjust pH to 5.2 with 25 % HCl.
 - 0.1 M sodium acetate (pH 5.2): 100 ml 1 M sodium acetate + 900 ml dH₂O.
- ❖ TRAP-stain solution: Transfer substrate solution 1 into substrate solution 2. Mix thoroughly and filter before use.
 - Substrate solution 1: 35 mg of Naphthol-AS-TR-Phosphate (N6125, Sigma-Aldrich, Germany) in 125 µl of N, N-dimethyl formamide (D4551, Sigma-Aldrich).

- Substrate solution 2: 57.5 mg sodium tartrate-dihydrate (1.06663, Merck) in 1 ml of sodium acetate buffer + 35 mg fast red (368881, Sigma-Aldrich) in 1 ml of sodium acetate buffer. Mix thoroughly.
- ❖ Instant-Haematoxylin stock solution: dissolve part A and B in 1 L ddH₂O. Mix thoroughly.
 - Instant-Haematoxylin working solution: 100 ml of instant haematoxylin stock solution + 300 ml ddH₂O. Mix thoroughly and filter before use.

2.13 Immunohistochemical staining

Immunohistochemistry was performed on undecalcified bone sections using the standard Avidin-Biotin Complex (ABC) method. The indirect antigen detection method involves an unlabelled primary antibody reacting with the tissue antigen and a biotinylated secondary antibody that reacts with the primary antibody. The signal is subsequently amplified using the Vectorstain ABC HRP kit that will form a complex of avidin-biotin-peroxidase. Finally, the peroxidase enzyme complex in conjunction with the Vectorstain NovaRED peroxidase substrate forms an insoluble brown-coloured precipitate. The bone sections were stained with both the primary and secondary antibodies for BMP2, OPG, RANKL (CD254) and ASMA to determine and quantify their cellular expression levels within the fractured area. The antibodies were titrated for optimal working dilution before use. Also, the staining protocol was optimised to avoid unspecific staining.

2.13.1 Bone morphogenetic protein-2 (BMP2) stain

The undecalcified bone sections were stained with BMP2 to investigate the activity of osteoblasts. After deplastification in MEA, the samples were incubated in 100 % acetone (9372, Roth, Germany) for ten minutes, then in a solution of acetone and wash buffer (1:1) for another ten minutes, followed by washing in two changes of wash buffer for five minutes each. Subsequently, an antigen retrieval step was performed with citrate buffer solution, pH 6.0 at 60 °C for 20 minutes. The samples were cooled down to room temperature, washed in two changes of wash buffer (TBS-X) for five minutes each. The endogenous peroxidase activity was blocked with 3 % H₂O₂ (v/v) in wash buffer for ten minutes, then washed in three changes of wash buffer for five minutes each. Sections were incubated overnight at 4 °C with the rabbit polyclonal anti-human

BMP2 antibody (AP20597PU-N, Acris, Germany) diluted 1:150 with the DAKO dilution buffer (S302283, Agilent Technologies, Germany). A negative control incubated only with the dilution buffer was included. Next, samples were washed in three changes of wash buffer for five minutes each and then incubated with biotinylated goat anti-rabbit secondary antibody (BA-1000, Vector, USA) diluted 1:500 with 1 % bovine serum albumin (A3912, Sigma-Aldrich, Germany) in Tris-buffered saline (4855.2, Roth, Germany) plus 12.5 % sheep serum (S2263, Sigma-Aldrich, Germany) for 40 minutes at room temperature. The samples were washed in two changes of wash buffer for five minutes each. The signals from the target antigen were amplified using the Vectorstain Elite ABC HRP-kit (PK-6100, Vector, USA) for 30 minutes at room temperature. Then, the samples were washed twice in wash buffer and once in distilled water for five minutes each. Visualisation of the detected signals was enabled by five minutes staining with the NovaRED peroxidase substrate kit solution (SK-4800, Vector, USA). Subsequently, the samples were washed in three changes of distilled water for five minutes each. The nuclei were counterstained with Shandon instant-haematoxylin for about 20 seconds, rinsed briefly in distilled water, placed under running tap water for ten minutes, and then washed in distilled water for five minutes. Lastly, the samples were dehydrated through an ascending series of alcohol, cleared in xylene and mounted with coverslips using Depex.

2.13.2 Osteoprotegerin (OPG) and Receptor activator of NF- κ B ligand (RANKL) stain

OPG and RANKL were stained to quantify the cellular expression levels of both proteins as key regulators of osteoblastogenesis and osteoclastogenesis, respectively. The staining of the undecalcified bone sections with the OPG and RANKL primary antibodies also followed the similar procedures as described for BMP2 above. OPG was detected using a dilution of 1:300 rabbit polyclonal OPG antibody (250800, Abbotec, USA). RANKL was detected using a dilution of 1:150 rabbit polyclonal CD254 antibody (251263, Abbotec, USA). Both primary antibodies were detected using biotinylated goat anti-rabbit secondary antibody (BA-1000, Vector, USA) diluted at 1:500 with 1 % bovine serum albumin in Tris-buffered saline plus 12.5 % sheep serum.

2.13.3 Alpha-smooth muscle actin (ASMA) stain

ASMA staining was used to investigate tissue vascularisation by quantifying the positively stained blood vessels in the fractured area. The ASMA staining also followed a similar procedure as described for BMP2 above. However, no antigen retrieval step was included. The staining was carried out using a 1:400 dilution of monoclonal mouse anti-human smooth muscle actin (M0851, Agilent Technologies, Germany). The primary antibody was detected with a horse anti-mouse secondary antibody (BA-2001, Vector, USA) diluted 1:150 in 1 % bovine serum albumin in Tris-buffered saline plus 12.5 % sheep serum.

2.13.3.1 Preparation of reagents

- ❖ Citrate buffer, pH 6:
 - Solution A (100 mM citric acid): 0.2 g citric acid (3958.2, Roth, Germany) in 10 ml dH₂O.
 - Solution B (100 mM sodium citrate): 5.8 g sodium citrate (106448, Merck, Germany) in 200 ml dH₂O.
 - Working solution: Add 41 ml of solution B to 400 ml dH₂O and adjust pH to 6.0 using solution A. Bring the volume to 500 ml with dH₂O.
- ❖ Tris-sodium chloride buffer (TBS), pH 7.4: Stock solution: 60.57 g Tris-base (4855.2, Roth, Germany) + 87.66 g sodium chloride (31434, Sigma-Aldrich, Germany) in 1000 ml dH₂O. Adjust the pH to 7.4 with 25% HCl.
 - Working solution: 100 ml stock solution to 900 ml dH₂O.
- ❖ Wash buffer: 1000 ml TBS working solution + 0.025 % Triton-X. Mix thoroughly.
- ❖ Tris-buffered saline-bovine serum albumin (TBS-BSA): 1 g BSA in 100 ml of TBS.
- ❖ 3 % H₂O₂: 7 ml 30 % H₂O₂ (8.22287, Merck, Germany) + 63 ml wash buffer.
- ❖ Vectorstain Elite ABC kit solution: 1 ml TBS + 18 µl reagent A + 18 µl reagent. Prepare fresh solution 30 minutes before use.
- ❖ NovaRED peroxidase substrate kit solution: 5 ml dH₂O + 3 drops of reagent 1. Mix properly. Then add two drops of reagent 2 and mix properly. Add two drops of reagent 3 and mix properly. Lastly, add two drops of hydrogen peroxide solution and mix thoroughly. Prepare the reagent about 30 minutes before use and store in the dark.

2.14 Light microscopic imaging

Images were acquired using a Leica light microscopy system (Leica DM5500 photomicroscope equipped with a DFC7000 camera and operated by LASX software version 3.0; Leica, Wetzlar, Germany).

2.15 Bone Histomorphometric analysis

Histomorphometric analysis was performed on the overview images generated from the Leica microscope using Adobe Photoshop (version CS6, Adobe, Germany). After loading each image, the system was calibrated according to the objective size. The ROI was defined and manually contoured in the fractured area of the operated left femur and at a comparable region in the unoperated right femur. Then, the positively stained area was selected and measured in a semi-automated manner, and the value was given in square millimetre. The generated values were then used to determine, for instance, the percentage of osteoid and mineralised bone areas of the operated femur relative to the unoperated femur. Similarly, the histomorphometric assessment was also performed on the TRAP, ALP, OPG, BMP2 and RANKL stained samples. Manual counting of the blood vessels and osteocytes lacunae was performed for the ASMA and silver nitrate staining, respectively.

2.16 Gene Expression analysis

2.16.1 RNA isolation

The freshly frozen bone slices stored in RNAlater solution at -80 °C were thawed at room temperature. The newly formed trabecular bone within the fractured area of the operated femur was carefully selected. For comparison, the trabecular bone was also collected from the metaphyseal area of the unoperated contralateral side. Subsequently, about 50 mg was collected from each sample with the aid of forceps for RNA isolation using the Lipid Tissue Mini Kit (160021969, Qiagen, Germany) according to the manufacturer's protocol. The isolated RNA was quantified using NanoDrop™ 1000 Spectrophotometer (NanoDrop Technologies, USA). After DNase treatment to remove genomic DNA, 0.5 µg RNA from each sample was reserved transcribed to cDNA using the QuantiTect Reverse Transcription Kit (157036867,

Qiagen, Germany) as described by the manufacturer. The samples were stored at -20 °C.

2.16.2 Primer testing and validation for the target genes

The primers for BMP2, OPG and RANKL were designed, tested and validated before being used for gene expression analysis. The remaining primers, namely osteocalcin (BGLAP), collagen type-1 alpha-1 (COL1A1), collagen type-2 alpha-1 (COL2A1), cathepsin-K (CTSK) and ALP were directly used for analysis since they were already established in the laboratory. The forward and the reverse sequences of the primers and the amplicon length are shown in table 5.

Table 5: The forward and reverse primer sequence of the target genes.

Gene	Forward Sequence (5' 3')	Reverse Sequence (5' 3')	Amplicon length (bp)
BGLAP	CAGCGAGGTGGTGAAGAGAC	GTCATCACAGTCAGGGTTG	122
CTSK	GGGTCAATGTGGTTCCTGTT	GCAGCCATCATTCTCAGACA	133
COL1A1	CCAGTCACCTGCGTACAGAACG	GCCAGTGTCTCCTTTGGGTCC	246
ALP	TCAGCAGACCCTGAAAAATG	TTCTTAGCCACGTTGGTGTTG	60
BMP2	GAAAGGACACCCTCTCCACAG	GCAACGATCCAGTCATTCCAC	135
OPG	AAACAGCGACACAACACTCACG	TGTCCAATATGCCTCCTCACG	140
RANKL	CTGTGCAGAAGGAAATGCAAC	GCGTTAATCGTGAGATGGGC	139
COL2A1	ACCCAGAACCAACACAATCC	TCAGTGCAGAGTCCTAGAGTG	81
B2M	CCAGAAGATGGAAAGCCAAA	AGCGTGGGACAGAAGGTAGA	159

2.16.3 Quantitative PCR

Quantitative PCR analysis of BMP2, OPG, RANKL, ALP, BGLAP, COL1A1, COL2A1, CTSK and the reference gene B2M were performed with the Quantifast SYBR Green PCR Mastermix kit (151050429, Qiagen, Germany) on the LightCycler® 2.0 instrument (software version 4.1, Roche, Germany). Each capillary tube contained 2 µl sample cDNA, 5 µl Quantifast SYBR Green PCR Mastermix, 0.2 µl (20 µM) of the primer and RNase free water to bring it to a final volume of 10 µl. The sample mixture was centrifuged for about one minute before thermal cycling. The thermal cycling program comprised of one denaturation cycle at 95 °C for five minutes, followed by 40 PCR cycles at 95 °C for ten seconds and 60 °C for 30 seconds. The specificity of the amplicon was verified using melting curve formation under one cycle at 95 °C, down to 60 °C for 15 seconds and back to 95 °C. The last cycle was a cooling step at 40 °C for 30 seconds. All analysis was performed in duplicate. Two negative controls, that is, a

mixture without transcriptase (RT-) and water instead of cDNA were included in each run. A sample with a known C_T value served as the positive control.

2.16.4 Data analysis

The mean values from the duplicate run were determined and normalised to the reference gene. Afterwards, the relative expression of the target genes of the operated left femurs was compared to those of the unoperated right femurs using the $2^{-\Delta C_T}$ method [54].

$$\text{Relative expression} = 2^{-\Delta C_T}$$

$$\Delta C_T (\text{operated left femur}) = (C_{T, \text{target gene left femur}} - C_{T, \text{B2M left femur}})$$

$$\Delta C_T (\text{unoperated right femur}) = (C_{T, \text{target gene right femur}} - C_{T, \text{B2M right femur}})$$

2.17 Time-of-Flight Secondary Ion Mass Spectrometry (ToF-SIM) analysis

The local distribution of calcium and collagen within the fractured area was studied using the ToF-SIMS 5-100 machine (ION-TOF Company, Germany) equipped with a 25 keV Bi-cluster ion source for surface examination. This analysis was performed by Dr. A. Henss, a collaborating partner at the Institute of Physical Chemistry, University of Giessen. The analysis was performed on undecalcified bone sample grinding of approximately 70 μm thickness. The ToF-SIMS method has been previously described [55]. Briefly, a primary ion gun using Bi_3^+ as main ion species was operated in the high current bunched (hc-bu) mode with highest mass resolution and a lateral resolution of about 10 μm . The signals collected from $\text{C}_4\text{H}_8\text{N}^+$, a proline derivative, which is one of the main components of collagen was used to image the collagen distribution [56]. The Ca^+ signal represented the mineralised bone area. To obtain a good mass image of the bone slice, a complete stage scan with a pixel density of 100 per mm, a cycle time of 60 μs , five frames per patch and three scans were generated. Single images with sizes of 400 x 400 μm^2 were stitched together to obtain areas of several square millimetres. Data evaluation was done with the Surface Lab 6.7 software of IONTOF Company.

2.18 Embedding of bone slices in Epon

The newly formed trabecular bone samples harvested from the fractured area were embedding in Epon to enable ultrastructure analysis as described below:

- ❖ Fixation: yellow fix buffer overnight at 4-8 °C.
- ❖ 6x washing using 0.1 M Cacodylate buffer at 4-8 °C with rigorous shaken.
- ❖ 3x washing using 0.1 M Cacodylate buffer at 4-8 °C with rigorous shaken.
- ❖ Store at 4 °C overnight in 0.1 M Cacodylate buffer.
- ❖ 3x washing using 0.1 M Cacodylate buffer at 4-8 °C with rigorous shaken. The washing step was continued until the yellow colour faded away.
- ❖ The samples were transferred into a dark staining rack.
- ❖ The samples were fixed once more in 1 % osmium tetroxide for two hours at room temperature.
- ❖ 6x washing using 0.1 M Cacodylate buffer at 4-8 °C with rigorous shaken. At least five minutes per wash.

The samples were dehydrated in increasing concentration of ethanol and xylene as shown in table 6.

Table 6: Sample embedding in Epon.

Duration of the dehydration, infiltration, embedding and polymerisation steps.

Treatment phase: Dehydration, infiltration and embedding		
Dehydration in Ethanol		
Concentration	Duration	Temperature
30 %	10 minutes	RT
50 %	2x 10 minutes	RT
70 %	2x 10 minutes	RT
80 %	2x 10 minutes	RT
96 %	2x 10 minutes	RT
100 %	15 minutes	RT
100 %	3x 30 minutes	RT
100 %	45 minutes	RT
Intermedium in Xylene		
Concentration	Duration	Temperature
100 %	3x 15 minutes	RT
Resin embedding (Epon mix)		
Reagent	Duration	Temperature
Infiltration 1	2 hours	Desiccator, 600mbar
Infiltration 2	Overnight	Desiccator, 600 mbar
Infiltration 3	4 hours	Desiccator, 600 mbar
Infiltration 4	Overnight	Desiccator, 600 mbar

Infiltration 5	10 minutes	60 °C incubator	
	50 minutes	Desiccator, 600 mbar	
	10 minutes	60 °C incubator	
	50 minutes	Desiccator, 600 mbar	
	10 minutes	60 °C incubator	
	50 minutes	Desiccator, 600 mbar	
	10 minutes	60 °C incubator	
	50 minutes	Desiccator, 600 mbar	
	Embedding	10 minutes	60 °C incubator
	Embedding	15 minutes	Desiccator, 600 mbar
Polymerisation I	3 hours	48 °C	
Polymerisation II	20 hours	60 °C	

Key: mbar: millibar; °C: degree Celsius; RT: room temperature

2.18.1 Preparation of reagents

- ❖ Yellow fixation buffer (stock solution): 2 % paraformaldehyde (0335, Roth, Germany) in 500 ml dH₂O + 500 ml sodium phosphate buffer solution (pH 7.2-7.4) + 0.02 % picric acid (74069, Sigma-Aldrich, Germany).
 - Working solution: 32 ml of 25 %-glutaraldehyde (3778, Roth, Germany) + 268 ml of the yellow fixation buffer stock solution.
- ❖ 0.2 M Cacodylate buffer: 42.8 g Sodium cacodylate trihydrate (5169, Roth, Germany) in 1 L of ddH₂O. The pH was adjusted with 0.2 N HCl to 7.2.
 - Working solution (0.1 M): Mix 1 part of 0.2 M cacodylate buffer + 1 part of dH₂O.
- ❖ 2 % Osmium tetroxide (OSO₄): 1 g OSO₄ (8371, Roth Germany) + 50 ml ddH₂O.
- ❖ Epon stock solution: 95 ml Glycid ether (21045, Serva, Germany) + 40 ml 2-Dodecenylsuccinic acid anhydride (20755, Serva, Germany) + 62 ml Methylnadic anhydride (29452, Serva, Germany).
 - Epon working solution was prepared by mixing the 197 ml stock solution + 3 ml 1.5 % 2,4,6-Tris(dimethylaminomethyl)phenol (20755, Serva, Germany).
- ❖ Infiltration 1: 10 ml Xylene + 5 ml Epon working solution.
- ❖ Infiltration 2: 5 ml Xylene + 5 ml Epon working solution.
- ❖ Infiltration 3: 5 ml Xylene + 10 ml Epon working solution.
- ❖ Infiltration 4: 15 ml Epon working solution.
- ❖ Infiltration 5: 15 ml Epon working solution.

- ❖ **Embedding:** Samples were embedded in Epon working solution. The final volume was dependent on the size of the embedding form. The samples were placed longitudinally on the narrow part of the form with the number tags.

2.19 Ultramicrotomy

2.19.1 Semi-thin sections

Semi-thin sections of about 0.5 µm thickness were prepared from the Epon-embedded samples using a histo-knife (DH4580 Diatome, Switzerland) on the ultramicrotome machine (701 701, Reichert-Jung, Germany). Each section was transferred onto a superfrost plus glass slide (03-0060, Langenbrinck, Germany) with the aid of a perfect loop (Diatome, Switzerland) and the sections were dried on a hot plate at 70 °C. The sections were stained for 15 seconds in Toluidine blue solution containing 1.25 % Toluidine blue (1B-481, Chroma Germany) + 1 % Borax (1.06306, Merck, Germany) diluted in double distilled water and then for five seconds in Safranin-O solution consisting of 1 % Safranin (1.15948, Merck, Germany) + 1 % Borax diluted in double distilled water, while being placed on a hot plate. Dried sections were coverslipped using a small drop of warm Epon solution and then polymerised at room temperature for two days. The samples were examined under the light microscope to localise the ROI. Overview images were taken, and the ROIs were identified and marked to enable further sample trimming and generation of the ultrathin sections.

2.19.2 Ultrathin sections

After proper sample trimming and cutting, ultrathin sections between 60 - 80 nm thicknesses were cut from the ROIs with the aid of a 35°-diamond knife (DU3525, Diatome, Switzerland) and an ultra-microtome machine (701 701, Reichert-Jung, Germany). Sections were carefully transferred onto 200 mesh copper grids (G2200C, Plano, Germany) that have been previously filmed with 2 % Collodion (12620-10, EMS, USA). To enable similar and reproducible contrasting, all samples were contrasted with 0.5 % uranyl acetate (Ultrastain 1, Laurylab, France) for 30 minutes and 3 % lead citrate (Ultrastain 2, Leica, Germany) for 80 seconds using the Leica contrasting machine (Leica EM AC20, Germany) in accordance with the manufacturer's protocol. Afterwards, the grids were dried, and the samples were stored using a grid box.

2.20 Transmission electron microscopic imaging

Images were acquired using a Zeiss transmission electron microscopy system (Zeiss EM912 OMEGA, Germany), equipped with a camera (TRS Sharp Eye 2k slow-scan CCD, Tröndle, Moorenweis) and controlled by the Olympus iTEM software. During imaging, the camera was cooled at -5 °C by the iTEM software.

2.21 Statistical analysis

The data analysis and graphical presentations were done using GraphPad Prism 8.0 (GraphPad Software Inc, USA) and SPSS (V.22.0, SPSS Inc, USA). All results are presented as means \pm standard error of the mean. The mean values from the operated left femur were compared to those of the unoperated right femur using the Wilcoxon matched-pairs signed rank test or paired Student's t-test to determine if a significant difference exists between the two groups and *p*-values less than 0.05 were considered significant.

3. RESULTS

3.1 Clinical observations

All the six animals tolerated the 10 mm osteotomy gap created at the distal metaphyseal area of the left femur. The animals returned to their normal activity and full load bearing around day three post-surgery. Postoperative X-ray of the femur revealed the fracture gap at the distal femur metaphysis with correct placement of the plate and locking screws that extended into the epiphysis for better stability of the fracture (Fig. 7A-B). All the sheep survived the observation period without any plate breakage, fracture or other relevant adverse events and could be euthanised according to the study protocol.

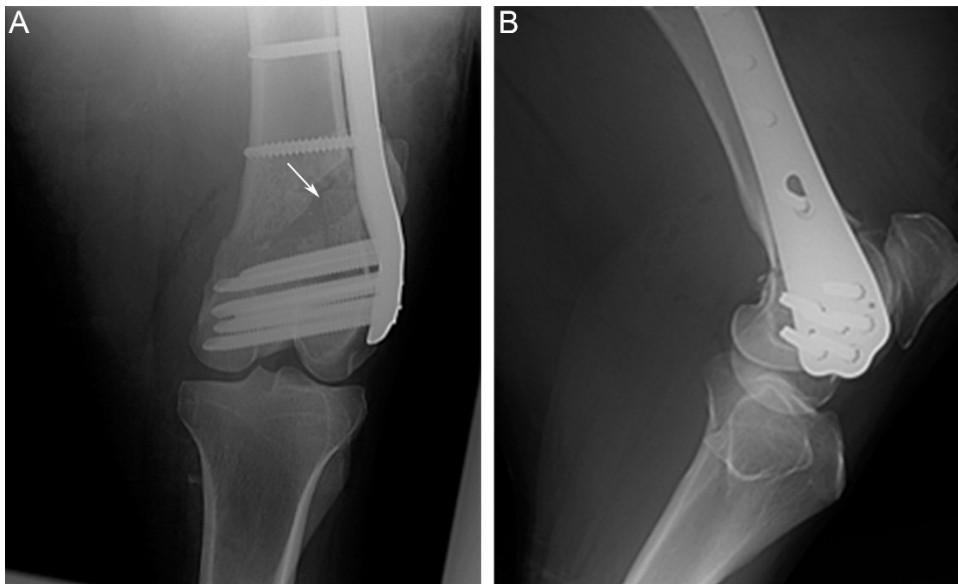


Fig. 7. Postoperative X-ray analysis of the operated femur. (A) The postoperative X-ray image on day 1 revealed the wedge-shaped metaphyseal fracture in the frontal plane on the antero-posterior view (arrow) with the locking plate and screws. (B) The lateral view showed the proper alignment of the plate along the femur axis. The osteotomy is not visible on the lateral image due to the overlying plate.

3.2 Bone mineral density evaluation

The whole-body BMD of each animal was measured immediately before the fracture and at 12 weeks post-fracture to determine whether the BMD of the animals were comparable before and after the surgery. The measurement revealed similar BMD in the study animals (Fig. 8A). The average BMD value at three months was slightly reduced at both the operated left and unoperated right femurs, but with no significant difference (Fig. 8B).

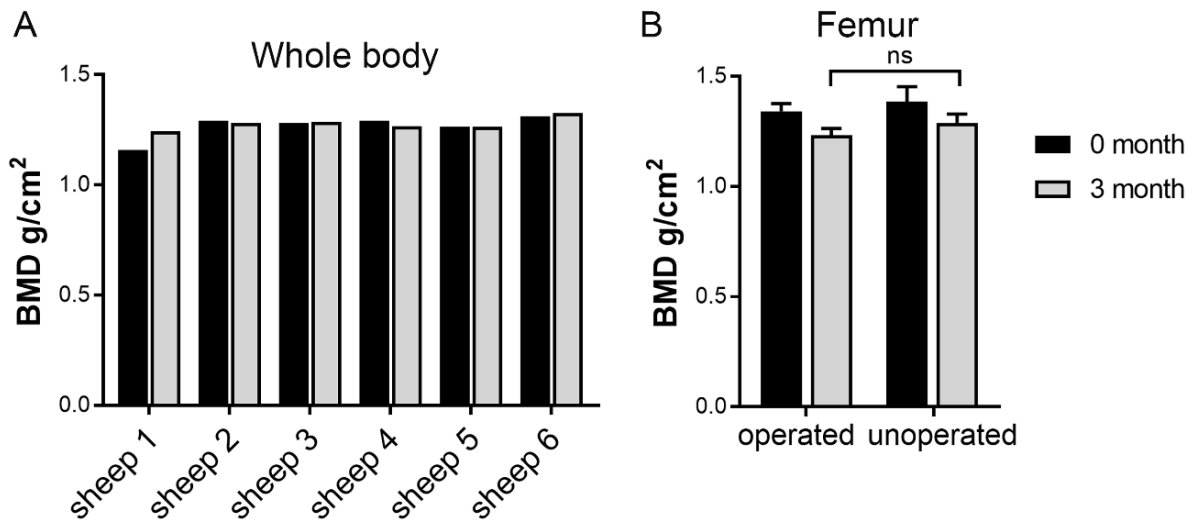


Fig. 8. Evaluation of the BMD. (A) The BMD at the whole-body region of the individual animal before and three months after femur osteotomy (B) Average BMD values on the operated left and unoperated right femurs. ns = not significant.

3.3 Micro-computed tomography analysis

3.3.1 Substantial bony bridging of the fracture gap evident by the high healing scores

Next, the healing quality at the fractured area was determined by a macroscopic analysis of the reconstructed 3D micro-CT images of the bone slices. Qualitatively, images of all samples revealed a complete bridging of the fracture gap from the medial side up to two-thirds of the fractured area. Four of the six samples (Fig. 9A-D) achieved almost complete healing of the entire fracture gap from the medial to the lateral cortex whereas the remaining two samples attained partial healing (Fig. 9E-F). Blinded scoring of the degree of healing by two independent investigators showed scores ranging between 4 and 8.5 from a maximal score of 9 (Fig. 10). The newly formed bone present in the fractured area appeared very dense and quite like the native bone outside the fractured area.

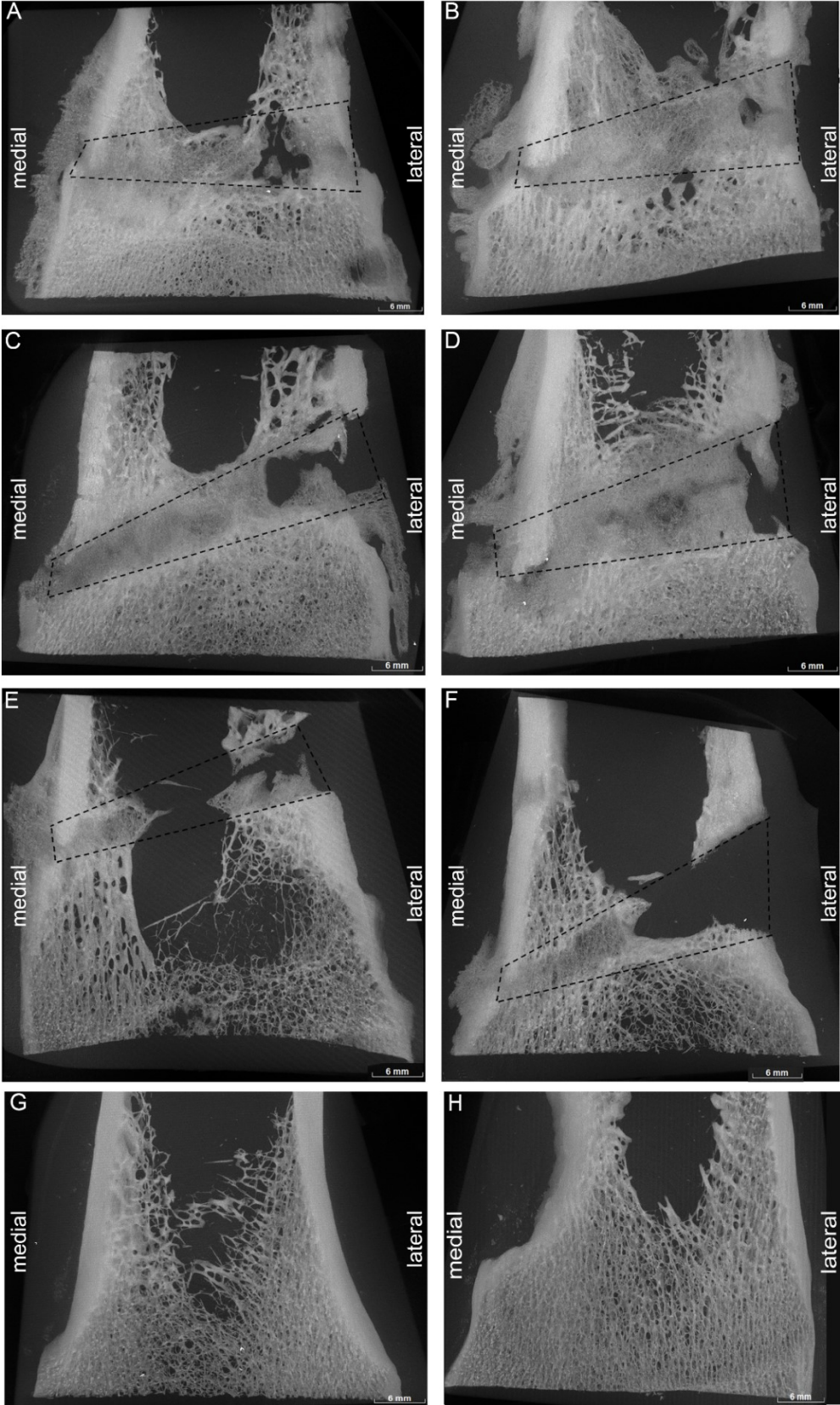


Fig. 9. Micro-CT image evaluation of the healing status of all six sheep at 12 weeks post-fracture. (A-D) Four of the six sheep, namely sheep number 2 (A), 3 (B), 5 (C) and 6 (D), showed almost complete bone bridging of the entire fractured area. (E-F) Partial healing of the fracture was evident in sheep 1 (E) and 4 (F). The fracture bridged fully from the medial aspect but very minor from the lateral side. The wedge-shaped outline shows the fractured area. (G-H) Two representative images of bone slices from the unoperated right femur showing the intact metaphyseal bone area.

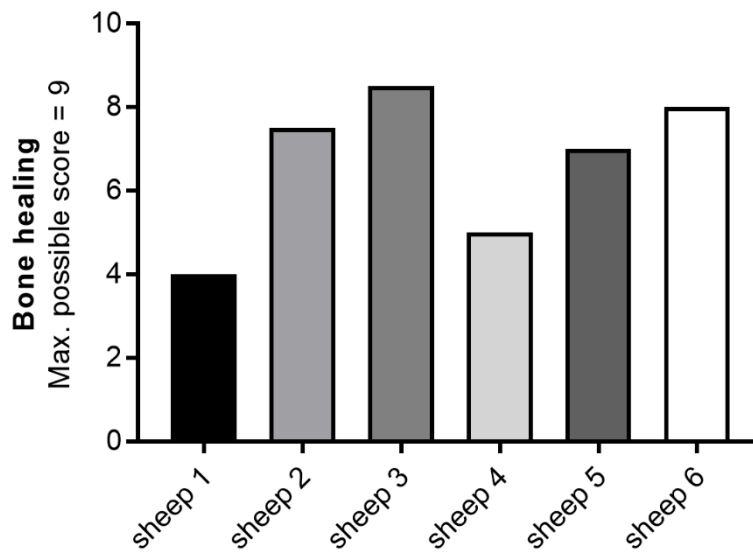


Fig. 10. Qualitative evaluation of the degree of bone healing. Healing score was determined from the macroscopic assessment of the fractured area from medial to the lateral end of the cortex.

3.3.2 An increased amount of newly formed bone revealed by the quantitative 3D-morphometry

Direct 3D-quantitative morphometry of a defined ROI within the trabecular bone area of the operated femur and a corresponding region within the unoperated femur showed that the bone volume (BV) and the ratio of the bone volume to total volume (BV/TV) were comparable in both femurs (Fig. 11A-B). Also, the number of trabeculae within the healed operated femur was comparable to the unoperated side (Fig. 11C). However, the thickness and spacing of the trabeculae were significantly higher in the operated femur when compared to the unoperated femur (Fig. 11D-E). Furthermore, the structural model index (SMI), a parameter for estimating the shape the trabecular was significantly reduced in the operated femur (Fig. 11F).

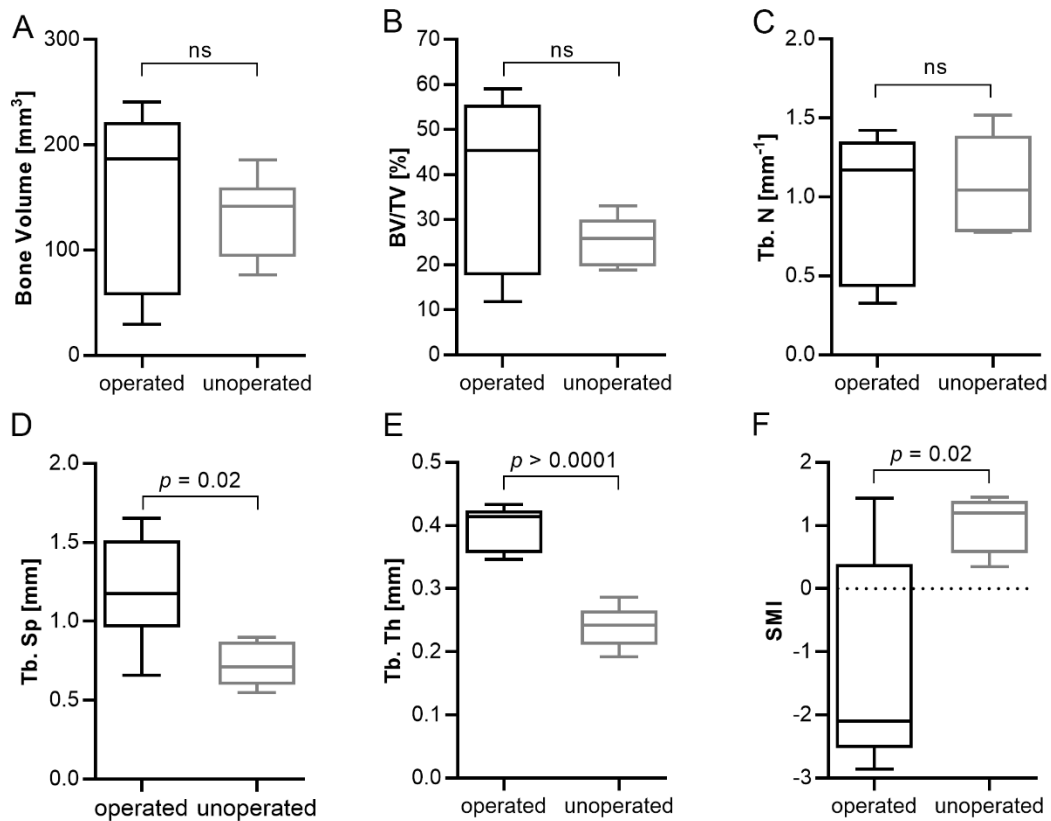


Fig. 11. Quantitative micro-CT image analysis. A direct 3D quantitative morphometry of a defined ROI within the trabeculae of the operated femur and the unoperated contralateral femur showing positive structural changes of the new trabeculae as revealed by a higher (A) bone volume (B) bone volume / total volume (BV/TV) and (C) comparable number of trabeculae (Tb.N). (D-E) A significantly higher trabecular spacing (Tb.Sp) and thickness (Tb.Th). (F) A negative structural mass index (SMI) value. ns = not significant.

3.4 Biomechanical analysis

3.4.1 A comparable bone stiffness at both the operated and unoperated femurs

The indentation test on nine different points covering the trabecular and cortical regions within the fractured area and sub-regions was performed on the bone slices to compare the stiffness of the fractured bone to those of the unoperated contralateral femur. The data generated by the cooperation partner as mentioned in the method section was used for the quantitative analysis. The quantification of the bone biomechanical strength based on the degree of stiffness showed that the operated femur both at the cortical and trabecular areas was not statistically different from the intact contralateral side as shown in figure 12. Furthermore, the stiffness at both the cortical area of the operated and unoperated femurs was two-fold more than in the trabecular area.

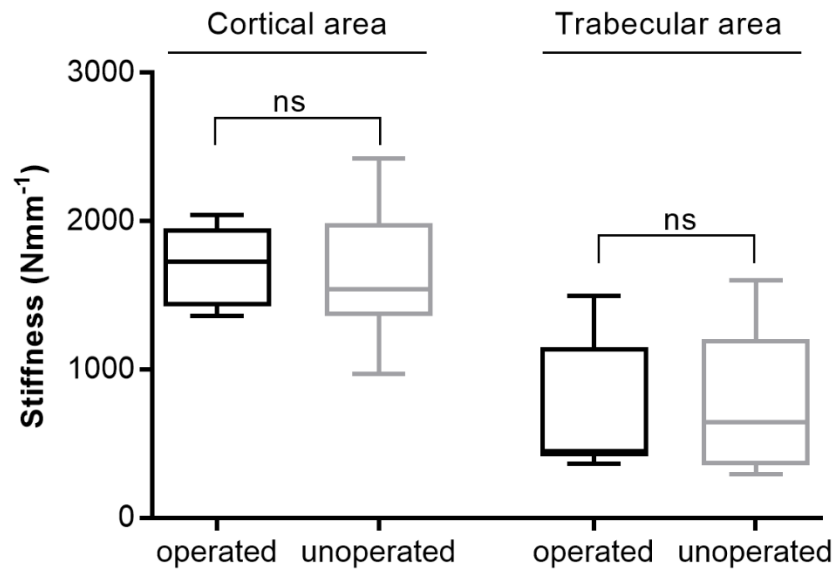


Fig. 12. Assessment of the biomechanical competence of the newly formed bone. The bone stiffness at the cortical and trabecular areas of the operated and unoperated femurs. The bone stiffness of the operated left femur was not statistically different from the unoperated right femur. However, the stiffness was about two-fold higher in the cortical area of both groups. ns = not significant.

3.5 Qualitative and quantitative histology

The overall microstructural appearance of the newly formed bone and the differentiation of mineralised from osteoid tissue were determined by trichrome Masson-Goldner and von-Kossa van-Gieson stain, respectively. Furthermore, the quantity and morphological arrangement of the osteocytes-lacunae canaliculi network was determined through silver nitrate stain.

3.5.1 Healing characterised by a dense inter-cortical and trabecular bone bridging

The overall microstructural appearance of the newly formed bone was determined by trichrome Masson-Goldner stain. An advanced bony bridging that correlated with the micro-CT images was evident. Medially, there was both inter-cortical and trabecular bone bridging of the fractured area as shown in the representative overview image (Fig. 13A). The fractured area was almost entirely bridged with new bone. Only a minor area within the trabeculae was bridged with soft connective tissue, mostly in the form of dense collagenous fibres. The bridged cortical bone area revealed tightly packed osteons of concentric lamellae while the connective tissue area showed dense collagenous fibres (Fig. 13B-C). The newly formed trabecular bone revealed dense and well-structured trabeculae and marrow space enriched with adipose tissue, similar to the native bone lying outside the fractured area (Fig. 13D). Moreover, chondrocytes were absent in the fractured area. The new trabeculae healed through a direct

membranous bone formation at the marrow cavity without any visible callus. However, a thin layer of periosteal callus was visible only at the medial end of the femoral cortex whereas at the lateral cortex no external callus formation was visible.

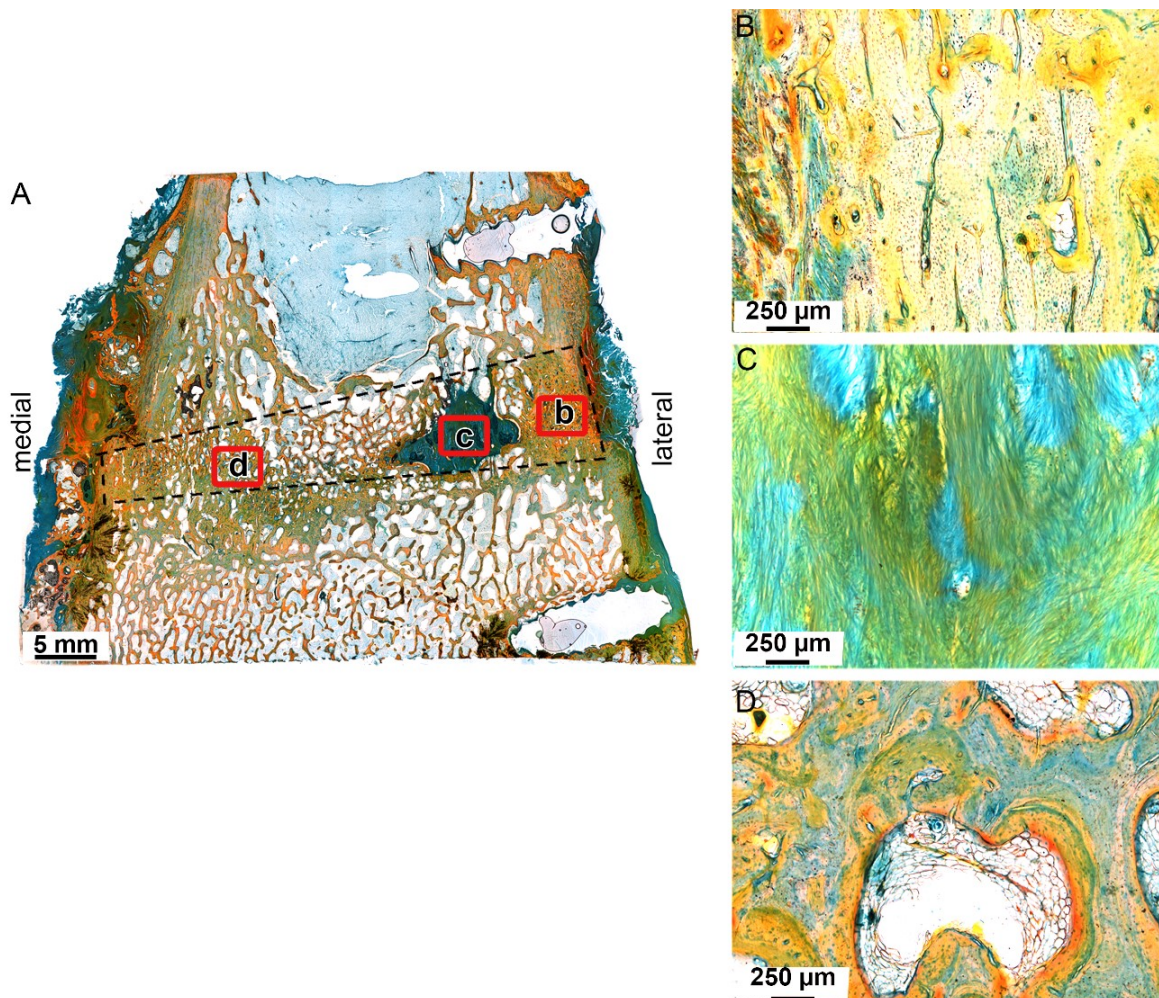


Fig. 13. Microstructural features of the newly formed cortical and trabecular bone in the fractured area. (A) Overview image of a coronal ground bone section of sheep number 2 stained with trichrome Masson-Goldner showing an advanced bony bridging at the fracture gap. The gap was almost entirely replaced with new bone. No callus formation is evident at the lateral cortex whereas a thin layer of periosteal callus is visible at the end of the medial cortex. A minor area within the trabeculae is filled with soft connective tissue, marked C. Detail images of the (B) cortical bone area showed a compact mineralised cortex with the typical Haversian system, (C) connective tissue showed bundles of dense collagenous fibres, and (D) trabecular bone area revealing dense and well-structured mineralised trabeculae with marrow cavity lying within. The mineralised bone area was stained greenish-orange, and the unmineralised bone area was stained green.

3.5.2 Major matrix mineralisation as evident by an increased amount of mineralised bone area

The level of mineralisation of the newly deposited bone matrix was determined by the von-Kossa van-Gieson stain. The images revealed a large area of mineralised bone (black staining) and less of the osteoid area (pink staining) within the fractured area of the operated left femur that was similar to that of the unoperated right femur (Fig. 14A-B). The osteoid region surrounded the mineralised area and was majorly composed of dense collagenous fibres with numerous osteoblasts embedded within (Fig. 14C-D). The histomorphometric analysis of a defined ROI revealed an average of about 40 % mineralised bone area in the operated femur that was comparable to the unoperated femur (Fig. 14E). However, the percentage of the osteoid area in the fractured area was significantly higher than the intact unoperated femur (Fig. 14F).

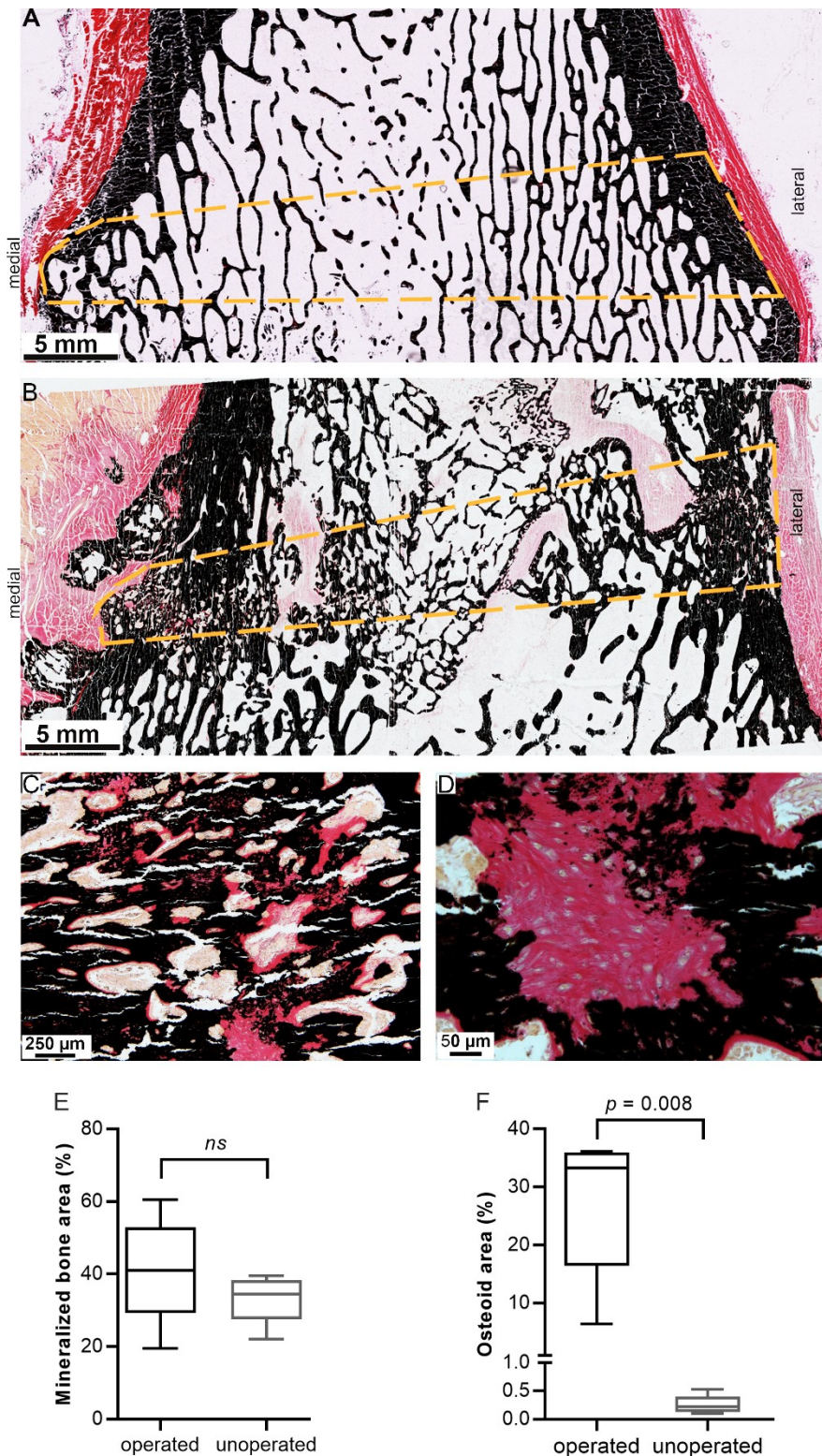


Fig. 14. Major bone matrix mineralisation as evidence of advanced bone healing. Overview image of undecalcified bone sections of the (A) unoperated right and (B) operated left femurs stained with von-Kossa van-Gieson showing the mineralised area in black and the osteoid area in pink. Close-up images of B within the fractured area (yellow dashed-line sketch) revealed mainly mineralised bone area (C) and the minor osteoid area (D) showed collagenous fibres that surrounded and lined the surface of the mineralised bone with numerous osteoblasts embedded within. (E) A higher percentage of the mineralised bone area was evident; however, the quantity was not statistically different from the unoperated femur. (F) The percentage of the osteoid area of the operated femur was significantly higher relative to the unoperated femur. The dashed-line sketch shows the ROI area used for the histomorphometric analysis. ns= not significant.

3.5.3 Increased number of regularly organised osteocytes-lacunae canaliculi network

The quality of the healing outcome in the fractured area was further characterised by quantifying the osteocytes lacunae and the morphological arrangement of the osteocyte-lacuna canaliculi network. Images of decalcified bone sections stained with silver nitrate revealed mostly spherically shaped osteocytes lacunae organised in lamellae and interconnected via the canaliculi network that was similar to the unoperated contralateral side (Fig. 15A-C). The canaliculi network was mostly arranged perpendicular to the longitudinal axis of the trabeculae. There was an increased number of osteocytes lacunae in the fractured area. However, the amount was significantly higher in the unoperated femur (Fig. 15D). Empty lacuna was mostly found at the lateral cortex where the least bone bridging occurred.

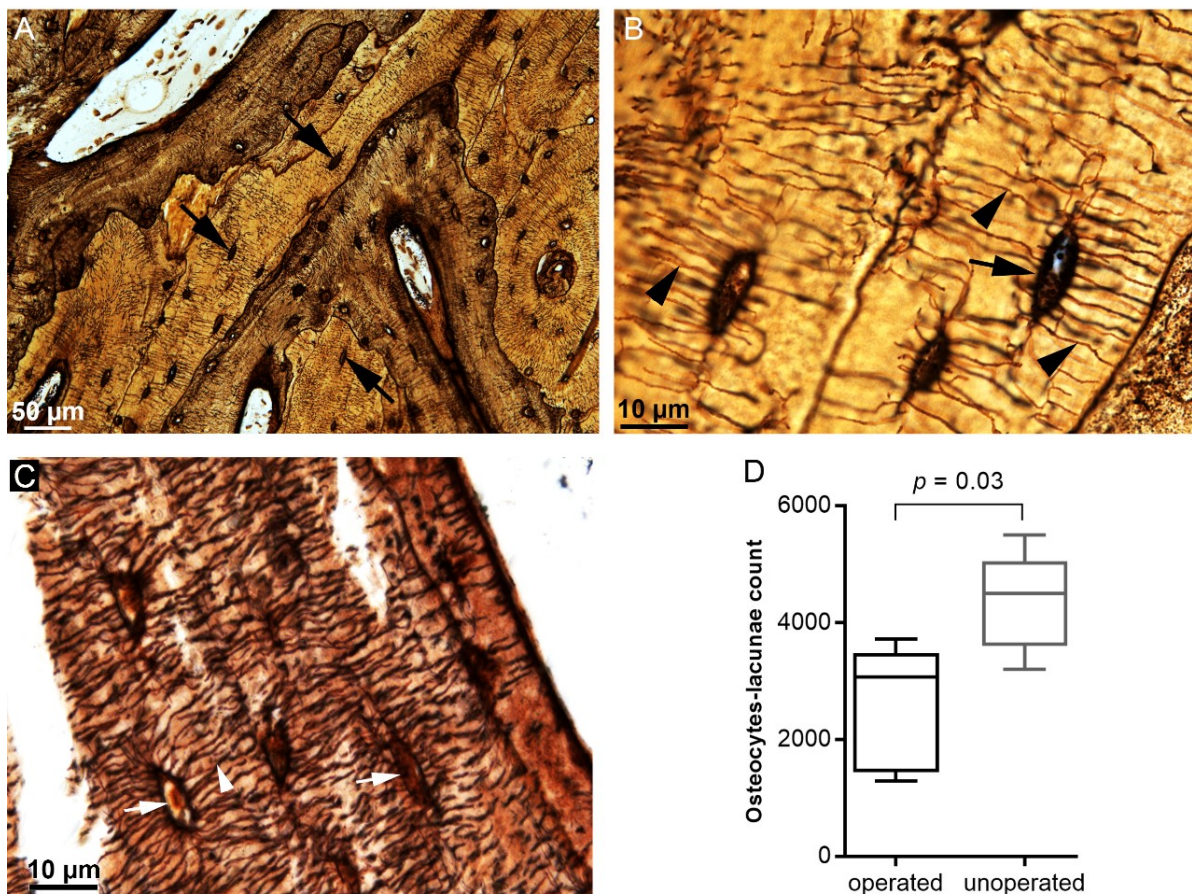


Fig. 15. Increased number of well-organised spherically shaped osteocytes-lacunae with the canaliculi network as proof of the new bone maturation. Images of decalcified silver nitrate stained bone sections of (A-B) operated and (C) unoperated femur showing abundant spherically shaped osteocytes (arrows) that were regularly arranged within the trabecular bone area. The close-up images (B-C) revealed the osteocyte-lacuna canaliculi network. The canaliculi networks in both operated and unoperated femur were arranged perpendicular to the bone surface (arrowheads). (D) The amount of the osteocytes lacunae was significantly higher in the unoperated femur.

3.6 Qualitative and quantitative enzyme histochemistry

3.6.1 A significantly higher cellular expression of ALP in the operated femur

The cellular activity of ALP as a key osteoblast marker associated with bone matrix mineralisation and TRAP as an osteoclast marker involved in bone resorption was determined by enzyme histochemical staining of the bone sections. The staining revealed high expression of ALP-positive cells and reduced expression of TRAP-positive cells in the fractured area (Fig. 16A-D). Similarly, histomorphometric analysis depicted significantly higher ALP activity in the operated relative to the unoperated femur (Fig. 16E). Although there was a lower activity of TRAP compared to ALP in the fractured area, the amount of TRAP positive cells in the operated femur was significantly higher than in the unoperated femur that expressed a negligible quantity (Fig. 16F).

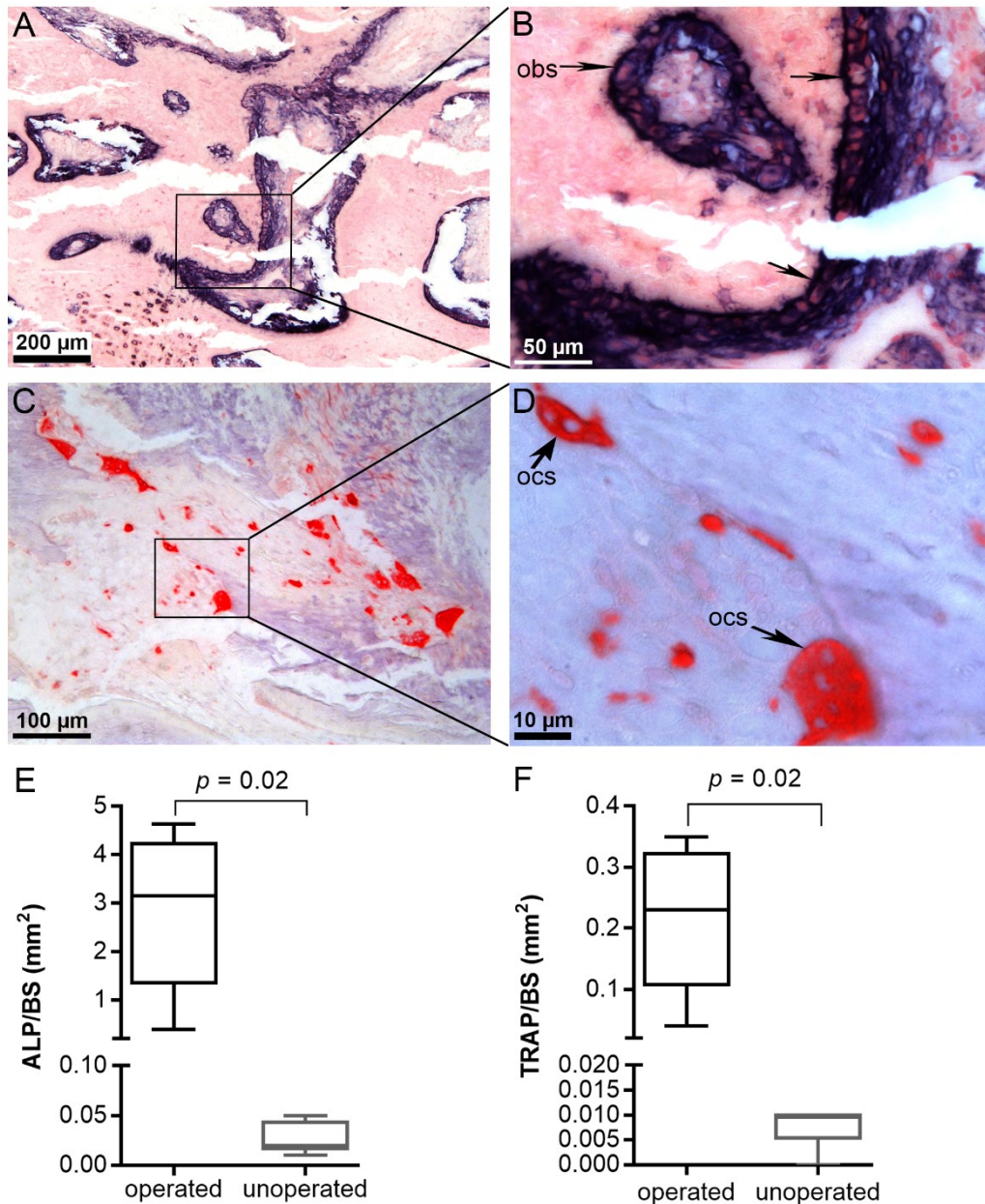


Fig. 16. Bone formation in the fractured area evident in the significantly higher activity of the osteoblasts. Photomicrographs of the ALP stained bone sections of the operated femur showing (A) increased activity of the osteoblasts. (B) Close-up image of A showing densely stained osteoblasts (obs) lining the bone surface (C) The reduced TRAP-positive cells visualised in the operated femur indicated lower osteoclasts activity (D) Close-up image of C revealing few multinucleated osteoclasts (ocs) attached to the bone surface. Histomorphometric analysis showed significantly higher activities of (E) ALP and (F) TRAP in the operated in comparison to the unoperated femur.

3.7 Qualitative and quantitative immunohistochemistry

3.7.1 A moderate amount of BMP2, OPG, RANKL and a reduced ASMA count

By employing the immunohistochemical technique that involves primary antibody binding to a specific antigen, bone sections were stained with the following antibodies; BMP2, OPG, RANKL and ASMA to determine their cellular expression level within the fractured area. Both BMP2 and OPG (bone formation markers) and RANKL (bone

resorption marker) were positively expressed (Fig. 17A-C). Histomorphometric analysis of the defined ROI (Fig. 17E) revealed similar quantities of the tested bone formation and resorption markers (BMP2, OPG and RANKL). The positively stained alpha smooth muscle cells localised within the vascular walls (Fig. 17D) confirmed the presence of blood vessels in the fractured area. The blood vessels were typically small-sized and sparsely distributed. The low ASMA count in the operated femur was comparable to the unoperated contralateral femur (Fig. 17F).

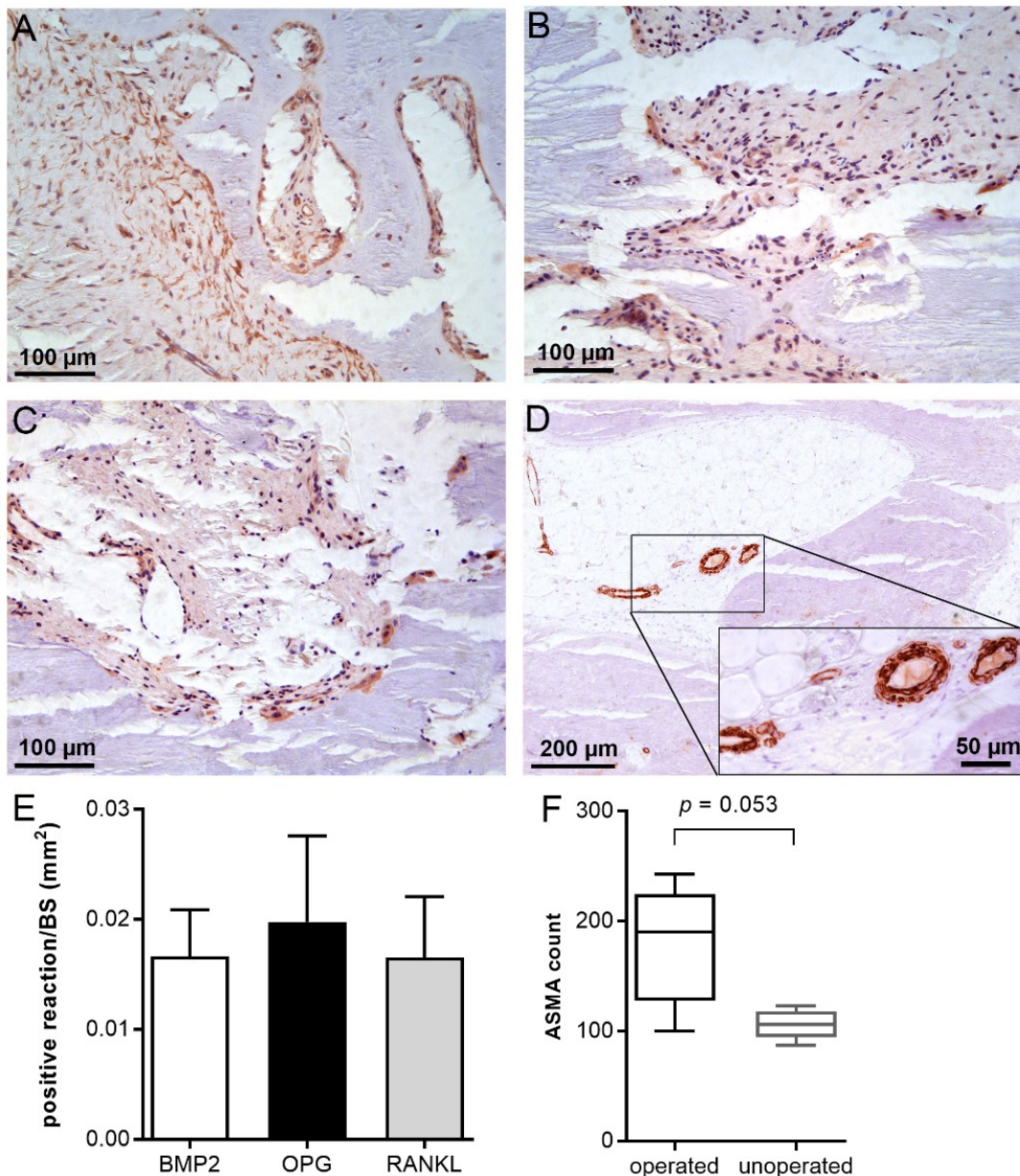


Fig. 17. Comparative expression of BMP2, OPG, RANKL and ASMA. Photomicrographs of the bone sections revealed a brownish stained (A) BMP2 and (B) OPG area, indicating new bone formation. (C) RANKL positive area reflected osteoclast associated bone resorption. (D) ASMA positive area revealed small-sized blood vessels with thin lumen lying within the trabecular bone marrow as shown in the close-up image. (E) The reduced amounts of BMP2 and OPG corresponded with that of the bone resorption marker, RANKL in the operated femur. (D) The ASMA count of the operated was almost significantly higher than in the unoperated femur.

3.8 Gene expression analysis

3.8.1 Up-regulation of prominent genes involved in bone formation

The gene expression of prominent bone formation and resorption markers in the fractured area was quantified using quantitative PCR. Most of the tested genes were expressed higher in the operated femur. However, the quantity was not statistically different from the unoperated contralateral femur as shown in figure 18. The bone turnover markers including, COL1A1, a dominant extracellular matrix collagenous protein alongside BGLAP and ALP, which are important osteoblast markers known to support bone matrix mineralisation were expressed at higher amount compared to OPG and BMP2.

Further, COL2A1 a cartilaginous tissue marker was expressed in a negligible quantity in both the operated and unoperated femur (Fig. 15A-F). The reduced expression of the OPG gene correlated positively with that of its agonist, RANKL that was also expressed in similar quantity resulting in equal RANKL/OPG ratio (Fig 15G-H). Surprisingly, CTSK, an important bone resorption marker was expressed more in the operated femur in contrast to the unoperated right femur (Fig 15I). However, there was no statistical difference between both groups.

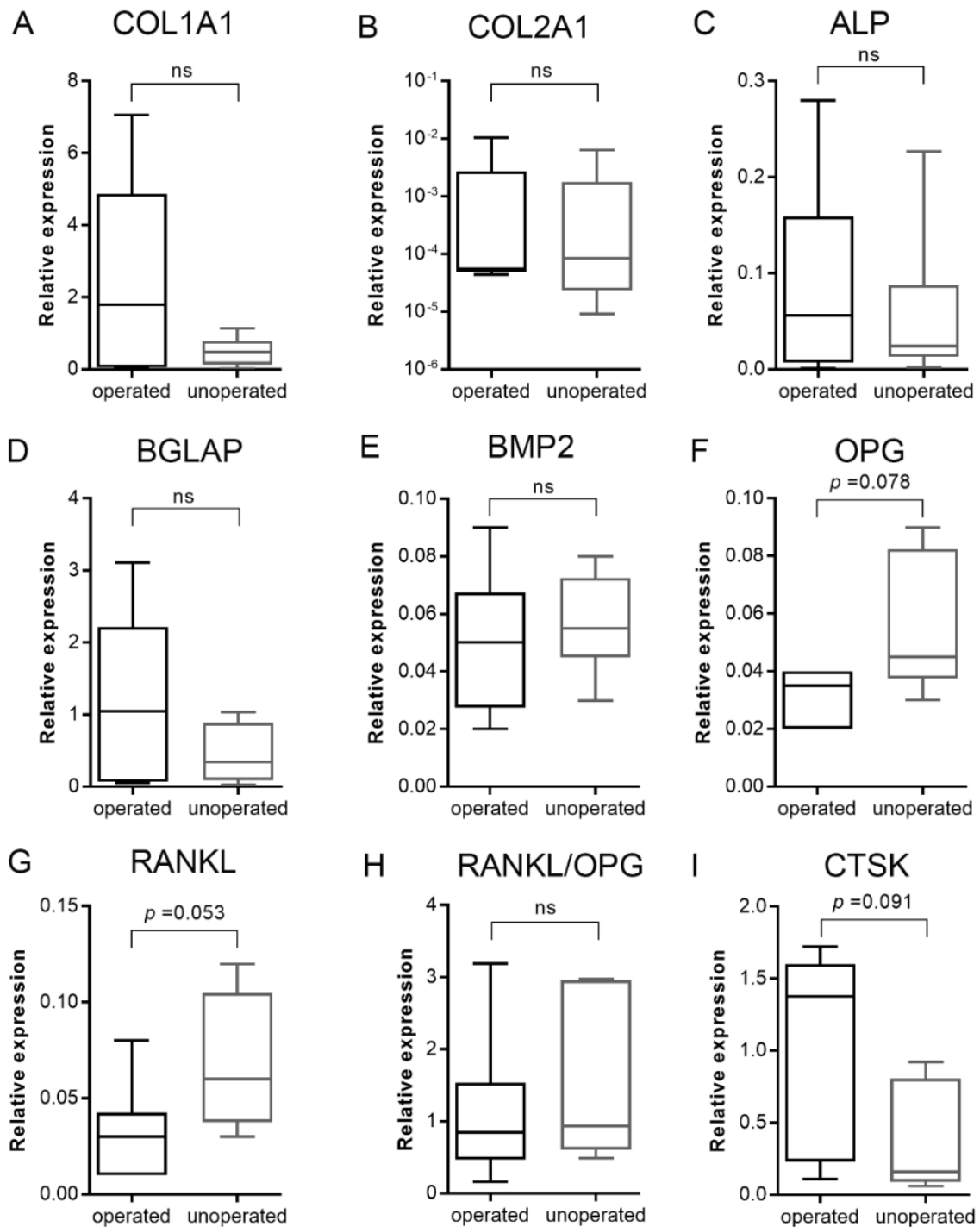


Fig. 18. Relative expression of prominent bone formation and resorption genes. Relative expression of major bone formation markers: CoL1A1 (A), CoL2A1 (B), ALP (C), BGLAP (D), BMP2 (E), and OPG (F) and bone resorption markers: RANKL (G) and CTSK (I) in the operated left and unoperated right femurs. The ratio of RANKL to OPG showed similar expression amounts both in the operated and unoperated contralateral femur (H).

3.9 Bone surface analysis using ToF-SIMS

3.9.1 Calcium and collagen surface mapping revealed similar intensity distribution

The local distribution pattern of calcium and collagen components of the newly formed bone within the fractured area was measured using ToF-SIMS by a collaborator as mentioned in the method section. The mass images of calcium and collagen represented by Ca^+ and $\text{C}_4\text{H}_8\text{N}^+$ signals respectively, as well as overlay images, were generated as shown in figure 19A-C. The calcium mapping revealed a quite homogeneous calcium distribution with increased calcium content in the cortical region. The colour scale encodes the signal intensity for each pixel, which means the brighter the colour, the more the detected signal. The collagen signal also showed a homogeneous distribution within the dense trabecular network. No noticeable difference was seen in the Ca^+ and collagen signal intensity between the newly formed bone that replaced the fractured area and the native bone outside the fracture area. The line scan given the summed signal intensity along the x-direction revealed higher calcium and collagen signal intensity at the dense cortical bone region in comparison to the trabecular bone region. However, within the fractured gap, the line scans complemented the mappings and demonstrated the presence of calcium and collagen in the fractured area.

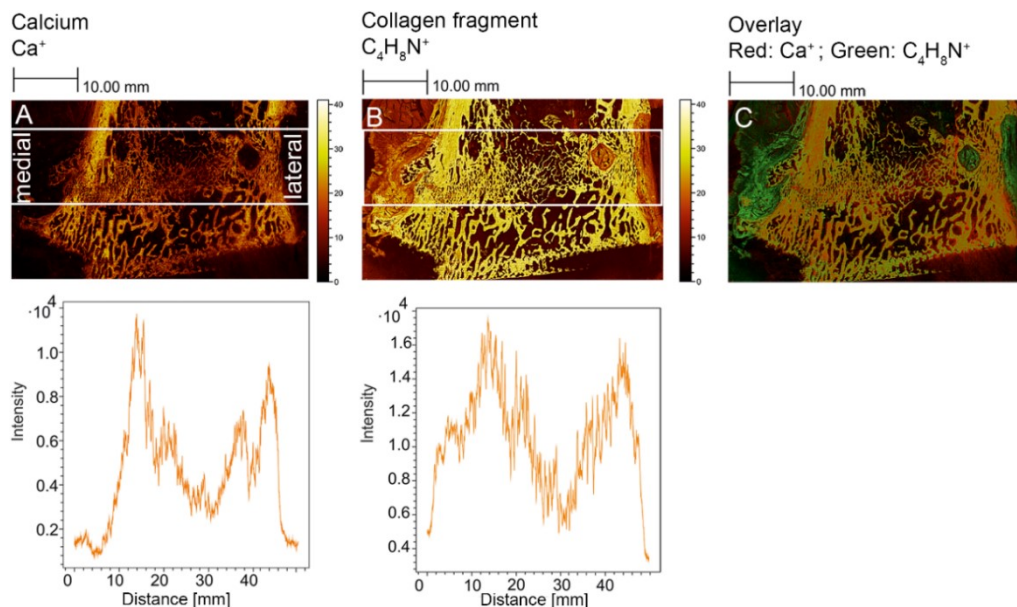


Fig. 19. The local distribution pattern of calcium and collagen in the fractured area. Mass images of (A) Ca^+ and (B) collagen fragment $\text{C}_4\text{H}_8\text{N}^+$ showed homogenous distribution within and outside the fractured area. (C) An overlay image of calcium in red and collagen in green. Unmineralised collagen signal was detectable at the edge of the cortex. The line scans below the Ca^+ and $\text{C}_4\text{H}_8\text{N}^+$ mass images showed the signal intensity of calcium and collagen respectively, within the fractured area, as marked with the white rectangle. The signal intensity generated in y-direction was summed up and plotted with the distance in the x-axis.

3.10 Ultrastructural analysis of the newly formed trabeculae

3.10.1 The localisation of the ROIs for further ultrastructural analysis

Next, to characterise the composition of the organic and inorganic matrix as well as the unique features of osteoblasts, osteoclasts and osteocytes within the new trabeculae. The ultrastructural features were investigated via transmission electron microscopy. First, the samples were cut into semi-thin sections and examined under the light microscope to localise ROIs for further electron microscopic investigation.

The ROI1 revealed an active remodelling zone as shown in figure 20A. The overview image (Fig. 20A) showed a mineralised bone area partly surrounded by an unmineralised area with an active remodelling front. A detail image of ROI1 at 'point B' (Fig. 20B) revealed parallel-aligned collagen fibres with abundant osteoblasts that were embedded inside the osteoid area and surrounded by blood vessels. A close-up image at 'point C', adjacent to the mineralisation front revealed predominantly unaligned collagen fibre with osteocyte-like cells embedded within the matrix (Fig. 20C). The loss of the alignment of the collagen fibres at 'point C' (as opposed to 'point A') indicated an ongoing mineralisation process. This observation is supported by the increased number of young osteocytes originating from the osteoblasts. The Howship's resorption pit was visualised at 'point D' with osteoclasts resorbing the mineralised bone surface (Fig. 20D).

The ROI2 (Fig. 20E) revealed a fully mineralised trabecular bone area with osteoblasts lining the bone surface. A detail image of ROI2 at 'point F' (Fig. 20F) revealed plumb osteoblasts arranged perpendicularly to the bone surface. Also, matured osteocytes were embedded within the mineralised bone area.

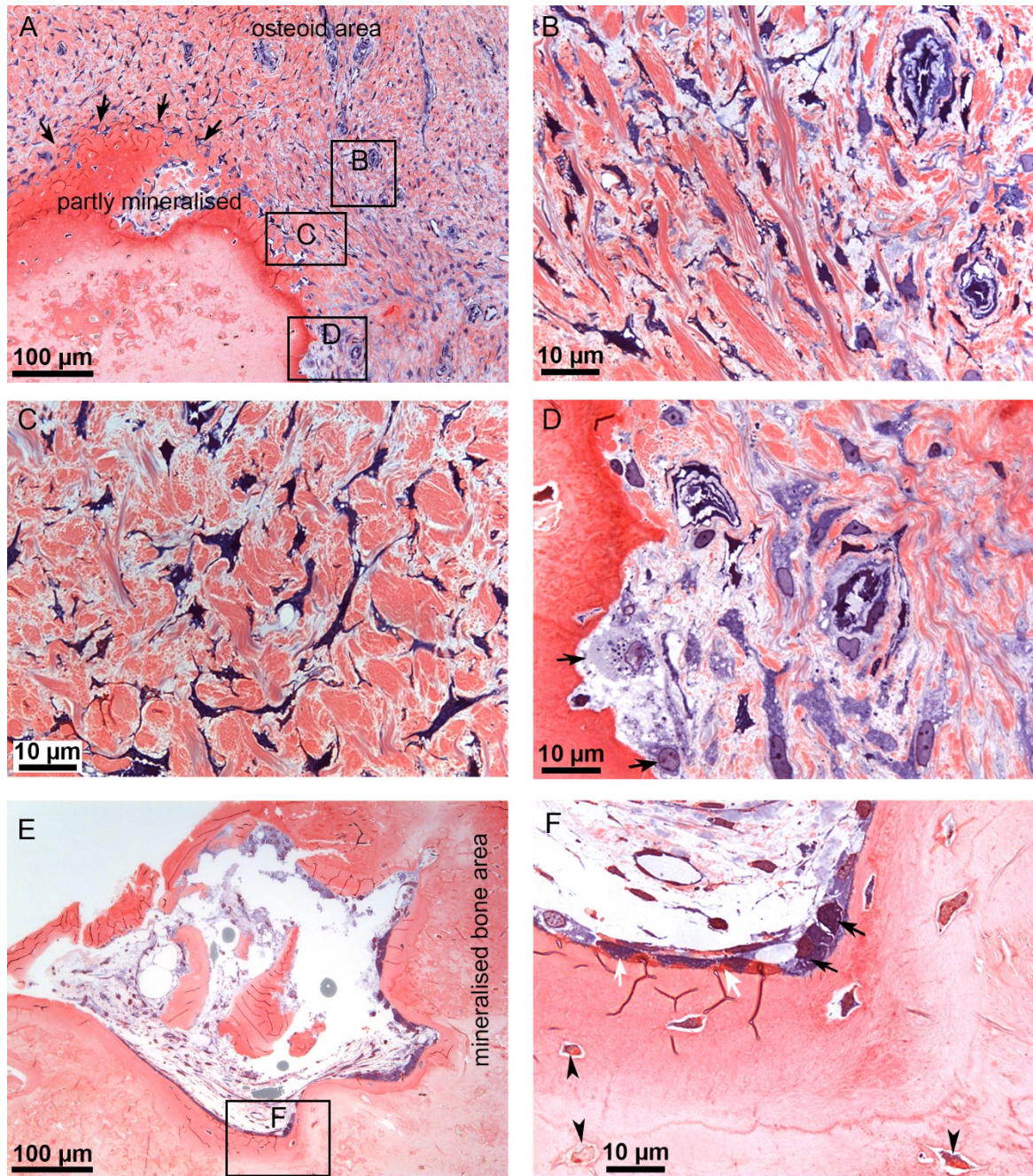


Fig. 20. The localisation of ROIs in the fractured area for further ultrastructural analysis. (A) An overview image of ROI1 showed partly mineralised bone area, osteoid area and an active remodelling front (arrows) within the trabeculae. Blood vessels were evident in the osteoid area. (B) A close-up image of ROI1 at 'point B' showed the parallel alignment of the collagen fibres with an abundance of embedded osteoblasts. (C) A close-up image of ROI1 at 'point C' revealed unaligned collagen fibres with many osteocyte-like cells embedded inside the matrix. (D) A close-up image of ROI1 at 'point C' showed the Howship's resorption pit with osteoclasts resorbing the bone surface (arrows). (E) An overview image of ROI2 showed fully mineralised trabeculae with osteoblasts lining the bone surface. (F) A close-up image of ROI2 at 'point F' showed plumb osteoblasts (black arrows), and flattened osteoblasts (white arrow) arranged perpendicular to the bone surface. Matured osteocytes (black arrowheads) embedded inside the mineralised bone matrix.

3.10.2 Ultrastructure of the organic matrix and the bone mineral material

The unmineralised organic matrix revealed smooth bundles of collagenous fibrils (Fig. 21A-B). The fibril has a thickness of about 50 nm. The fibrils were tightly packed together in parallel orientation and the architecture resembled those of type 1 collagen. The organic matrix was homogeneously mineralised by the densely distributed bone mineral particle of a few nanometres thickness. The deposition of the bone mineral on the organic matrix seemed to have happened both parallel and perpendicularly to the direction of the collagen fibrils. The aggregation of collagen fibrils increased as more mineral particles deposit within and on the fibrillar space. The bone mineral appeared as dense needle-like clusters with a diameter of about 1 μm (Fig. 21C-D).

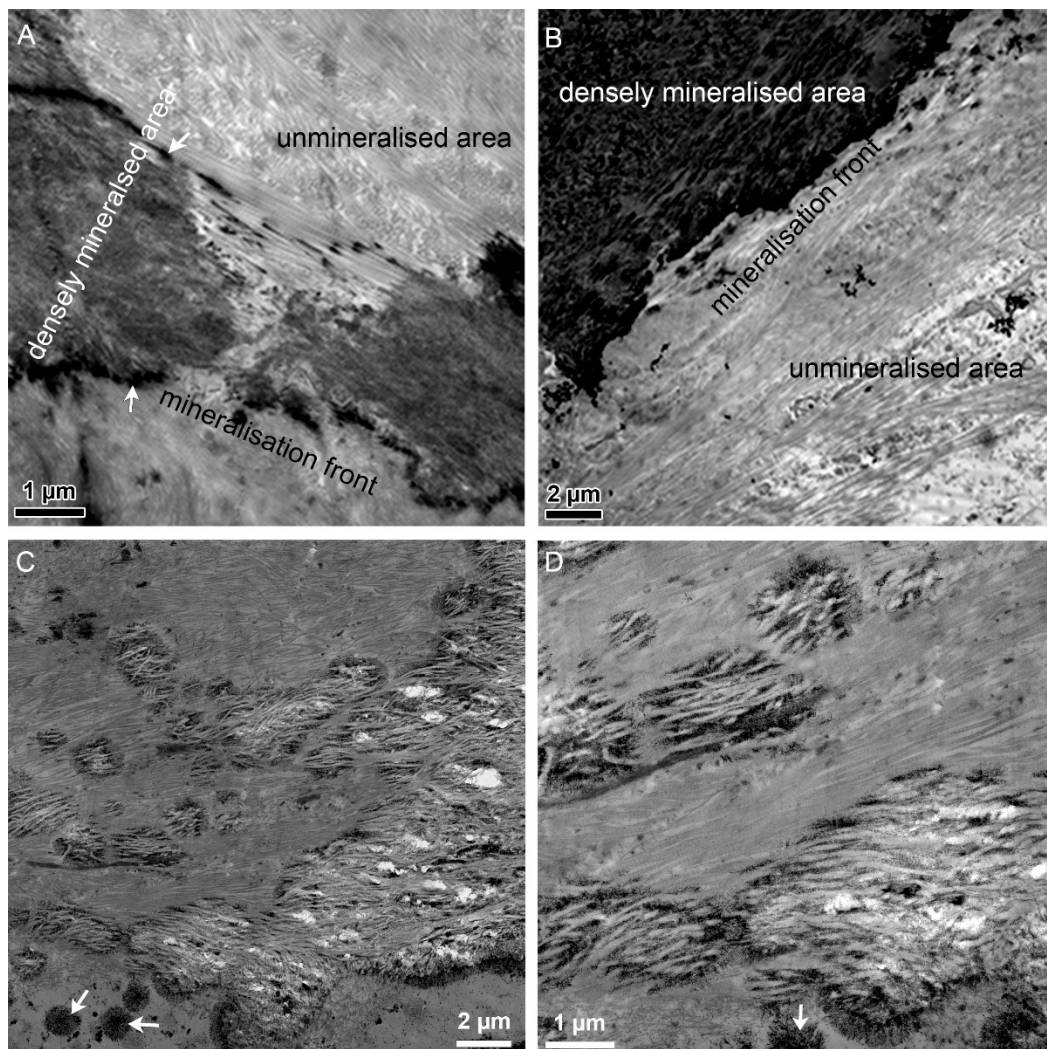


Fig. 21. Ultrastructure of the organic matrix and the bone mineral material. (A-D) Electron micrographs of both ROIs showed the unmineralised organic matrix consisting of majorly collagen fibrils that were closely packed and parallel arranged. The densely mineralised area revealed a homogenous distribution of the bone mineral substance that localised within and on the collagen fibrils. The high electron-dense bone mineral particles appeared as needle-like clusters (arrows). At the active mineralisation front, the organic matrix appeared less dense.

3.10.3 Ultrastructure of the osteoclasts

Large multinucleated osteoclasts actively involved in the resorption process were localised at the trabecular bone surface (Fig. 22A) and in the vicinity of bone (Fig. 22B). Their nuclei surrounded by Golgi apparatus were distributed in the cytoplasm and positioned away from the resorption area. The osteoclasts revealed prominent ruffled borders, known as the active resorption site that directly connected them to the bone surface. Numerous large vacuoles and mitochondria laid very close to the ruffled border (Fig. 22C). A closer focus into the ruffled border (Fig. 22D) revealed deep invaginations of the cell membrane in the locality of the tissue to be resorbed.

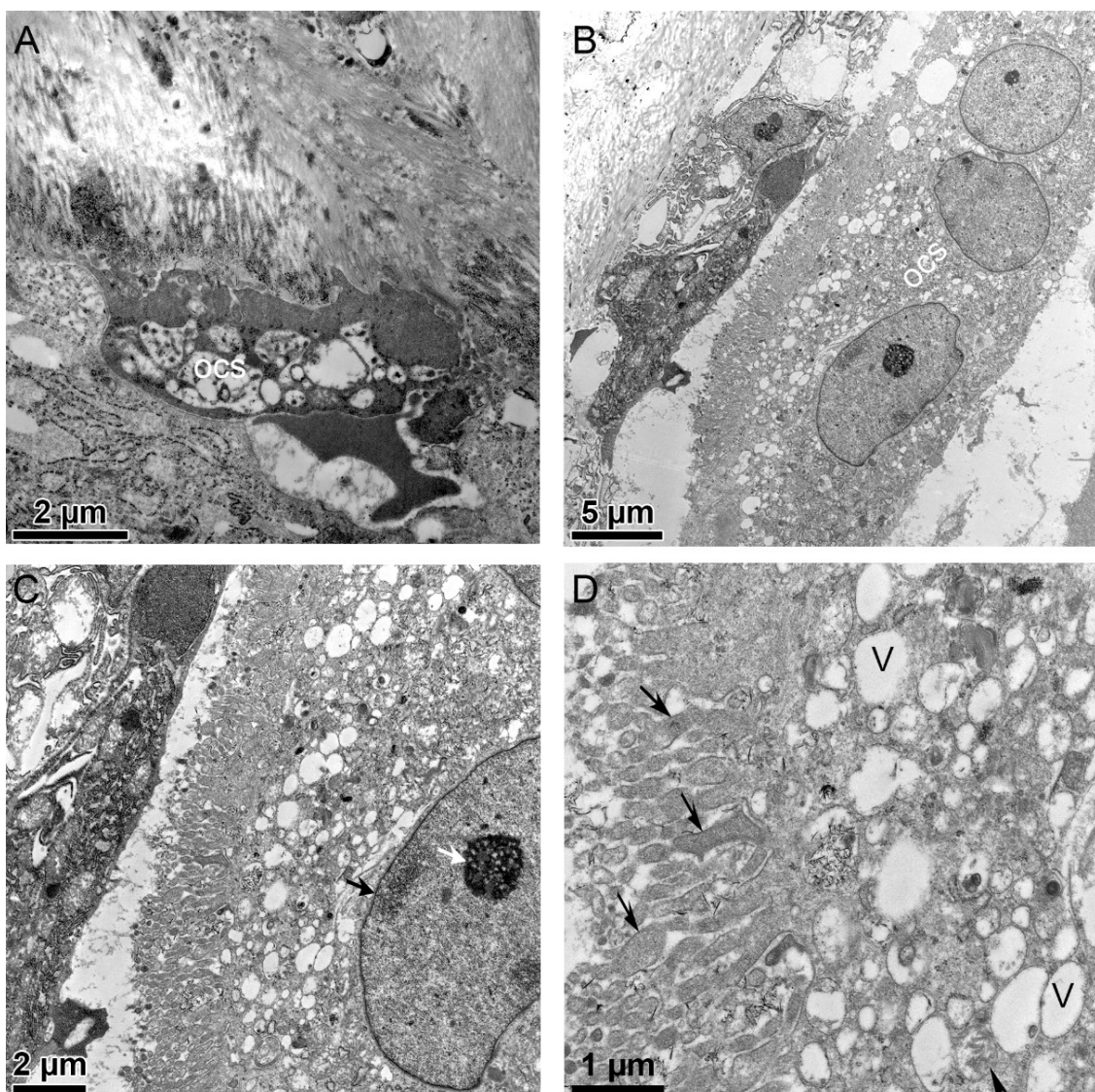


Fig. 22. Ultrastructure of the osteoclasts. Osteoclasts (ocs) actively involved in bone resorption were attached directly to the bone surface (A) and some laid near the bone surface (B). Their large nuclei were positioned away from the resorption area. (C) A detail image of B revealed several cytoplasmic components surrounding the nucleus. The nucleus (black arrow) also revealed its highly electron-dense nucleolus, lying at the centre (white arrow). (D) A close-up image of the ruffled border showed deep invagination of the cell membrane into the resorption area (arrows). Small and large sized vacuoles (labelled V) and mitochondria (arrowhead) localised close to the ruffled border.

3.10.4 Ultrastructure of the osteoblasts

Osteoblasts with different shapes, sizes and arrangements were evident in the trabeculae. Several of the osteoblasts were actively involved in the secretion of the new bone matrix along the mineralised bone surface. The active osteoblasts were mostly cuboidal shaped and arranged perpendicularly to the bone surface with their nucleus positioned opposite to the bone surface (Fig. 23A). A closer look into one of the osteoblasts revealed numerous rough endoplasmic reticulum and mitochondria within the cytoplasm (Fig. 23B). Furthermore, less active osteoblasts that were less plump (Fig. 23C) and some almost flattened along the bone surface (Fig. 23D) were seen lying at the osteoid layer, which separated them from the mineralised bone area. Unlike the active osteoblasts, they appeared less developed and have several elongated cytoplasmic components.

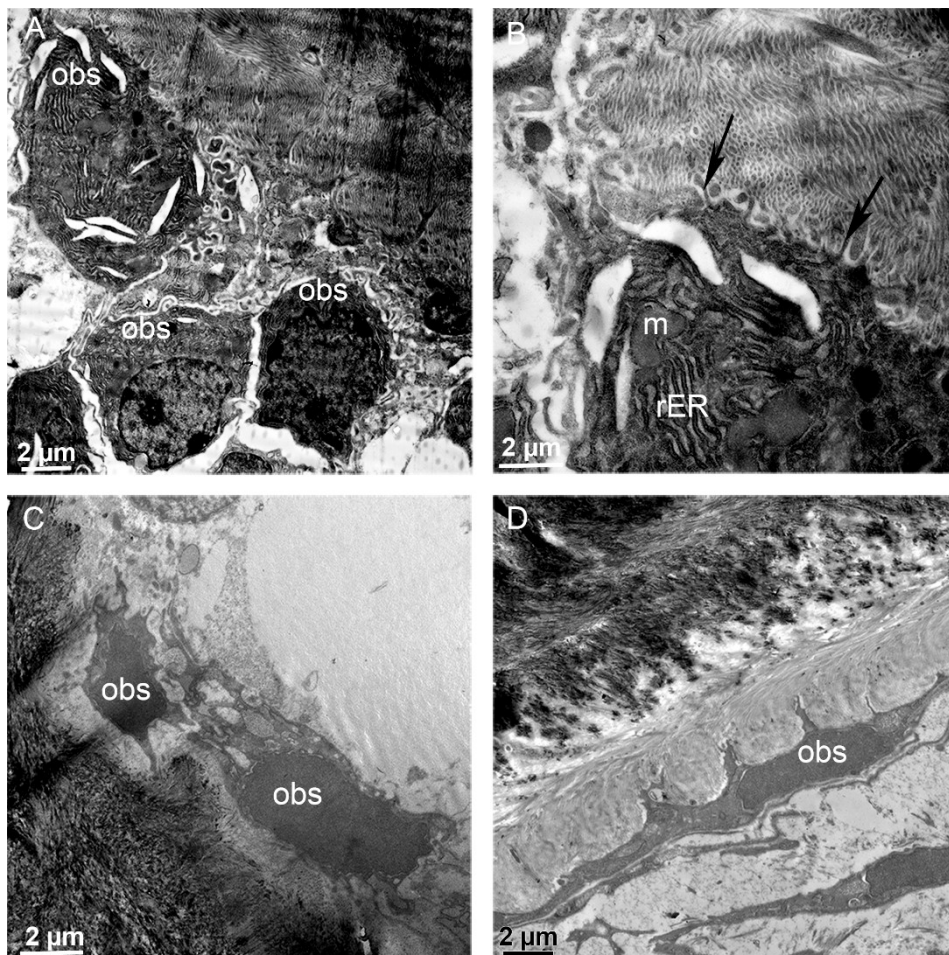


Fig. 23. Ultrastructure of the osteoblasts. (A) Active osteoblasts (obs) in cuboidal shape containing a large nucleus laid perpendicular to the bone surface. (B) A close-up image of an obs revealed several electron dense rough endoplasmic reticulum (rER) and mitochondria (m). The obs were attached to the bone surface via short electron dense filopodia (arrows). Less active obs with elongated cytoplasmic extensions that appeared (C) less cuboidal and (D) flattened were evident. The less active obs occupied the less dense osteoid layer separating them from the more electron dense mineralised bone surface.

3.10.5 Ultrastructure of the osteocytes

Mature star-shaped osteocytes localised individually in flattened periosteocytic lacuna and embedded in the fully mineralised bone matrix were evident in the newly formed trabeculae (Fig. 24A). Furthermore, osteocytes surrounded by osteoid or partially mineralised bone matrix referred to as osteoid-osteocytes or young osteocytes were seen connected via their cytoplasmic extension to osteoblasts at the bone surface as shown in figure 24B. A close-up image of a young osteocyte (Fig. 24B) revealed thin filopodia that linked it to the adjacent osteoblast on the bone surface. In comparison to osteoblasts, their nucleus appeared more prominent, and their cytoplasm seemed less abundant.

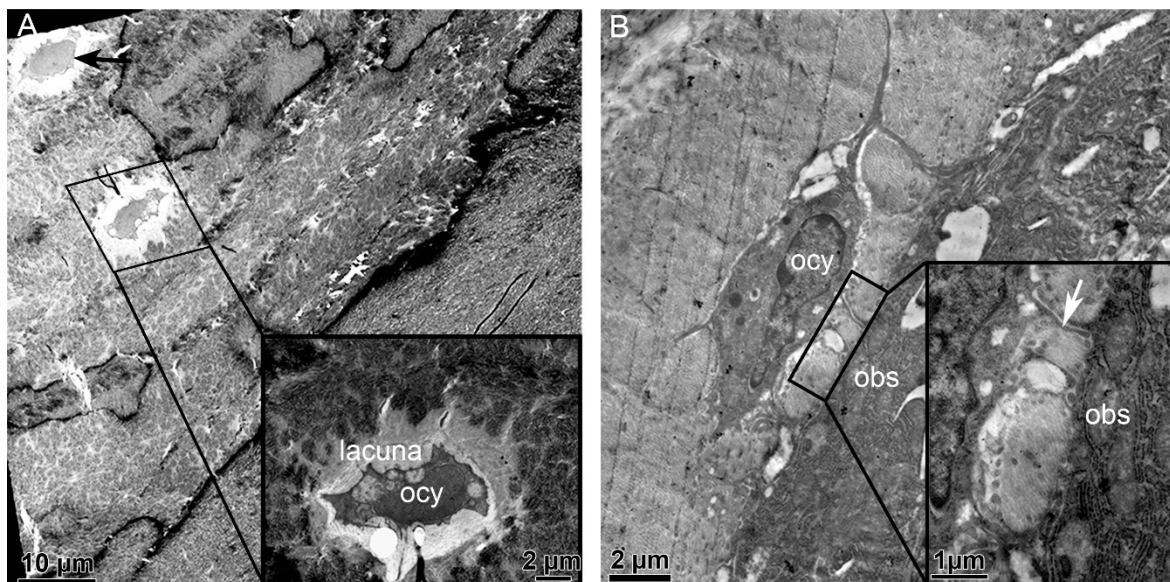


Fig. 24. Ultrastructure of the osteocytes. (A) Micrograph of the matured star-shaped osteocytes (arrow) embedded within the fully mineralised bone matrix. A close-up image of an osteocyte (in the insert) revealed its flattened periosteocytic lacuna and the prominent nucleus. (B) Micrograph of a young osteocyte localised in the osteoid area and connected via the cytoplasmic projections to an adjacent osteoblast. A close-up image of the connecting area as shown in the insert revealed long filopodia (arrow) adjoining the osteocyte to the adjacent osteoblast.

4. DISCUSSION

4.1 Successful establishment of a metaphyseal fracture model in the distal femur of skeletally matured sheep

The first aim of this experimental study was to establish a clinically relevant metaphyseal fracture model in the distal femur of adult sheep. The three main parameters identified from clinical practice to be clinically relevant for such a model include (1) full discontinuity of the metaphyseal area, (2) comparable internal fixation method, and (3) postoperative full weight bearing of the operated hind limb [39], [40]. The establishment of the fracture gap at the distal metaphyseal region of the femur is of clinical relevance due to the high prevalence of fracture at this bone area [25], [57]. Instead of the commonly used partial osteotomy model, a complete osteotomy at the metaphyseal area was generated using a wedge-shaped fracture with a medial gap of approximately 0.1 mm, and a width of 10 mm at the lateral end of the femoral cortex. The full discontinuity allows comparison to frequently observed comminution defect zones in clinical metaphyseal fractures. The fracture gap was stabilised internally using a customised titanium locking plate construct, which is also comparable to the fixation method used in patients with a similar type of fracture. The main benefit of this fixation technique is the allowance of full weight bearing without any restrictions for the animals. Since the selection of an appropriate time point is essential for achieving a successful bone healing, an observation period of 12 weeks was selected for this study based on the suggested estimated time of 10 to 14 weeks for the union of long bone defects in sheep [51], [58], [59].

All animals survived the surgical procedure and returned to their regular activity as well as full load bearing around day three post-surgery. No form of plate breakage or secondary fracture was recorded throughout the 12-week observation period. This confirmed that all the three identified parameters were translated into this large animal model, thus demonstrating a successful establishment of a clinically relevant metaphyseal fracture model.

4.2 Validation of the BMD in the study animals

4.2.1 A comparable BMD at the whole body and femur region of the sheep

Since previous studies have demonstrated that sheep BMD significantly changes with seasonal variation [28], [60]. The initial and final BMD of the whole body and femur region of the animals was determined by DEXA. DEXA is a standard non-invasive method commonly used in the clinic and animal experiments for the assessment of bone quality [51], [61], [62]. The comparable BMD evident at the whole body region of the animals and the similar BMD of the operated left and unoperated right femur indicated that all six sheep have similar BMD status and no seasonal influence on their BMD. The comparable BMD measurement eliminates any potential adverse effect such seasonal variation could have had on the fracture healing, and also indicated that the surgical operation did not affect the general bone quality of the animals. This positive effect could be associated with the angular stable internal fixation that facilitated immediate postoperative full weight bearing of the animals and excluded the need for immobilisation that could have possibly led to a general bone loss. Many reports from patients and animal models have shown that long term immobilisation is a major culprit of mechanical unloading that could result in bone loss [63], [64].

4.3 Characterisation of bone healing in the fractured area

The second aim of this study was to characterise bone healing in the established metaphyseal fracture model relative to the unoperated femur using different analytical methods. The various methods enabled a comprehensive characterisation of metaphyseal bone healing both qualitative and quantitatively. The findings provided in-depth insight on the bone microstructure, bone stiffness and mineralisation, cellular activities of the specialised bone cells, vascularisation, normal ultrastructure of main bone components as well as the activities of prominent bone formation and resorption genes as discussed below.

4.3.1 Bone microstructure

The qualitative micro-CT and histological evaluation of the bone samples from the medial to the lateral end of the fractured gap showed prominent bony bridging from the medial cortex up to two-thirds of the defect. The lack of external callus formation at the lateral end of the cortex is suggestive of improved mechanical stability achieved by the

internal plate fixation. This observation in the fractured metaphysis is similar to those of Claes et al. 1997 [65] who linked periosteal callus formation in metatarsus diaphysis with the size of interfragmentary movement and strain. They showed that higher interfragmentary movement even though in smaller size gap could negatively impact the overall diaphyseal fracture healing and the resulting instability most often leads to external callus formation. A similar finding by Christopher and co-workers showed decreased periosteal callus formation in patients with distal femoral fractures stabilised with stable locking plates [66]. However, the thin layer of periosteal callus found at the end of the medial cortex where the defect was only 0.1 mm wide could be likely due to minor periodic movements at this region since the major stability was provided at the lateral aspect of the femur by the locking plate. Such minor periodic movements are reported to be beneficial for optimal healing of trabecular bone both in human and animal [67]–[69].

The new trabecular bone that bridged the fracture gap formed through a direct membranous bone transformation at the marrow cavity without any visible callus. The absence of cartilaginous tissue within the new trabeculae as evident by the lack of chondrocytes and the insignificant expression of COL2A1 supports the notion of a primary bone formation without an endochondral healing phase that mostly requires cartilage formation. Cartilaginous tissue formation is connected to instability in both cortical and cancellous bone healing. Thus, the direct transformation into new bone without any cartilage stage could also be attributed to the sufficient biomechanical stability provided by the locking plate in this model. These findings support previous observations that metaphyseal bone healing occurs through a direct intramembranous bone formation under stable biomechanical conditions [19]–[21], [70]. Furthermore, the presence of the Haversian system consisting of tightly packed osteons of concentric lamellae at the newly bridged cortical bone area is typical for a matured sheep compact bone and also similar to human subject [32], [60], [71].

The high healing scores of the micro-CT images provided a good impression of the healing outcome and correlated with the quantitative micro-CT results. The increased bone mass also evident by the high percentage bone volume fraction was comparable to the unoperated contralateral femur. The improved quality of the newly formed trabeculae microarchitecture is evident in the derived key morphometric parameters. The significantly higher trabecular thickness and separation of the operated left femur

also indicates a dense trabecula with an abundance of marrow filled cavities. This suggests that bone healing in the fractured femur is still under remodelling process in specific areas, unlike in the contralateral femur where the matured trabeculae are intact with no need for repair, hence the low trabecular thickness [72], [73]. The negative SMI value of the operated femur is also indicative of dense trabeculae with plate-like structure whereas the positive SMI value of the unoperated side suggests thinner trabeculae with more or less rod-like shape [74], [75].

4.3.2 Bone mineralisation and stiffness

The newly formed bone that bridged the fractured gap also attained a substantial level of mineralisation as seen with the higher percentage increase of mineralised bone area that was, however, comparable to the unoperated femur. On the other hand, the significantly higher percentage of the osteoid area in the operated relative to the unoperated femur suggests a rich organic matrix that is still under remodelling process. ToF-SIMS as previously reported is an excellent method to identify mineralised tissue [76], [77]. The high calcium signal detectable within the fractured area also demonstrates high matrix mineralisation. Under-mineralisation with increased heterogeneity of calcium in the bone matrix is reported in patients with fragility fractures in the metaphyseal area [78]. The increased mineralised bone area correlates positively with the high stiffness measured at both the newly formed cortical and trabecular bone areas of the operated femur, which was quite comparable to the unoperated femur. The higher stiffness recorded at the bridged cortical bone area is in line with previous reports and could be attributed to its unique structural features [2], [14], [79]. Furthermore, the similar distribution pattern observed in the collagen component of the fractured area also implies abundant organic matrix. This observation indicates that the quality of both the organic and the inorganic bone components play important roles in the ultimate bone mechanical strength [80]–[82].

4.3.3 Cellular activities of osteoclasts, osteoblasts and osteocytes

The healing process is reflected in the activities of the specialised bone cellular components. The significantly higher activity of osteoblasts observed in the ALP staining indicates new bone formation. The bone formation also manifested in the BMP2 and OPG staining. The increased amount of ALP-activity in the operated femur

could be associated with the increased mineralised bone area, which suggests a possible role in matrix mineralisation [83]. BMP2, a bone matrix derived protein is shown to be more expressed during the early healing phase and subsequently downregulated at the later phase [84]–[86]. Hence, its low expression after this 12-week study period could imply an advance healing stage. Besides, the stimulation of transforming growth factors (for instance the BMPs), are linked to OPG production [87], [88]. Thus, the low expression of BMP2 could be coupled to the decreased amount of OPG. In the operated femur, the ten-fold decrease in TRAP compared to ALP indicates a reduced osteoblast activity. However, the TRAP activity in the operated femur was significantly higher in comparison to the unoperated femur. This finding in line with the micro-CT result indicates that the operated femur, as opposed to the intact contralateral femur is still under active remodelling. Bone resorption in the operated femur is also evident in the RANKL staining. Osteoclast-mediated bone resorption is known to be strongly regulated by the ratio of RANKL to OPG [87], [89]–[93]. Thus, the similar expression amount of OPG and RANKL is suggestive of a controlled resorption process.

The proper formation and maturation process of the newly formed bone is further reflected in the well-established osteocytes-lacunae canaliculi network. Their regular arrangement suggests active involvement of the osteocytes in the regulation of local strains that might have occurred during the mechanical loading episodes thus, implying a role in mechanosensing [2], [94]–[96]. In small animal models of osteoporosis, osteocytes death is associated with a reduction in bone formation and mechanical strength [97], [98]. Similarly, bone loss as reported in an ovine model of osteoporosis and the human subject were caused by low osteocytes density along with an increasing number of empty lacunae [99], [100]. Given that the number of osteocytes and their appropriate response to mechanical stimuli is very vital to the maintenance of superior bone quality, it is thus, certain that the increased density of osteocytes lacunae positively influenced the recruitment of active osteoblasts and osteoclasts as well as other relevant growth factors necessary for the bone remodelling process.

Furthermore, changes in the osteocyte-lacuna morphology and arrangement are recently proposed to influence the way bone responds to the applied mechanical signal with ageing and or in disease condition [96]. A previous study by Carter et al., 2013 [101] showed that osteocytes lacunae of the human femora become smaller and

spherically shaped with ageing. Ubaidus and co-workers [102] reported uniformity in the arrangement of the osteocyte-lacuna canalicular system in healthy bone. Similar to the result of this study, the osteocytes aligned parallel longitudinally to the bone surface and the canaliculi network extended perpendicularly. Therefore, the dominance of spherically shaped osteocytes lacunae along with regular canaliculi system in the newly formed trabeculae of the operated as well as the unoperated femur indicates that the morphological arrangement of the osteocytes positively influenced their overall function.

4.3.4 Vascularisation

The small size and reduced number of blood vessels visualised within the fractured area also suggest an advanced healing stage. The sparse distribution of the blood vessels implies that the healing is at a later stage and thus, does not require major blood vessels formation. The formation of fibrocartilages is linked to inadequate blood supply while bone formation indicates sufficient vascularisation under stable condition [103].

4.3.5 Activities of prominent bone formation and resorption genes

The high expression of important bone formation genes (ALP, BGLAP and COL1A1) relative to the unoperated femur further indicates bone formation. The increased expression of ALP and BGLAP probably relates to the richly mineralised matrix. The low quantity of BMP2 and OPG as similarly observed in quantitative immunohistochemistry confirm both findings and the already stated interpretation.

Conversely, bone resorption is evident in the expressed RANKL and CTSK genes of the operated femur, which is comparable to the unoperated contralateral side. CTSK is a key catabolic enzyme needed for the digestion of the collagenous matrix during the resorption process [104], [105]. Hence, its high level is also suggestive of an active remodelling phase. Regardless of the high CTSK level, there was a low level of RANKL/OPG ratio indicating that the resorption process is well coupled to the new bone formation process as evident by the increased bone mass. The high expression of CTSK could be related to this study time point. This could imply that a high level of CTSK is necessary even at the advanced healing stage since the remodelling process is still in progress. Since osteoclast-mediated bone resorption is strongly regulated by

RANKL/OPG ratio [87], [90] thus, their controlled expression by osteoblasts is vital to achieving a balanced remodelling in healthy bone.

4.3.6 Characteristic ultrastructure of the organic, inorganic and the specialised bone cells

Transmission electron microscopic imaging of the newly formed trabecular bone was performed to characterise the ultrastructure of the collagen-mineral composite, osteoblasts, osteoclasts as well as the osteocytes. A rich organic matrix majorly consisting of collagenous protein was evident. The typical parallel arrangement of the collagen fibrils resembles that of a normal human lamella bone [106]. Major mineralisation of the organic matrix evident in the dense and uniformly distributed bone mineral substance implies bone maturation. The dense needle-like clusters of the bone mineral substance laid within and upon the collagen fibrils, consequently reinforcing their regular cross-linking [9], [12], [107]. The less electron dense area observed close to the mineralisation front suggests an ongoing mineralisation process. Thus, the unique composition and structural arrangement of the collagen fibrils and the bone mineral substance at the osteoid and mineralised bone areas respectively, indicate that they both contribute to the final bone quality [82], [108].

The large multinucleated osteoclasts with the typical ruffled border attached directly to the surface of the newly formed trabeculae show their active involvement in the remodelling process [13], [109]. The abundant vacuoles situated adjacent to the ruffled border are necessary for the digestion and transportation of cellular debris produced during the bone resorption process [10]. Alterations in the structure and function of osteoclasts result in several bone pathologies [110].

The unique morphology and size of the osteoblasts reveal their level of activity. Previous reports have also shown that the shape, size and arrangement of osteoblasts is a reflection of the activity level [111], [112]. The plump cuboidal-shaped osteoblasts characterised by a larger surface area and enriched cytoplasmic components, notably the abundant rough endoplasmic reticulum and mitochondria; indicate their active involvement in the secretion of the new bone matrix whereas the flattened osteoblasts characterised by several elongated cytoplasmic extensions with a poorly developed cytoplasm possibly suggest a reduction in activity.

The ultrastructure of the osteocytes differed depending on the level of bone mineralisation. The matured star-shaped osteocytes localise individually in flattened periosteocytic lacuna and embed within the fully mineralised bone area. The osteocytes embedded in the osteoid and partially mineralised bone regions connect via their cytoplasmic extensions to adjacent osteoblasts at the bone surface. Those located in the osteoid area are termed osteoid osteocytes whereas those located in the partially mineralised area are called young osteocytes [94], [113]. Generally, the structure of the osteoid or young osteocytes seemed more developed than the matured osteocytes. This observation indicates that the young osteocytes are probably involved in the bone maturation process. Moreover, by connecting directly to adjacent osteoblasts, the young osteocytes could play important roles in inter-cellular communication as well as molecular transports [114].

4.4 Limitations of the study

The two main limitations of this study are the small sample size and the use of a single observation time point. Although more sample size could have improved the outcome of the statistical analysis, this was not possible due to the strong European welfare act on the use of laboratory animals that encourages the use of a reduced number of animals for experimental purpose. Secondly, additional time points such as an earlier study period would have enabled a better understanding of the molecular and cellular events occurring during the early phase of bone healing. For example, studying the early phase of bone healing could have provided new insights on the impact of the initial mechanical condition at the fracture area during the early remodelling phase. However, an additional time point was not possible due to the small sample size.

5. CONCLUSION

This study established and characterised a clinically relevant fracture model for metaphyseal bone healing in the distal femur of adult sheep. In contrast to the commonly used partial osteotomy model, this metaphyseal fracture model is the first large animal model to employ full discontinuity at the metaphysis and use a clinically relevant internal fixation technique to stabilise the fracture area. The customised anatomical locking plate conferred sufficient mechanical stability on the fractured area that enabled direct postoperative full weight bearing in the animals. The use of different analytical (both qualitative and quantitative) methods in this study enabled the comprehensive characterisation of the metaphyseal bone healing in the operated left femur relative to the unoperated contralateral femur at 12 weeks post-fracture. The results taken together showed an advanced bony bridging at the fractured area that was characterised by densely mineralised trabeculae. The improved quality of the newly formed trabecular microarchitecture reflected positively in the key morphometric indices. The advanced healing and maturation of the newly formed trabeculae also reflected on the increased mineralised bone area, high density of regularly arranged osteocytes-lacunae along with their canaliculi network, similar biomechanical competence and reduced vasculature. Bone formation and moderate resorption activities of osteoblasts and osteoclasts respectively were evident in tested markers at various stages, namely tissue, molecular, cellular and gene expression levels. This study also presents an in-depth ultrastructure analysis of the newly formed trabeculae using TEM imaging. The characteristic ultrastructure of the collagen-mineral composite and those of the specialised bone cells (osteoblast, osteoclasts and osteocytes) also support normal bone healing and maturation.

The metaphyseal bone area healed through a direct intramembranous bone formation, which is typical and unique to the trabecular bone without visible callus and cartilaginous tissue formation. This large animal model enabled direct metaphyseal healing study without the influence of any material. Thus, the findings explicitly reveal the characteristic healing pattern of the metaphyseal bone under stable internal fixation.

In conclusion, this newly established metaphyseal fracture model is of interest to study bone healing and treatment options for the enhancement of metaphyseal fractures.

6. REFERENCES

- [1] R. S. Taichman, "Blood and bone: two tissues whose fates are intertwined to create the hematopoietic stem-cell niche.," *Blood*, vol. 105, no. 7, pp. 2631–9, Apr. 2005.
- [2] B. Clarke, "Normal bone anatomy and physiology.," *Clin. J. Am. Soc. Nephrol.*, vol. 3 Suppl 3, pp. 131–139, 2008.
- [3] J. J. Alexander, J. J. Piotrowski, D. Graham, D. Franceschi, and T. King, "Outcome of complex vascular and orthopedic injuries of the lower extremity," *Am. J. Surg.*, vol. 162, no. 2, pp. 111–116, 1991.
- [4] D. Rixen, S. Sauerland, H.-J. Oestern, and B. Bouillon, "[Management strategies in the first operative phase after long-bone injury of the lower extremity in multiple-injured patients. A systematic literature review].," *Unfallchirurg*, vol. 108, no. 10, pp. 829–38, 840–2, Oct. 2005.
- [5] R. Oftadeh, M. Perez-Viloria, J. C. Villa-Camacho, A. Vaziri, and A. Nazarian, "Biomechanics and Mechanobiology of Trabecular Bone: A Review," *J. Biomech. Eng.*, vol. 137, no. 1, p. 010802, 2015.
- [6] K. Choi and S. A. Goldstein, "a Comparison of the Fatigue Behavior of Human," vol. 25, no. 12, 1992.
- [7] J. Kragstrup and F. Melsen, "Three-dimensional morphology of trabecular bone osteons reconstructed from serial sections," *Metab. Bone Dis. Relat. Res.*, vol. 5, no. 3, pp. 127–130, 1983.
- [8] W. S. S. Jee, "The skeletal tissues," in *Histology: Cell and Tissue Biology*, Fifth., L. Weiss, Ed. Amsterdam: Elsevier Biomedical/ Elsevier Science Publishing Co., Inc, 1983, pp. 200–255.
- [9] E. Bonucci, "The structural basis of calcification," in *Ultrastructure of the Connective Tissue Matrix*, A. Ruggeri and P. M. Motta, Eds. Boston, MA: Springer US, 1984, pp. 165–191.
- [10] S. C. Marks and S. N. Popoff, "Bone cell biology: The regulation of development, structure, and function in the skeleton," *Am. J. Anat.*, vol. 183, no. 1, pp. 1–44, Sep. 1988.
- [11] A. S. Posner, "The mineral of bone.," *Clin. Orthop. Relat. Res.*, no. 200, pp. 87–99, Nov. 1985.
- [12] S. Lees and K. Probst, "The locus of mineral crystallites in bone.," *Connect. Tissue Res.*, vol. 18, no. 1, pp. 41–54, 1988.
- [13] G. Boivin, C. Anthoine-Terrier, and K. J. Obrant, "Transmission electron microscopy of bone tissue. A review.," *Acta Orthop. Scand.*, vol. 61, no. 2, pp. 170–80, Apr. 1990.
- [14] R. Oftadeh, V. Entezari, G. Sporri, J. C. Villa-Camacho, H. Krigbaum, E. Strawich, L. Graham, C. Rey, H. Chiu, R. Muller, H. N. Hashemi, A. Vaziri, and A. Nazarian, "Hierarchical analysis and multi-scale modelling of rat cortical and trabecular bone," *J. R. Soc. Interface*, vol. 12, no. 106, pp. 20150070–20150070, 2015.

- [15] A. Fritsch and C. Hellmich, "‘Universal’ microstructural patterns in cortical and trabecular, extracellular and extravascular bone materials: micromechanics-based prediction of anisotropic elasticity.," *J. Theor. Biol.*, vol. 244, no. 4, pp. 597–620, Feb. 2007.
- [16] P. Augat, K. Margevicius, J. Simon, S. Wolf, G. Suger, and L. Claes, "Local tissue properties in bone healing: influence of size and stability of the osteotomy gap.," *J. Orthop. Res.*, vol. 16, no. 4, pp. 475–481, 1998.
- [17] A.-B. M. Rabie, Z. Dan, and N. Samman, "Ultrastructural identification of cells involved in the healing of intramembranous and endochondral bones Research; development," *Int. J. Oral M~zTillofac. Surg. J. Oral Mctrillofac. Sttrg*, vol. 25, no. 25, pp. 383–388, 1996.
- [18] F. Shapiro, "Bone development and its relation to fracture repair. The role of mesenchymal osteoblasts and surface osteoblasts," *Eur. Cells Mater.*, vol. 15, pp. 53–76, 2008.
- [19] L. Claes, A. Veesser, M. Göckelmann, U. Simon, and A. Ignatius, "A novel model to study metaphyseal bone healing under defined biomechanical conditions," *Arch. Orthop. Trauma Surg.*, vol. 129, no. 7, pp. 923–928, 2009.
- [20] O. H. Sandberg and P. Aspenberg, "Inter-trabecular bone formation: a specific mechanism for healing of cancellous bone: A narrative review," *Acta Orthop.*, vol. 87, no. 5, pp. 459–465, 2016.
- [21] W. T. Chen, D. C. Han, P. X. Zhang, N. Han, Y. H. Kou, X. F. Yin, and B. G. Jiang, "A special healing pattern in stable metaphyseal fractures," *Acta Orthop.*, vol. 86, no. 2, pp. 238–242, 2015.
- [22] D. Han, N. Han, F. Xue, and P. Zhang, "A novel specialized staging system for cancellous fracture healing, distinct from traditional healing pattern of diaphysis corticalfracture?," *Int. J. Clin. Exp. Med.*, vol. 8, no. 1, pp. 1301–4, 2015.
- [23] J. E. Aaron and T. M. Skerry, "Intramembranous trabecular generation in normal bone.," *Bone Miner.*, vol. 25, no. 3, pp. 211–30, Jun. 1994.
- [24] T. Kon, T. J. Cho, T. Aizawa, M. Yamazaki, N. Nooh, D. Graves, L. C. Gerstenfeld, and T. A. Einhorn, "Expression of osteoprotegerin, receptor activator of NF-kappaB ligand (osteoprotegerin ligand) and related proinflammatory cytokines during fracture healing.," *J. Bone Miner. Res.*, vol. 16, no. 6, pp. 1004–14, Jun. 2001.
- [25] L. Mosekilde, E. N. Ebbesen, L. Tornvig, and J. S. Thomsen, "Trabecular bone structure and strength - remodelling and repair," *J Musculoskelet Neuronal Interact*, vol. 1, no. 1, pp. 25–30, 2000.
- [26] T. Komori, "Animal models for osteoporosis.," *Eur. J. Pharmacol.*, vol. 759, pp. 287–94, Jul. 2015.
- [27] L. Martini, M. Fini, G. Giavaresi, and R. Giardino, "Sheep model in orthopedic research: a literature review," *Comp. Med.*, vol. 51, no. 4, pp. 292–299, 2001.
- [28] A. S. Turner, "The sheep as a model for osteoporosis in humans," *Vet. J.*, vol. 163, no. 3, pp. 232–239, 2002.
- [29] S. Reinwald and D. Burr, "Review of nonprimate, large animal models for

- osteoporosis research.," *J. Bone Miner. Res.*, vol. 23, no. 9, pp. 1353–68, Sep. 2008.
- [30] A. I. Pearce, R. G. Richards, S. Milz, E. Schneider, and S. G. Pearce, "Animal models for implant biomaterial research in bone: A review," *Eur. Cells Mater.*, vol. 13, no. 0, pp. 1–10, 2007.
- [31] R. Mori, T. Kodaka, S. Soeta, J. Sato, J. Kakino, S. Hamato, H. Takaki, and Y. Naito, "Preliminary study of histological comparison on the growth patterns of long-bone cortex in young calf, pig, and sheep.," *J. Vet. Med. Sci.*, vol. 67, no. 12, pp. 1223–9, Dec. 2005.
- [32] D. N. Kalu, "Animal Models of the Aging Skeleton," in *The Aging Skeleton*, 1st ed., J. G. Clifford J. Rosen and John P. Bilezikian, Eds. Academic Press, 1999, pp. 37–50.
- [33] R. Oheim, M. Amling, A. Ignatius, and P. Pogoda, "Large animal model for osteoporosis in humans: the ewe.," *Eur. Cell. Mater.*, vol. 24, pp. 372–85, Nov. 2012.
- [34] V. Borsari, M. Fini, G. Giavaresi, L. Rimondini, U. Consolo, L. Chiusoli, A. Salito, A. Volpert, R. Chiesa, and R. Giardino, "Osteointegration of titanium and hydroxyapatite rough surfaces in healthy and compromised cortical and trabecular bone: in vivo comparative study on young, aged, and estrogen-deficient sheep," *J. Orthop. Res.*, vol. 25, no. 9, pp. 1250–1260, Sep. 2007.
- [35] M. Rocca, M. Fini, G. Giavaresi, N. Nicoli Aldini, and R. Giardino, "Osteointegration of hydroxyapatite-coated and uncoated titanium screws in long-term ovariectomized sheep," *Biomaterials*, vol. 23, no. 4, pp. 1017–1023, 2002.
- [36] A. Malhotra, M. H. Pelletier, Y. Yu, C. Christou, and W. R. Walsh, "A Sheep Model for Cancellous Bone Healing," *Front. Surg.*, vol. 1, no. September, pp. 1–7, 2014.
- [37] L. Claes, A. Veeseer, M. Göckelmann, U. Simon, and A. Ignatius, "A novel model to study metaphyseal bone healing under defined biomechanical conditions.," *Arch. Orthop. Trauma Surg.*, vol. 129, no. 7, pp. 923–8, Jul. 2009.
- [38] R. Bindl, R. Oheim, P. Pogoda, F. T. Beil, K. Gruchenberg, S. Reitmaier, T. Wehner, E. Calcia, P. Radermacher, L. Claes, M. Amling, and A. Ignatius, "Metaphyseal fracture healing in a sheep model of low turnover osteoporosis induced by hypothalamic-pituitary disconnection (HPD)," *J. Orthop. Res.*, vol. 31, no. 11, pp. 1851–1857, 2013.
- [39] W. H. Cheung, T. Miclau, S. K. H. Chow, F. F. Yang, and V. Alt, "Fracture healing in osteoporotic bone," *Injury*, vol. 47, pp. S21–S26, 2016.
- [40] R. M. Y. Wong, M. H. V. Choy, M. C. M. Li, K.-S. Leung, S. K-H. Chow, W.-H. Cheung, and J. C. Y. Cheng, "A systematic review of current osteoporotic metaphyseal fracture animal models," *Bone Joint Res.*, vol. 7, no. 1, pp. 6–11, Jan. 2018.
- [41] M. E. Wullschleger, R. Steck, R. Matthys, J. Webster, M. A. Woodruff, R. Devakar, K. Ito, and M. Schuetz, "A new model to study healing of a complex femur fracture with concurrent soft tissue injury in sheep," *Open J. Orthop.*, vol.

- 3, no. June, pp. 1–7, 2013.
- [42] C. A. Lill, J. Hessel, U. Schlegel, C. Eckhardt, J. Goldhahn, and E. Schneider, “Biomechanical evaluation of healing in a non-critical defect in a large animal model of osteoporosis,” *J. Orthop. Res.*, vol. 21, no. 5, pp. 836–842, 2003.
- [43] M. J. Challis, P. Gaston, K. Wilson, G. A. Jull, and R. W. Crawford, “Cyclic pneumatic soft-tissue compression accelerates the union of distal radial osteotomies in an ovine model,” *J Bone Jt. Surg Br*, vol. 88, no. 3, pp. 411–415, 2006.
- [44] D. R. Epari, H. Schell, H. J. Bail, and G. N. Duda, “Instability prolongs the chondral phase during bone healing in sheep,” *Bone*, vol. 38, no. 6, pp. 864–870, 2006.
- [45] P. Tufekci, A. Tavakoli, C. Dlaska, M. Neumann, M. Shanker, S. Saifzadeh, R. Steck, M. Schuetz, and D. Epari, “Early mechanical stimulation only permits timely bone healing in sheep,” *J. Orthop. Res.*, vol. 36, no. 6, pp. 1790–1796, 2018.
- [46] R. Hente, J. Cordey, B. A. Rahn, M. Maghsudi, S. von Gumpfenberg, and S. M. Perren, “Fracture healing of the sheep tibia treated using a unilateral external fixator. Comparison of static and dynamic fixation,” *Injury*, vol. 30, Supple, pp. SA44-SA51, 1999.
- [47] P. Augat, J. Merk, S. Wolf, and L. Claes, “Mechanical stimulation by external application of cyclic tensile strains does not effectively enhance bone healing.,” *J. Orthop. Trauma*, vol. 15, no. 1, pp. 54–60, Jan. 2001.
- [48] L. E. Claes, H.-J. Wilke, P. Augat, S. Rübenacker, and K. J. Margevicius, “Effect of dynamization on gap healing of diaphyseal fractures under external fixation.,” *Clin. Biomech. (Bristol, Avon)*, vol. 10, no. 5, pp. 227–234, Jul. 1995.
- [49] S. Wolf, A. Janousek, J. Pfeil, W. Veith, F. Haas, G. Duda, and L. Claes, “The effects of external mechanical stimulation on the healing of diaphyseal osteotomies fixed by flexible external fixation.,” *Clin. Biomech. (Bristol, Avon)*, vol. 13, no. 4–5, pp. 359–364, Jun. 1998.
- [50] M. L. Bouxsein, S. K. Boyd, B. A. Christiansen, R. E. Guldberg, K. J. Jepsen, and R. Müller, “Guidelines for assessment of bone microstructure in rodents using micro-computed tomography.,” *J. Bone Miner. Res.*, vol. 25, no. 7, pp. 1468–86, Jul. 2010.
- [51] F. C. Den Boer, P. Patka, F. C. Bakker, B. W. Wippermann, A. Van Lingen, G. Q. M. Vink, K. Boshuizen, and H. J. T. M. Haarman, “New segmental long bone defect model in sheep: Quantitative analysis of healing with dual energy x-ray absorptiometry,” *J. Orthop. Res.*, vol. 17, no. 5, pp. 654–660, 1999.
- [52] E. F. Morgan, Z. D. Mason, K. B. Chien, A. J. Pfeiffer, G. L. Barnes, T. A. Einhorn, and L. C. Gerstenfeld, “Micro-computed tomography assessment of fracture healing: Relationships among callus structure, composition, and mechanical function,” *Bone*, vol. 44, no. 2, pp. 335–344, 2009.
- [53] J. S. Nyman, S. Munoz, S. Jadhav, A. Mansour, T. Yoshii, G. R. Mundy, and G. E. Gutierrez, “Quantitative measures of femoral fracture repair in rats derived by micro-computed tomography,” *J. Biomech.*, vol. 42, no. 7, pp. 891–897, 2009.

- [54] K. J. Livak and T. D. Schmittgen, "Analysis of relative gene expression data using real-time quantitative PCR and the 2(-Delta Delta C(T)) Method.," *Methods*, vol. 25, no. 4, pp. 402–8, Dec. 2001.
- [55] B. W. Schueler, "Time-of-flight mass analysers," in *TOF-SIMS: materials analysis by mass spectrometry*, 2nd ed., J. C. Vickerman and D. Briggs, Eds. Chichester: IM Publications LLP, 2012, p. 732.
- [56] A. Henss, M. Rohnke, T. El Khassawna, P. Govindarajan, G. Schlewitz, C. Heiss, and J. Janek, "Applicability of ToF-SIMS for monitoring compositional changes in bone in a long-term animal model," *J. R. Soc. Interface*, vol. 10, no. 86, pp. 20130332–20130332, 2013.
- [57] B. L. Riggs and L. J. Melton, "Involitional osteoporosis.," *N. Engl. J. Med.*, vol. 314, no. 26, pp. 1676–86, Jun. 1986.
- [58] L. A. Mills and A. H. R. W. Simpson, "In vivo models of bone repair.," *J. Bone Joint Surg. Br.*, vol. 94, no. 7, pp. 865–74, Jul. 2012.
- [59] C. Christou, R. A. Oliver, M. H. Pelletier, and W. R. Walsh, "Ovine model for critical-size tibial segmental defects," *Comp. Med.*, vol. 64, no. 5, pp. 377–385, 2014.
- [60] D. Arens, I. Sigrist, M. Alini, P. Schawaldler, E. Schneider, and M. Egermann, "Seasonal changes in bone metabolism in sheep.," *Vet. J.*, vol. 174, no. 3, pp. 585–91, Nov. 2007.
- [61] M. D. Markel and J. J. Bogdanske, "The effect of increasing gap width on localized densitometric changes within tibial ostectomies in a canine model.," *Calcif. Tissue Int.*, vol. 54, no. 2, pp. 155–9, Feb. 1994.
- [62] K. Tanaka, T. Kurokawa, K. Nakamura, T. Matsushita, S. Horinaka, I. Kusaba, H. Okazaki, K. Mamada, R. Shiro, W. Ou, and S. C. Hung, "Callus formation in femur and tibia during leg lengthening: 7 patients examined with DXA.," *Acta Orthop. Scand.*, vol. 67, no. 2, pp. 158–60, Apr. 1996.
- [63] W. S. Jee and Y. Ma, "Animal models of immobilization osteopenia.," *Morphologie*, vol. 83, no. 261, pp. 25–34, Jun. 1999.
- [64] C. Alexandre and L. Vico, "Pathophysiology of bone loss in disuse osteoporosis," *Jt. Bone Spine*, vol. 78, no. 6, pp. 572–576, 2011.
- [65] L. Claes, P. Augat, G. Suger, and H. J. Wilke, "Influence of size and stability of the osteotomy gap on the success of fracture healing," *J. Orthop. Res.*, vol. 15, no. 4, pp. 577–584, 1997.
- [66] C. E. Henderson, T. Lujan, M. Bottlang, D. C. Fitzpatrick, S. M. Madey, and J. L. Marsh, "Stabilization of distal femur fractures with intramedullary nails and locking plates: differences in callus formation.," *Iowa Orthop. J.*, vol. 30, no. 319, pp. 61–8, 2010.
- [67] L. Claes, M. Reusch, M. Göckelmann, M. Ohnmacht, T. Wehner, M. Amling, F. T. Beil, and A. Ignatius, "Metaphyseal fracture healing follows similar biomechanical rules as diaphyseal healing," *J. Orthop. Res.*, vol. 29, no. 3, pp. 425–432, 2011.
- [68] M. Lutz, R. Steck, I. Sitte, M. Rieger, M. Schuetz, and T. Klestil, "The

- metaphyseal bone defect in distal radius fractures and its implication on trabecular remodeling—a histomorphometric study (case series),” *J. Orthop. Surg. Res.*, vol. 10, no. 1, pp. 1–7, 2015.
- [69] G. Vicenti, V. Pesce, N. Tartaglia, A. Abate, C. M. Mori, and B. Moretti, “Micromotion in the fracture healing of closed distal metaphyseal tibial fractures: A multicentre prospective study,” *Injury*, vol. 45, no. S6, pp. S27–S35, 2014.
- [70] H. K. Uthoff and B. a Rahn, “Healing patterns of metaphyseal fractures.,” *Clin. Orthop. Relat. Res.*, no. 160, pp. 295–303, 1981.
- [71] M. Martiniaková, B. Grosskopf, R. Omelka, M. Vondráková, and M. Bauerová, “Histological analysis of ovine compact bone tissue.,” *J. Vet. Med. Sci.*, vol. 69, pp. 409–411, 2007.
- [72] D. B. Burr, “Targeted and nontargeted remodeling.,” *Bone*, vol. 30, no. 1, pp. 2–4, Jan. 2002.
- [73] A. M. Parfitt, “Targeted and nontargeted bone remodeling: relationship to basic multicellular unit origination and progression.,” *Bone*, vol. 30, no. 1, pp. 5–7, Jan. 2002.
- [74] T. Hildebrand, A. Laib, R. Müller, J. Dequeker, and P. Rügsegger, “Direct three-dimensional morphometric analysis of human cancellous bone: microstructural data from spine, femur, iliac crest, and calcaneus.,” *J. Bone Miner. Res.*, vol. 14, no. 7, pp. 1167–74, Jul. 1999.
- [75] T. Hildebrand and P. Rügsegger, “Quantification of Bone Microarchitecture with the Structure Model Index.,” *Comput. Methods Biomech. Biomed. Engin.*, vol. 1, no. 1, pp. 15–23, Jan. 1997.
- [76] S. Ray, U. Thormann, M. Eichelroth, M. Budak, C. Biehl, M. Rupp, U. Sommer, T. El Khassawna, F. I. Alagboso, M. Kampschulte, M. Rohnke, A. Henß, K. Pepler, V. Linke, P. Quadbeck, A. Voigt, F. Stenger, D. Karl, R. Schnettler, C. Heiss, K. S. Lips, and V. Alt, “Strontium and bisphosphonate coated iron foam scaffolds for osteoporotic fracture defect healing,” *Biomaterials*, vol. 157, pp. 1–16, 2018.
- [77] U. Thormann, S. Ray, U. Sommer, T. Elkhassawna, T. Rehling, M. Hundgeburth, A. Henß, M. Rohnke, J. Janek, K. S. Lips, C. Heiss, G. Schlewitz, G. Szalay, M. Schumacher, M. Gelinsky, R. Schnettler, and V. Alt, “Bone formation induced by strontium modified calcium phosphate cement in critical-size metaphyseal fracture defects in ovariectomized rats.,” *Biomaterials*, vol. 34, no. 34, pp. 8589–98, Nov. 2013.
- [78] N. Fratzi-Zelman, P. Roschger, B. M. Misof, K. Nawrot-Wawrzyniak, S. Pötter-Lang, C. Muschitz, H. Resch, K. Klaushofer, and E. Zwettler, “Fragility fractures in men with idiopathic osteoporosis are associated with undermineralization of the bone matrix without evidence of increased bone turnover,” *Calcif. Tissue Int.*, vol. 88, no. 5, pp. 378–387, 2011.
- [79] P. K. Zysset, X. Edward Guo, C. Edward Hoffler, K. E. Moore, and S. A. Goldstein, “Elastic modulus and hardness of cortical and trabecular bone lamellae measured by nanoindentation in the human femur,” *J. Biomech.*, vol. 32, no. 10, pp. 1005–1012, 1999.

- [80] X. Wang, X. Shen, X. Li, and C. M. Agrawal, "Age-related changes in the collagen network and toughness of bone.," *Bone*, vol. 31, no. 1, pp. 1–7, Jul. 2002.
- [81] P. Zioupos, J. D. Currey, and A. J. Hamer, "The role of collagen in the declining mechanical properties of aging human cortical bone.," *J. Biomed. Mater. Res.*, vol. 45, no. 2, pp. 108–16, May 1999.
- [82] P. Fratzl, H. S. Gupta, E. P. Paschalis, and P. Roschger, "Structure and mechanical quality of the collagen–mineral nano-composite in bone," *J. Mater. Chem.*, vol. 14, no. 14, pp. 2115–2123, 2004.
- [83] M. P. Whyte, "Hypophosphatasia and the role of alkaline phosphatase in skeletal mineralization.," *Endocr. Rev.*, vol. 15, no. 4, pp. 439–61, Aug. 1994.
- [84] J. Yang, P. Shi, M. Tu, Y. Wang, M. Liu, F. Fan, and M. Du, "Bone morphogenetic proteins: Relationship between molecular structure and their osteogenic activity," *Food Sci. Hum. Wellness*, vol. 3, no. 3–4, pp. 127–135, 2014.
- [85] Y. Y. Yu, S. Lieu, C. Lu, T. Miclau, R. S. Marcucio, and C. Colnot, "Immunolocalization of BMPs, BMP antagonists, receptors, and effectors during fracture repair," *Bone*, vol. 46, no. 3, pp. 841–851, 2010.
- [86] T. J. Cho, L. C. Gerstenfeld, and T. A. Einhorn, "Differential temporal expression of members of the transforming growth factor β superfamily during murine fracture healing," *J. Bone Miner. Res.*, vol. 17, no. 3, pp. 513–520, 2002.
- [87] N. Udagawa, N. Takahashi, H. Yasuda, A. Mizuno, K. Itoh, Y. Ueno, T. Shinki, M. T. Gillespie, T. J. Martin, K. Higashio, and T. Suda, "Osteoprotegerin produced by osteoblasts is an important regulator in osteoclast development and function," *Endocrinology*, vol. 141, no. 9, pp. 3478–3484, 2000.
- [88] M. Schoppet, K. T. Preissner, and L. C. Hofbauer, "RANK ligand and osteoprotegerin: paracrine regulators of bone metabolism and vascular function.," *Arterioscler. Thromb. Vasc. Biol.*, vol. 22, no. 4, pp. 549–53, Apr. 2002.
- [89] M. M. Cohen, "The new bone biology: pathologic, molecular, and clinical correlates.," *Am. J. Med. Genet. A*, vol. 140, no. 23, pp. 2646–706, Dec. 2006.
- [90] W. J. Boyle, W. S. Simonet, and D. L. Lacey, "Osteoclast differentiation and activation.," *Nature*, vol. 423, no. 6937, pp. 337–42, May 2003.
- [91] S. Khosla, "Minireview: the OPG/RANKL/RANK system.," *Endocrinology*, vol. 142, no. 12, pp. 5050–5055, 2001.
- [92] D. L. Lacey, E. Timms, H. L. Tan, M. J. Kelley, C. R. Dunstan, T. Burgess, R. Elliott, A. Colombero, G. Elliott, S. Scully, H. Hsu, J. Sullivan, N. Hawkins, E. Davy, C. Capparelli, A. Eli, Y. X. Qian, S. Kaufman, I. Sarosi, V. Shalhoub, G. Senaldi, J. Guo, J. Delaney, and W. J. Boyle, "Osteoprotegerin ligand is a cytokine that regulates osteoclast differentiation and activation.," *Cell*, vol. 93, no. 2, pp. 165–76, Apr. 1998.
- [93] W. . Simonet, D. . Lacey, C. . Dunstan, M. Kelley, M.-S. Chang, R. Lüthy, H. . Nguyen, S. Wooden, L. Bennett, and T. Boone, "Osteoprotegerin: A Novel Secreted Protein Involved in the Regulation of Bone Density," *Cell*, vol. 89, no.

- 2, pp. 309–319, Apr. 1997.
- [94] E. M. Aarden, E. H. Burger, and P. J. Nijweide, “Function of osteocytes in bone,” *J. Cell. Biochem.*, vol. 55, no. 3, pp. 287–299, 1994.
- [95] J. Klein-Nulend, A. D. Bakker, R. G. Bacabac, A. Vatsa, and S. Weinbaum, “Mechanosensation and transduction in osteocytes,” *Bone*, vol. 54, no. 2, pp. 182–90, Jun. 2013.
- [96] H. Hemmatian, A. D. Bakker, J. Klein-Nulend, and G. H. van Lenthe, “Aging, Osteocytes, and Mechanotransduction,” *Curr. Osteoporos. Rep.*, vol. 15, no. 5, pp. 401–411, 2017.
- [97] Y.-L. Ma, R.-C. Dai, Z.-F. Sheng, Y. Jin, Y.-H. Zhang, L.-N. Fang, H.-J. Fan, and E.-Y. Liao, “Quantitative associations between osteocyte density and biomechanics, microcrack and microstructure in OVX rats vertebral trabeculae,” *J. Biomech.*, vol. 41, no. 6, pp. 1324–32, 2008.
- [98] C. A. O’Brien, D. Jia, L. I. Plotkin, T. Bellido, C. C. Powers, S. A. Stewart, S. C. Manolagas, and R. S. Weinstein, “Glucocorticoids act directly on osteoblasts and osteocytes to induce their apoptosis and reduce bone formation and strength,” *Endocrinology*, vol. 145, no. 4, pp. 1835–1841, 2004.
- [99] M. G. Mullender, S. D. Tan, L. Vico, C. Alexandre, and J. Klein-Nulend, “Differences in osteocyte density and bone histomorphometry between men and women and between healthy and osteoporotic subjects,” *Calcif. Tissue Int.*, vol. 77, no. 5, pp. 291–6, Nov. 2005.
- [100] M. R. Zarrinkalam, A. Mulaibrahimovic, G. J. Atkins, and R. J. Moore, “Changes in osteocyte density correspond with changes in osteoblast and osteoclast activity in an osteoporotic sheep model,” *Osteoporos. Int.*, vol. 23, no. 4, pp. 1329–1336, 2012.
- [101] Y. Carter, C. D. L. Thomas, J. G. Clement, and D. M. L. Cooper, “Femoral osteocyte lacunar density, volume and morphology in women across the lifespan,” *J. Struct. Biol.*, vol. 183, no. 3, pp. 519–526, Sep. 2013.
- [102] S. Ubaidus, M. Li, S. Sultana, P. H. L. de Freitas, K. Oda, T. Maeda, R. Takagi, and N. Amizuka, “FGF23 is mainly synthesized by osteocytes in the regularly distributed osteocytic lacunar canalicular system established after physiological bone remodeling,” *J. Electron Microsc. (Tokyo)*, vol. 58, no. 6, pp. 381–392, Dec. 2009.
- [103] L. Claes, K. Eckert-Hübner, and P. Augat, “The effect of mechanical stability on local vascularization and tissue differentiation in callus healing,” *J. Orthop. Res.*, vol. 20, no. 5, pp. 1099–1105, Sep. 2002.
- [104] J.-M. Delaissé, T. L. Andersen, M. T. Engsig, K. Henriksen, T. Troen, and L. Blavier, “Matrix metalloproteinases (MMP) and cathepsin K contribute differently to osteoclastic activities,” *Microsc. Res. Tech.*, vol. 61, no. 6, pp. 504–13, Aug. 2003.
- [105] B. R. Troen, “The regulation of cathepsin K gene expression,” *Ann. N. Y. Acad. Sci.*, vol. 1068, no. 1, pp. 165–172, 2006.
- [106] S. A. Reid, “A study of lamellar organisation in juvenile and adult human bone.”

- Anat. Embryol. (Berl)*., vol. 174, no. 3, pp. 329–38, 1986.
- [107] M. J. Glimcher and H. Muir, “Recent Studies of the Mineral Phase in Bone and Its Possible Linkage to the Organic Matrix by Protein-Bound Phosphate Bonds [and Discussion],” *Philos. Trans. R. Soc. B Biol. Sci.*, vol. 304, no. 1121, pp. 479–508, 1984.
- [108] W. J. Landis, “The strength of a calcified tissue depends in part on the molecular structure and organization of its constituent mineral crystals in their organic matrix.,” *Bone*, vol. 16, no. 5, pp. 533–44, May 1995.
- [109] T. Domon and M. Wakita, “Electron microscope study of osteoclasts with special reference to the three-dimensional structure of the ruffled border.,” *Arch. Histol. Jpn.*, vol. 49, no. 5, pp. 593–602, Dec. 1986.
- [110] S. C. Marks, “Congenital osteopetrotic mutations as probes of the origin, structure, and function of osteoclasts.,” *Clin. Orthop. Relat. Res.*, no. 189, pp. 239–63, Oct. 1984.
- [111] A. Z. Zallone, “Relationships between shape and size of the osteoblasts and the accretion rate of trabecular bone surfaces.,” *Anat. Embryol. (Berl)*., vol. 152, no. 1, pp. 65–72, Dec. 1977.
- [112] W. L. Ries, J. K. Gong, and M. M. Sholley, “A comparative study of osteoblasts: in situ versus isolated specimens.,” *Am. J. Anat.*, vol. 172, no. 1, pp. 57–73, Jan. 1985.
- [113] C. Palumbo, “A three-dimensional ultrastructural study of osteoid-osteocytes in the tibia of chick embryos.,” *Cell Tissue Res.*, vol. 246, no. 1, pp. 125–31, 1986.
- [114] M. Sasaki, H. Hongo, T. Hasegawa, R. Suzuki, L. Zhusheng, P. H. L. de Freitas, T. Yamada, K. Oda, T. Yamamoto, M. Li, Y. Totsuka, and N. Amizuka, “Morphological aspects of the biological function of the osteocytic lacunar canalicular system and of osteocyte-derived factors,” *Oral Sci. Int.*, vol. 9, no. 1, pp. 1–8, 2012.

THESIS DECLARATION

I declare that I have completed this dissertation single-handedly without the unauthorised help of a second party and only with the assistance acknowledged therein. I have appropriately acknowledged and referenced all text passages that are derived literally from or are based on the content of published or unpublished work of others, and all information that relates to verbal communications. I have abided by the principles of good scientific conduct laid down in the charter of the Justus Liebig University of Giessen in carrying out the investigations described in the dissertation.

Francisca I. Alagboso

Giessen, Germany

ACKNOWLEDGEMENTS

My immense gratitude goes to my mentor Prof. Dr. Dr. Volker Alt for permitting me to carry out my PhD work under his guidance. His continual support, guidance and kindness enabled me to complete this thesis successfully.

It gives me great pleasure to acknowledge the invaluable help and support I received from Dr. Ursula Sommer throughout my PhD work. Her unswerving expert ideas and constructive discussions during my experimental work were noteworthy. I also wish to express my profound appreciation for her meticulous revision of my thesis.

My sincere thanks go to PD. Dr. Ulrich Thormann and Dr. Matthaeus Budak for providing their invaluable expertise and support in animal surgeries. Special thanks to Dr. Seemun Ray, Mr. Andreas Kaiser and Mrs. Nirosha Wijekoon for offering the best teamwork during the animal surgeries.

I am truly grateful for the support provided by the technical staffs in the Experimental Trauma Surgery and Radiology laboratories, Giessen University. My special thank you go to Mrs. Ida Oberst, Irina Bogun, Ivonne Bergen and Gunhild Martels for the brilliant technical support.

My sincere appreciation go to the collaborating partners: Dr. Marian Kampschulte from the Radiology laboratory, Giessen University, and to Dr. Anja Henss from the Institute for Physical Chemistry, Giessen University and Prof. Dr. Lutz Dürselen from the Institute of Orthopaedic Research and Biomechanics, Ulm University for the invaluable support and discussions during my experimental work.

I am also grateful to Prof. Dr. Christian Heiß for giving me the great opportunity to participate in the interdisciplinary SFB/79 research group and to the laboratory head Prof. Dr. Katrin Lips for providing the conducive work environment to conduct my research work. Also, I appreciate the general support and the peaceful working atmosphere provided by all the laboratory members.

I owe my gratitude to the German Research Foundation (DFG) for funding this project under the collaborative research work SFB/79 and the international Giessen Graduate Centre for the Life sciences (GGL) for allowing me to benefit from their well-structured graduate school program.

I am forever grateful to my family for their continual loving support and help.

Words are not enough for me to express my heartfelt gratitude to my dear husband for his constant support and encouragement and to my loving son for bringing me so much joy that help eased my stressful moments.

Last but by no means least; I thank the GOD ALMIGHTY who made everything possible.

